University of Debrecen

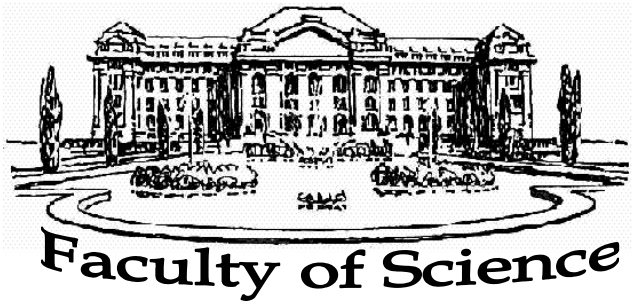

Faculty of Science

ION BEAM BASED NUCLEAR MICROANALYSIS OF GEOLOGICAL AND ARCHEOLOGICAL OBJECTS

PhD thesis

Zoltán Elekes

UNIVERSITY OF DEBRECEN
Debrecen, 2001

PREFACE

The claim to the understanding of our surroundings and predecessors has already been existed at the dawn of our civilization, hence the birth of geology and archeology can be dated to very early times. However, for long times, these sciences were restricted to observations, sometimes questionable theories and interpretations which were not supported by experimental data and precise measurements.

Reliable analytical study of geological objects was started only at the mid of the 19th century by the introduction of the petrologic microscope and wet chemical methods, while the so-called "New Archeology", which wanted to support the archeological methods and theories with an exact scientific frame, began in the 1960's. From this time on, powerful physical techniques like radioactive age determination methods, magnetic and electric resistivity surveying, etc., have also been gradually involved into the analytical investigations to gain as much information, and to give as precise interpretations as possible.

The appearance of ion beam methods in archeology and geology can be dated to about 50 years back, but it became widely used only in the 1970's. The ion beam techniques can give wide variety of information on the studied objects including compositional, lateral and spatial distributions and have nondestructive capabilities, which makes them comprehensively useful in archeological and geological research.

In the Institute of Nuclear Research of the Hungarian Academy of Sciences (ATOMKI), the first application of ion beams in the field of archeology was in 1994 when roman glasses were studied by Proton Induced X-ray Emission (PIXE) and Proton Induced Gamma-ray Emission (PIGE) techniques [Bor94]. Since then, enormous developments (installation of a scanning microprobe

facility and various kind of radiation detectors) were carried out, and nowadays the ion beam analysis is routinely used.

This work includes interdisciplinary ion beam research in ATOMKI. It shows how the ion beam based analytical techniques can help the basic research of geology and archeology and demonstrates how they relate back to physics and prompt methodological developments and measurements of fundamental parameters required for analytical purposes.

In chapter 1 a short summary of the principles of the applied ion beam techniques (PIXE /Particle Induced X-ray emission/ and some NRA /Nuclear Reaction Analysis/ methods) and their realization in practice at the ATOMKI nuclear microprobe is discussed. It also contains the author's contribution to the technical and experimental improvements in a longer form (subchapters 1.3.1 and 1.3.2). Chapter 2 includes specific applications of ion beams in the field of geology and archeology carried out by myself with my cooperators. Detailed description of the problems, the given answers and the conclusions are drawn as well.

I would like to thank the many people at the Section of Electrostatic Accelerators who made it possible to realize this work. My very special thanks are due to my supervisor, Árpád Zoltán Kiss who always helped and supported me. I am also grateful to my archeologist colleagues, Katalin T. Biró and Tamás Gesztelyi and geologist cooperators Gyula Szöőr and Péter Rózsa who raised exciting problems and were always ready for discussion. Finally, I would like to acknowledge the assistance of some members of the ATOMKI researcher staff, namely, Gyula Hegyesi, József Molnár, Attila Krasznahorkay and János Gulyás.

CONTENTS

1. THE ATOMKI NUCLEAR MICROPROBE AND THE APPLIED METHODS

In this chapter the ATOMKI nuclear microprobe and the techniques applied in this work are described with an emphasis on my contribution to methodological developments carried out in the past five years around the microprobe and on my results achieved in the improvements of the experimental techniques.

Subchapter 1.1 begins with a brief introduction to the concept and theory of the nuclear microprobes and continues with the presentation of the realized instrument at our laboratory.

Subchapter 1.2 is a short summary of the PIXE method. Its principles are first detailed, then its practical implementation at the microprobe facility is described[1].

Subchapter 1.3 is about those NRA techniques, namely, ion-ion and ion-gamma reactions, which were used in the analytical investigations. At the beginning the theory and concepts of these methods are discussed, while subchapters 1.3.1 and 1.3.2 deal with the installation and application of a Clover-Ge-BGO detector system and my study on the role of deuterons in ion beam analysis respectively.

[1] In one case (analysis of Roman gems in subchapter 2.1.1) the macro-PIXE setup of ATOMKI was used. Nevertheless, it is not connected strongly to the subject of the thesis, therefore it is discussed in the corresponding subchapter.

1.1 THE ATOMKI NUCLEAR MICROPROBE FACILITY

Principles

The instrument which provides chemical information on a sample with a certain lateral resolution is called a microprobe [Che81]. In order to get this information, the samples should be irradiated with some sort of particles. In the case of nuclear microprobes, these particles are ions, and they are supplied by a particle accelerator.

The schematic layout of a nuclear microprobe is shown in Figure 1.1.1. The ion beam from the accelerator is transferred to an aperture (the so-called object slit). The demagnified image of the aperture generated by the focusing lens is imaged on the surface of the sample over which the ion beam is scanned in order to explore the lateral distribution of the elements. The elemental maps can be produced by storing and plotting the information on the beam position and the emerging radiation in a two-dimensional graph using, e.g., a color scale for the different intensities.

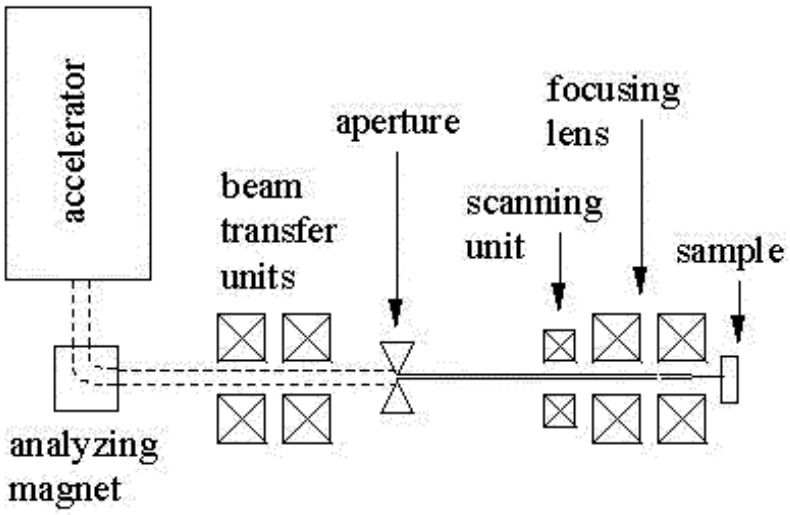

Figure 1.1.1 Schematic layout of a nuclear microprobe

The ATOMKI nuclear microprobe facility

The ATOMKI nuclear microprobe was installed in 1994. The paper [Raj96] deals with the installation and contains detailed description of the facility, therefore only some important features are recalled here in a short way.

For the production of ion beams, the 5 MV single ended Van de Graaff accelerator of ATOMKI is used. The microprobe is located at the 0° beamline, which is shown in Figure 1.1.2.

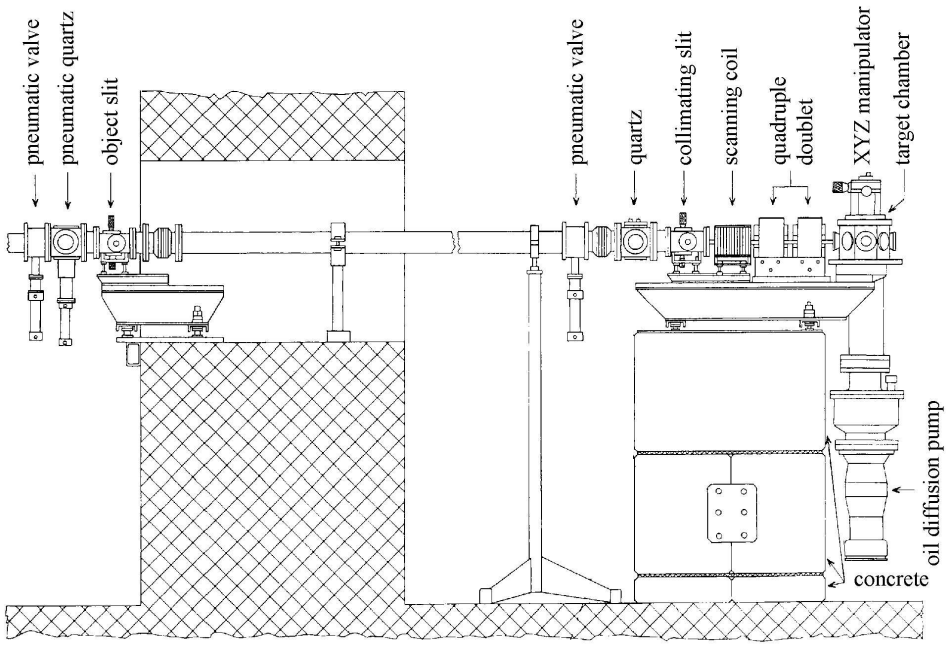

Figure 1.1.2 The ATOMKI nuclear microprobe beamline

After passing the beam shaping and focusing system (object slit, collimating slit, magnetic quadruple doublet), the ions enter the target chamber (the recently modified version of which can be found in [Uzo01]) and hit the sample (Figure 1.1.3). The specimen is adjusted with an XYZ translating manipulator of 5-10 μm precision. The smallest attainable focus is 1 μm x 1 μm, while the largest scan size is 2500 μm x 2500 μm.

The beam current is measured by a small beam chopper placed at the

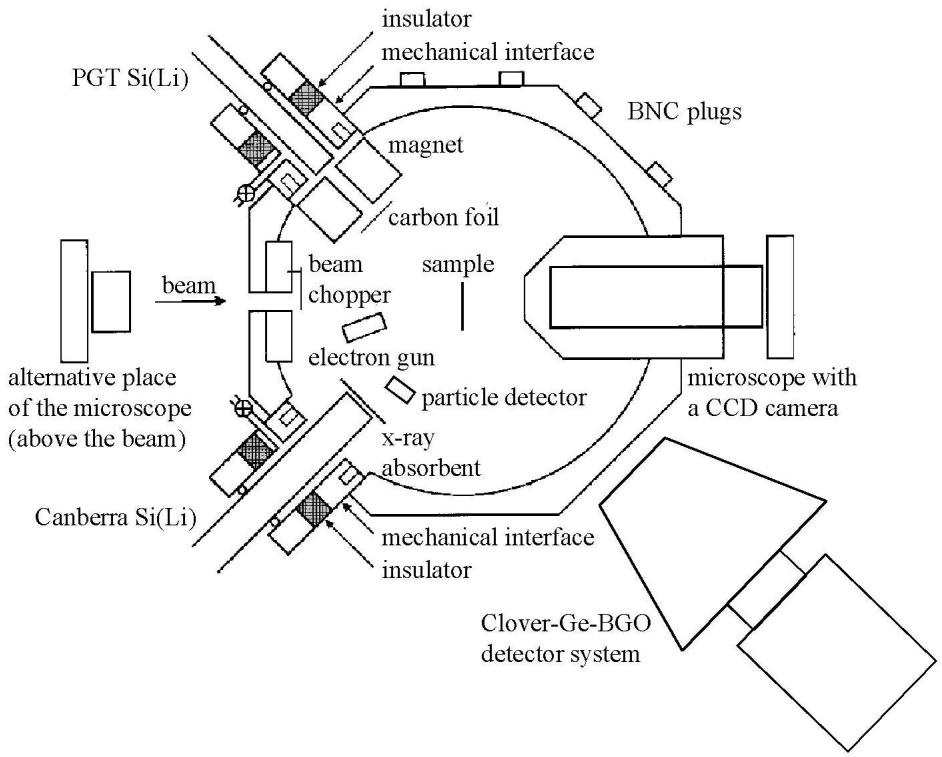

Figure 1.1.3 The ATOMKI nuclear microprobe sample chamber

entrance hole of the chamber. The ions scatter back from the wing of the chopper into an annular surface barrier semiconductor detector at 180° with respect to the beam direction. The calibration of the particle yield is carried out using a micro Faraday-cup with an entrance hole of about 300 μm [Bar00]. The usual beam currents are 30 pA and 1 nA at 1 μm x 1 μm and 10 μm x 10 μm beam sizes respectively.

For the optical observation of the sample, a microscope equipped with a colored CCD camera is situated at 0° with respect to the beam direction. This microscope can also be mounted at 180° when thick samples are analyzed.

In order to prevent the charging up of insulating samples, an electron gun is used during some measurements. The necessity of this device is explained in subchapter 1.2.

For the detection of the radiation induced by the particle beam hitting the sample, the nuclear microprobe is equipped with the following detectors:

The X-rays leaving the sample are detected by two Si(Li) detectors symmetrically placed at 135° with respect to the beam direction. A detailed description of the set-up can be found in subchapter 1.2.

For the detection of charged particles, moveable surface barrier semiconductor detectors are used, which is described in subchapter 1.3.

The gamma-rays are detected by Harshaw Ge(Li) or Canberra HPGe detectors and recently a Clover-Ge-BGO detector system. The details of this topic is discussed in subchapter 1.3.

The analytical methods based on the detection of different kinds of radiation mentioned above and their application in the interdisciplinary analyses are highlighted at the end of their detailed description in Table 1.3.1.

An Oxford type OMDAQ data acquisition system [Gri94] is used for generating the so-called elemental maps and for controlling the scanning unit. The X-ray, gamma-ray and particle spectra are stored by means of Nucleus ADCs independent of each other.

1.2 PARTICLE INDUCED X-RAY EMISSION

Principles

Particle induced X-ray emission is a multi-stage process. The ion approaching the atom with considerably high kinetic energy first creates vacancies in the inner electron shells of the target atom, then these vacancies are filled up by outer shell electrons. The excess energy are taken away by either photons or Auger electrons. The emitted photons are named so that the initial and final state of the atom are taken into account. In Figure 1.2.1 the most common transitions are plotted. The energy of the radiation is characteristic to the atomic number of the target atom.

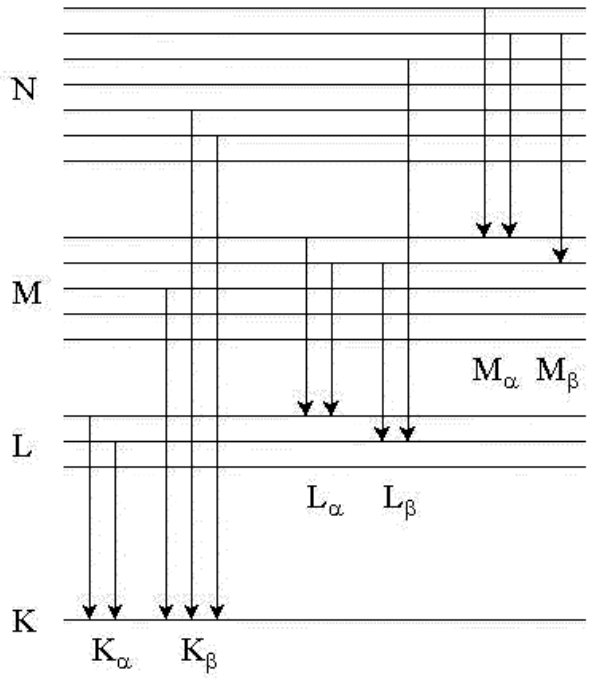

Figure 1.2.1 Some common X-ray transitions

The yield of an X-ray peak is proportional to the concentration of the respective element and can be given by the following formula [Sza89, Joh88]:

$$Y_{lm} = N_b N_{Av} \frac{C_l}{M_l} \frac{\Omega}{4\pi} W_{lm}$$

$$W_{lm} = \varepsilon(E_{lm}) T(E_{lm}) [\int_{E_b}^{0} \frac{\sigma_{lm}(E)}{SM(E)} e^{-\mu(E_{lm}) X(E) \frac{\cos\alpha}{\cos\beta}} dE + \sum_{ij} \frac{C_i}{M_i} \int_{E_b}^{0} \frac{\sigma_{ij}}{SM(E)} SF_{ij}(E) dE]$$

$$X(E) = \int_{E_b}^{E} \frac{dE'}{SM(E')} \text{ where}$$

N_b the number of the bombarding particles with energy E_b

N_{Av} the Avogadro's number

C_l the concentration of the element l in g/g

M_i mass of the atom i in AMU

$\Omega/4\pi$ the solid angle of the detector

$\varepsilon(E_{lm})$ the efficiency of the detector

$T(E_{lm})$ the transmission of the absorbers placed between the sample and the detector

E_b the initial bombarding energy

$\sigma_{lm}(E)$ X-ray production cross section of the line m of the element l

$SM(E)$ the stopping power in the sample at energy E

$\mu(E_{lm})$ the mass absorption coefficient of the sample for X-rays of energy E_{lm}

α the angle between the normal of the sample and the direction of the projectiles

β the angle between the normal of the sample and the direction of the detector

SF_{ij} the outgoing intensity of the radiation lm in the direction of the detection β excited in the total volume of the sample by the radiation ij of unit intensity in depth $X(E)$.

For the detection of X-rays, Si(Li) semiconductor detectors are used with a typical energy resolution of 140 eV at 5.9 keV. Their efficiency is the largest

between 4 and 15 keV. The low energy limit of the detection strongly depends on the material and thickness of the detector entrance window, which is commonly made from beryllium (because its atomic number and, consequently, its absorption for X-rays is small, and quite thin window can be produced from it), partly employed to prevent the detector from the scattered ions which can deteriorate the semiconductor crystal, and partly to maintain vacuum in the end cap. In front of the detectors, some absorption filters are often placed to reduce the intensity of major or disturbing X-rays, thus decreasing the detection limit of other elements.

If we plot the X-ray yield as the function of target atomic number for a usual detector and bombarding energy (Figure 1.2.2), we can observe that the yield is the largest in the range $13<Z<30$ for K_α lines and $60<Z<80$ for L_α lines. (Recently, ultra thin, polymer windowed detectors are also produced where this graph is slightly different.) The position of the sharp drop at the lower Z numbers depends on the detector efficiency, while the gradually decreasing tendency at the higher atomic numbers is the consequence of the fall of the ionization cross section.

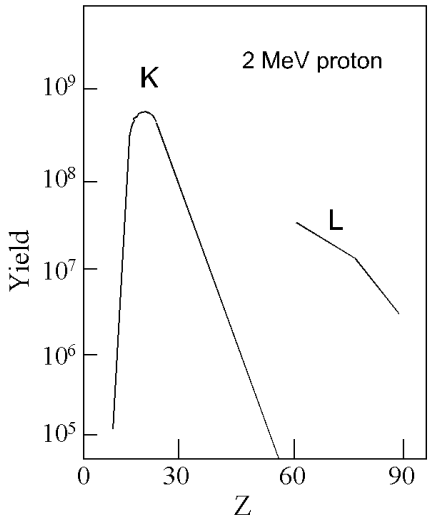

Figure 1.2.2 X-ray yield vs. target atomic number for a usual detector and bombarding energy

The spectrum analysis and concentration calculation are quite complicated in PIXE, therefore computer packages are used for the evaluations in which several effects should be considered:

- energy loss of the projectiles and the attenuation of X-rays in the sample material and detector entrance window
- the X-rays of energy E_x can interact with the Si atoms of the detector, and the emerging radiation may escape from the detector, thus so-called escape peaks appear in the spectra
- if two pulses arrive to the amplifier at nearly the same time, they are seen as one pulse twice the height (these peaks are called pile-up peaks)
- there are various origins of background radiation which has to be taken into account in the fitting procedure: the bremsstrahlung of the secondary electrons ejected from the sample, projectile bremsstrahlung, Compton scattering of gamma-rays occurring in the detector; the charging up effects of the insulating samples, which causes the free electrons to accelerate towards the sample.

The knowledge of background under the peaks is also important from the point of view of detection limits which is a key feature of an analytical technique. The minimum detection limit of element i (MDL_i) is defined by the following expression:

$$MDL_i = 3\frac{\sqrt{BG}}{Y}$$

where Y is the given peak area and BG is the sum of the background counts under this peak. In routine measurements, the relative detection limits are in the range of 10^{-6}-10^{-7} g/g, while the absolute detection limits vary between 10^{-9}-10^{-12} g depending on the sample matrix, thickness and beam size. The total uncertainty of the concentration values ranges from 5 to 10 %. Extremely low detection limits can be achieved by means of microbeams. With few micrometer lateral resolution, the absolute detection limits are 10^{-15}-10^{-16} g.

PIXE measurements at the ATOMKI nuclear microprobe

Several details of the target chamber and experimental conditions used at the nuclear microprobe have been discussed earlier in subchapter 1.1, therefore only the specific parts, which relates to the PIXE analysis, is touched now.

Although the beam parameters and experimental conditions vary from measurements to measurements, which is separately detailed in each subchapter dealing with the applications, a general description can be given for micro-PIXE analyses. The usual beam energy is 2 MeV because the X-ray production cross-section is high enough at this energy, however most of the nuclear reactions are not significant, therefore they do not cause high energy background in the X-ray spectra. For the detection of the radiation emitted by light atoms (up to Fe), the beam current is kept low (30-100 pA at 1-9 μm^2 beam spot sizes) in order to avoid pile-up effect. Nevertheless, sometimes when detecting energetic X-rays (>5 keV) from heavier atoms, higher intensity (1-2 nA at 100 μm^2 beam size) is used with absorption filters in front of the detector to collect enough counts in the X-ray peaks in reasonably short times. For the quantitative determination of concentration values of major and minor elements, collected charges of 0.01-0.1 μC are sufficient, however to achieve this goal for trace elements, a few μC should be used.

The photons emitted from the target are detected by two Si(Li) detectors. The high energy part of the radiation (larger than 5 keV) is monitored by a common Be-windowed detector with 24 μm Hostaphan and 98.8 μm aluminum filters in front of its entrance window[2], while the other detector with an ultra thin (0.38 μm) polymer window is dedicated to light elements. Even the extremely low energy X-rays from carbon (0.28 keV) can be detected with this set-up. Some MDLs characterizing the best results can be found in [Uzo01]. However, both the scattered ions and the light can penetrate the thin entrance window. Therefore, a permanent magnet is used in front of the detector to deflect

[2] Before the purchase of the ultra thin window detector, it was also used without aluminum filter to determine the concentration of the lighter elements down to Al

the ions which can deteriorate the detector, and a thin carbon foil (40 $\mu g/cm^2$) is mounted as an absorber to get rid of the filtering light. (If it is required, other absorbers can also be mounted externally with a filter rotating device.)

As it was mentioned in subchapter 1.1 the charging up effect of the samples should be removed. In order to do this, an electron gun is mounted close to the target. In fact, this electron gun is a filament the power supply of which can be adjusted (in this way its electron current is changed) corresponding to the given sample. The possibility of the beam current measurement still remains with the usage of the beam chopper.

The spectrum evaluation and the concentration calculations are carried out by using an updated version of the program package PIXYKLM [Sza93] which is capable of handling even micro-PIXE spectra taken on rounded objects.

1.3 NUCLEAR REACTION ANALYSIS

Concepts and theory

When a sample is bombarded by ions of a few MeV energy, several interactions may occur among which the major ones are nuclear reactions. These reactions are governed by the following general equations which are deduced from the conservation of energy and momentum principles (Figure 1.3.1) [Bir85]:

$$\mu = \frac{M_2}{M_1}$$

$$E_T = E_1 + Q = E_3 + E_4$$

$$W = \frac{(M_1 M_3 E_T + M_1 M_3 Q)}{M_1 M_4 E_1}$$

$$X = \frac{M_1 M_3 E_1}{E_T (M_1 + M_2)(M_3 + M_4)}$$

$$Y = \frac{M_2 M_4 (1 + \frac{M_1 Q}{M_2 E_T})}{(M_1 + M_2)(M_3 + M_4)}$$

$$K = (\frac{\cos\theta \pm \sqrt{\mu^2 - \sin^2\theta}}{1+\mu})^2$$

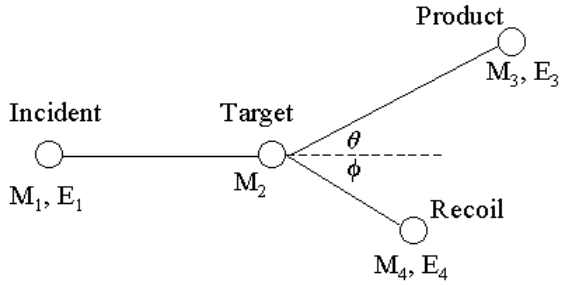

Figure 1.3.1 Relevant particle parameters in nuclear reactions

a) for normal kinematics (*M2>M1*, $Y \geq X$, using positive sign unless *Y>X*)

PRODUCT ION $$E_3 = XE_T(\cos\theta \pm \frac{Y}{\sqrt{X - \sin^2\theta}})^2$$

RECOIL ATOM $$E_4 = E_1 + Q - E_3$$

b) for threshold reactions (*Q*<0)

PRODUCT ION $$E_3 = XE_T(\cos\theta \pm \frac{Y}{\sqrt{X - \sin^2\theta}})^2$$

RECOIL ATOM $$E_4 = E_1 + Q - E_3$$

THRESHOLD ENERGY $$E_t = -Q\frac{(M_1 + M_2)}{M_2}$$

where *Q* is the energy release in the reaction in question. Most useful reactions have large *Q* values, and if the final nucleus is formed in an excited state of energy *E'*, then a modified energy balance (*Q'=Q=E'*) must be used in kinematics calculations.

From the energy of the emitted particles, principally, the target nucleus can be identified, however it is not an easy task because the primary radiation can be changed in several ways when passing through the target material and interacting with the detector nuclei and atoms.

The yield of the nuclear reaction products depends on the reaction cross-section. Each reaction has its own characteristic dependence on energy and angle of observation. The yield of the product radiation is proportional to the concentration of the emitting isotope. Although the nature of the significant interactions, which should be taken into account in calculations, is different for each analytical technique based on the various reactions, the following treatment provides equations which are common to most aspects of ion beam analysis:

For so-called thick samples (thickness greater than the range of the incident ion), and supposed that the product radiation is not significantly attenuated by travelling through this still quite thin layer,

the observed yield obeys the following relation:

$$Y_3 = N_1 e d\Omega f_i \int_0^R \frac{d\sigma}{d\Omega} dx = N_1 e d\Omega f_i \int_{E_1}^0 \frac{d\sigma}{d\Omega \varepsilon_m(E)} dE = N_1 e d\Omega \frac{c_i}{m_i} \int_{E_1}^0 \frac{d\sigma}{d\Omega S_m(E)} dE$$

N_1 the number of the incident ions

e the detector efficiency

$d\Omega$ the solid angle of the detector

f_i atomic percent of the isotope i in the sample

$\frac{d\sigma}{d\Omega}$ the differential cross-section in barn/(atom·sr)

dx the ion path length in the sample in atom/cm^2

E_1 the initial bombarding energy

$\varepsilon_m(E)$ the stopping cross-section ($\varepsilon_m(E) = \sum_i f_i \varepsilon_i(E)$ for a mixture)

c_i weight percent of the isotope i in the sample

m_i equals $\frac{M_i}{N_{Av}}$ where M_i is the mass number of the isotope i and N_{Av} is the Avogadro's number

$S_m(E)$ the stopping power ($S_m(E) = \sum_i f_i S_i(E)$ for a mixture).

Since accurate data on the cross-section are practically not available, approximations are commonly used in concentration calculations. The most powerful and widespread one is the average stopping power method [Ish87, Dec78]. If an average stopping power is defined as the stopping power at an energy $\overline{E}$ such that

$$\overline{E} = \frac{\int E \frac{d\sigma}{d\Omega} dE}{\int \frac{d\sigma}{d\Omega} dE},$$

then the ratio of concentrations from a standard (with known composition)

and an unknown sample is:

$$f_i = f_s \frac{Y_i}{Y_s} \frac{\varepsilon(\overline{E})}{\varepsilon_s(\overline{E})} \qquad \text{and} \qquad c_i = c_s \frac{Y_i}{Y_s} \frac{S(\overline{E})}{S_s(\overline{E})}.$$

This approach gives deviations from the true yield by 10 % or less in most cases.

If the outgoing radiation is significantly attenuated in the sample or in the absorbers placed in front of the detector, the calculated yields should be multiplied by additional attenuation factors.

Ion-ion reactions

Both the ion inducing the reaction and the ion emitted by the excited nucleus are influenced by the Coulomb barrier of the target nuclide, therefore at energies of a few MeV, ion-ion reactions are most probable for light ion irradiation of light nuclides. For thick targets, the energy and yield of the outgoing ions are modified by the sample matrix, hence the resulting particle spectrum is complicated and difficult to interpret sometimes even when resonances are used. Moreover, the detection limits for the different elements are strongly depend on the given reaction, thus the ion detection method cannot be regarded as a multielemental technique.

For the detection of the product ions, surface barrier semiconductor detectors with energy resolution of about 10 keV are customarily used. (However, a number of electrostatic and magnetic spectrometers are recently employed in ion beam analysis with an order of magnitude better resolution [Lan00, Dol98].) Sometimes various types of absorber foils are mounted in front of the entrance window either to prevent the detector from light or to avoid high count rate (which is originated from backscattered ions) or to eliminate disturbing and uninteresting radiation. However, the major drawback of foil technique is that the resolution may be degraded to about 50 to 100 keV.

Sensitivities of the order of 10 μg/g or even less can be achieved with measuring times of tens of minutes and commonly using 0.5 to 2 MeV energies.

Ion-gamma reactions

Particle Induced Gamma-ray Emission (PIGE) is one of the most common applications of NRA.

The emitted radiation are almost not attenuated, therefore it is not necessary to put the detectors into a vacuum chamber. On the other hand, the detectors with a possible shielding sometimes are too large to fit into these chambers. However, the efficiencies are very low, therefore they should be placed as close to the sample as possible. Because of this low efficiency, quite high beam currents and collected charge is employed. The best known and everyday-used detectors are:

- Lithium Drifted Germanium /Ge(Li)/ and Hyperpure Germanium /HPGe/ with low efficiency and good energy resolution
- Sodium Iodide /NaI/ and Bismuth Germanate /BGO/ with high efficiency and low energy resolution.

Nowadays the HPGe and Ge(Li) detectors mostly serve as analytical devices, while the latter ones are often built into detector systems as veto instruments by means of which, the detection limits can be significantly reduced.

The analysis of a PIGE spectrum is often sophisticated, especially for samples having complex composition, however far easier than the evaluation of a particle spectrum:

- the nuclear reactions can interfere, producing the same final nucleus
- the individual peaks of interest can be overlapped by other peaks (e.g., from the laboratory background)
- quite high background is present from the Compton scattering of photons
- escape peaks of a primary peak with an energy E appear at energies E-511 keV and E-1022 keV because the positron of the electron-positron pair produced during the interaction between the photons and the detector material annihilates, and one or both of 511 keV photons may escape from the detector

- the fitting procedure is complicated by the fact that the photons may undergo Doppler effect, which shifts and broadens the peak.

Generally, PIGE method does not reach the sensitivity level of PIXE technique even for the light elements with the highest cross-sections. Nevertheless, with the careful selection of the bombarding energy and particle, angle of observation, distance between the target and the sample and with the use of coincidence methods and shielding/vetoing devices, 1 to 1000 μg/g detection limits can be achieved for the region A<40. Moreover, several elements can be determined in a single run with considerably good detection limits.

Table 1.3.1
Highlights of the applied methods at low energy accelerators (<5 MV)

	PIXE	Ion-Ion	PIGE
Bombarding particles	p	p, d, α	p, d
Bombarding energy	2-3 MeV	0-5 MeV	0-5 MeV
Detected radiation	X-ray	ion	gamma-ray
Detected elements	C-U multielemental	Li-Ca especially Z<15	Li-Ca especially Z<15
Sensitivity	<10 μg/g	1-500 μg/g	1-1000 μg/g
Concentration uncertainty	10 %	10-20 %	10-20 %
Absolute concentration determination	yes	yes	yes
Isotopic specificity	no	yes	yes
Depth profiling	yes	yes	yes
Depth resolution	1-10 nm	10-100 nm	1-10 nm
Non-destructivity	yes	yes	yes

1.3.1 CLOVER-GE-BGO DETECTOR SYSTEM

Motivation

In the analytical applications, two of the most important requirements are the short measuring time and low detection limit. As it was mentioned before, the cross sections in PIXE technique are higher than that of PIGE method, moreover, lower detection limits can be generally achieved by the detection of X-rays. Therefore, the detection of gamma-rays should be made more efficient, and the background in PIGE spectra should be reduced. These goals can be achieved at the same time by the use of a Clover-Ge-BGO Compton suppression spectrometer which is described below.

General description

The detector system contains a Clover detector and a surrounding BGO shield (Figure 1.3.2).

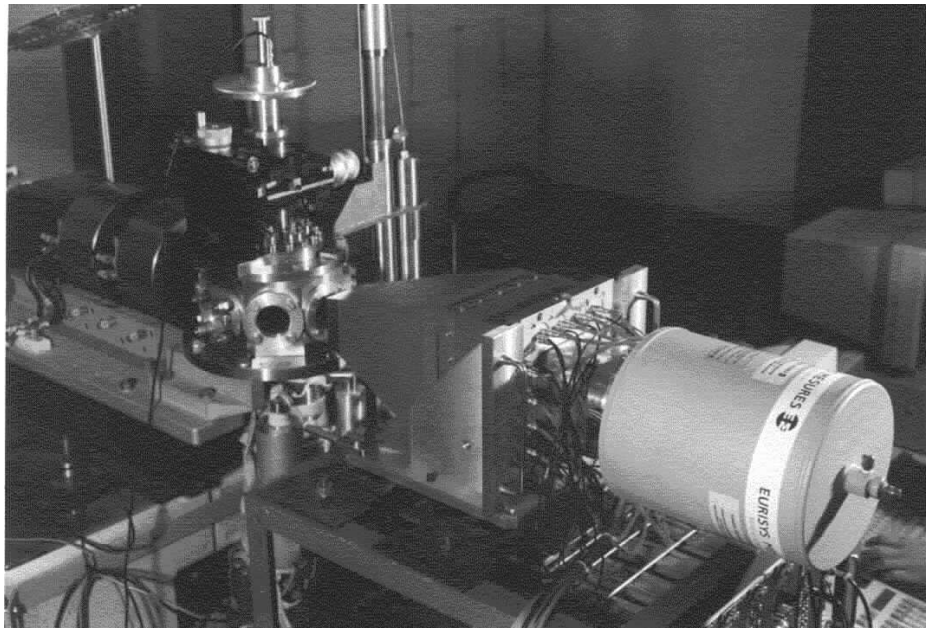

Figure 1.3.2 Photo of the Clover-Ge-BGO detector system at the ATOMKI nuclear microprobe

The Clover has been developed by EURISYS MESURES in the framework of the EUROGAM collaboration. It consists of four coaxial N-type HPGe detectors arranged like a four leaf clover. Each crystal has a square front face with round edges. The sum of their active volumes is about 470 cm^3, and they are mounted in the same cryostat. A common high voltage of +3500 V is applied to the inner contacts. Energy and timing signals are obtained for each crystal through AC coupling.

The BGO detector has been designed by CYBERSTAR having complete compatibility with the Clover detector. It has a pyramidal shape at the end of which, it is cut, and a heavy metal collimator is placed. The detector contains 16 crystals with separate energy outputs and high voltage of +1000 V inputs.

Installation at the nuclear microprobe

The schematic view of the electronic setup built from NIM modules is shown in Figure 1.3.3.

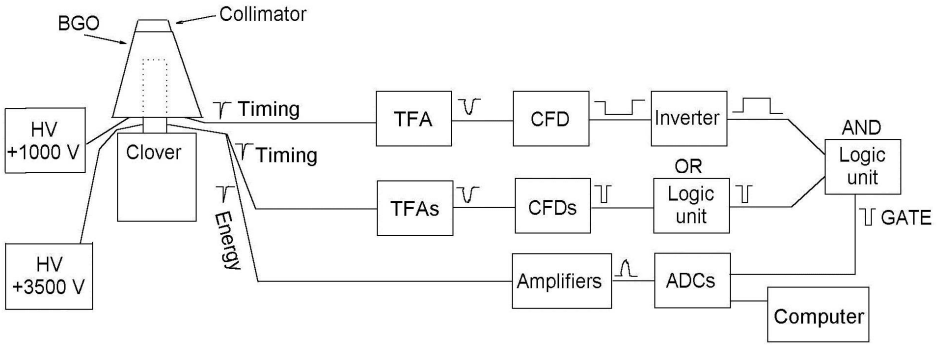

Figure 1.3.3 Schematic view of the electronic setup of the Clover-Ge-BGO system

The four energy signals from the preamplifiers of the Clover detector are fed into linear spectroscopy amplifiers which magnify and shape the pulses in order to facilitate accurate amplitude measurements and to optimize the energy resolutions. Then the maximum amplitudes are converted into digital numbers using analog-to-digital converters (ADCs) used in coincidence mode by applying

appropriate gate pulses (GATE). The outputs are stored in binary format on a personal computer.

The timing signals from the Clover preamplifiers serve as input pulses for four timing filter amplifiers (TFAs) which shape the pulses, allowing the optimization of the signal-to-noise ratios. The outputs are delivered to constant fraction discriminators (CFDs), thus resulting in timing signals independent of the pulse amplitudes. Then an OR function is applied to these output signals by using a four fold logic unit, obtaining a signal which is present when at least one of the detectors catch a gamma-photon (CLOV-OR).

The signals deriving from the independent BGO crystals are summed and accepted by a TFA and then a CFD, gaining a fast timing signal which is delivered to a logic unit where it is inverted. Another logic unit performs an AND function with this signal and the CLOV-OR one. In this way, we get the GATE signals for the ADCs, where the GATE permits the conversion only when at least one of the HPGe detectors send a signal, but the BGO does not fire.

The histograms from the binary file including information on the conversion values of the four ADCs are produced off-line by Physics Analysis Workstation (PAW, from CERN, Geneva) computer package.

The detector system can be used in a slightly modified arrangement as well, i.e., the Clover energy signals can be analogously summed after the preamplification and fed into a PC acquisition card which is gated by the proper pulse created in the way above. This layout results in poorer energy resolution (about 4 keV at 1332 keV), nevertheless it has the advantage of the production of elemental maps and on-line manipulation.

After the buildup of electronics, characteristic features of the detector system (photopeak efficiency, Compton suppression factor, minimum detection limits) were determined.

The total photopeak efficiency (i.e., the sum of the full gamma-ray absorption in each of the individual crystals and the full gamma-ray absorption in two or more crystals for composite detectors) of Clover detectors was measured

earlier [Duc99]. However, this is not reported for the whole detector system containing the BGO shield, therefore it was determined in this work using ^{66}Ga, ^{56}Co, ^{252}Eu and ^{60}Co radioactive sources in a region of 120-4800 keV which is interesting in analytical applications performed by PIGE method. The gamma-emitters were placed at a distance of 25 cm from the Ge crystal front face, and the counting rate did not exceed a few kHz in the total detection mode. The obtained absolute total photopeak efficiency ($\varepsilon_p\omega$) versus the gamma-ray energy is shown in Figure 1.3.4. In this low energy region, the data can be fitted by a quite simple three-parameter equation (fitting coefficient R^2=0.9955):

$$\varepsilon_p\omega = y_0 + \frac{ab}{b+E}.$$

The measured efficiency corresponds to the efficiency obtained in [Duc99] if we consider that the BGO collimator covers approximately the half of the sensitive volume.

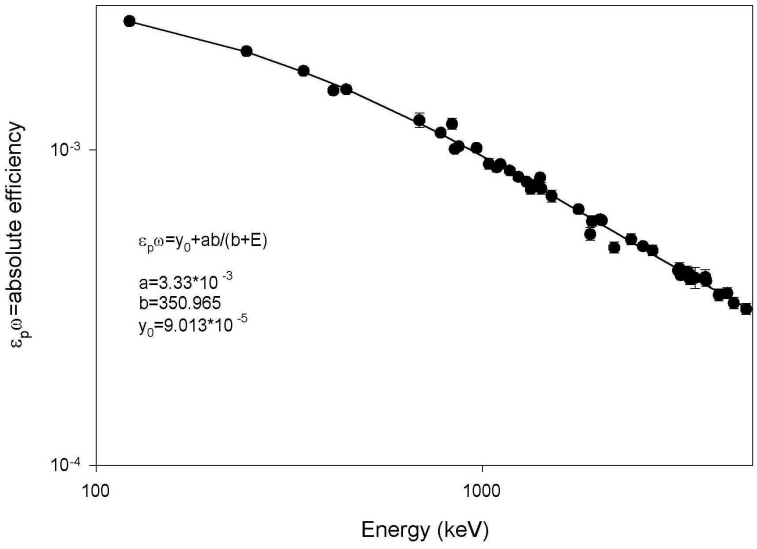

Figure 1.3.4 Absolute total photopeak efficiency of the Clover-Ge-BGO system vs. gamma-ray energy

The most characteristic parameters of the detector system are the peak-to-total (P/T) and peak-to-Compton (P/C) ratios. The P/T value was calculated as the ratio of the summed net area of the 1173 keV and 1332 keV gamma-ray peaks and the total counts in the spectrum above 100 keV. The P/C value is the ratio of the height of the 1332 keV gamma-ray line and the average height of the spectrum between 1040 and 1096 keV. These values were determined in four cases: (A) bare CLOVER detector without shielding, (B) in passive 5 cm thick Pb shield, (C) with the surrounding BGO used as a passive shield, (D) with the BGO anti-Compton shield. The corresponding spectra are plotted together in Figure 1.3.5. The Compton suppression factor (E) as a function of gamma-ray energy, utilizing A and D layout, is added as well. In the attached table, the P/T and P/C data are summarized. Comparing the P/T ratios with the ones in [Duc99], it can be seen that the absolute values are different because in the cited paper the authors subtracted the laboratory background from the spectra. However, the relative peak-to-total ratios are in a good agreement.

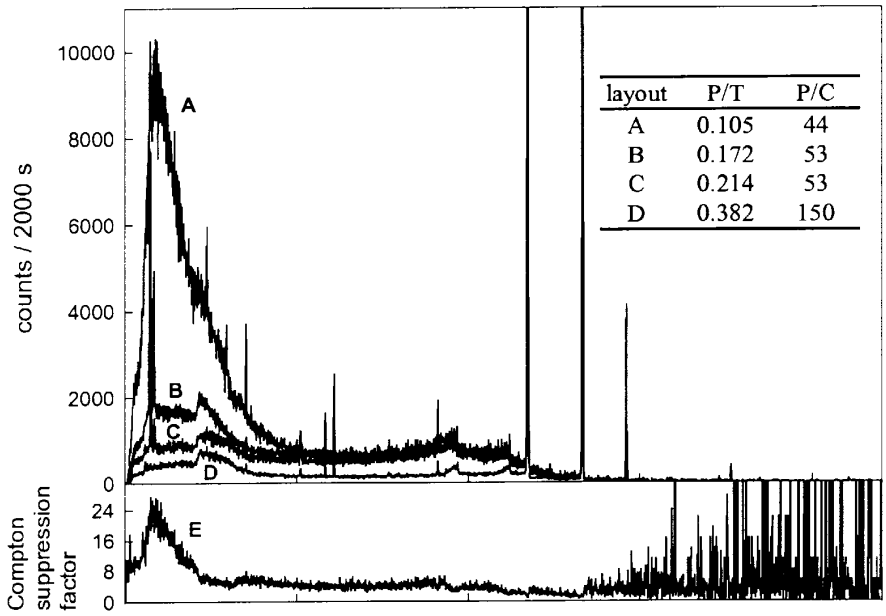

Figure 1.3.5 Spectra taken by the Clover-Ge-BGO system in four different experimental layouts (see text)

In order to check the minimum detection limits achievable with the detector system in micro-PIGE measurements, spectra were taken on several standard mineral and glass samples. Table 1.3.2 includes the MDLs at bombarding energy of 3.3 MeV, beam spot size of 10-100 μm^2, beam current of 1 nA and collected charge of 3 μC (in parentheses the gamma-ray energy values are shown in keV units) which are convenient and common beam parameters and measurement conditions in analytical applications allowing quite fast (30-45 min/sample) concentration determination.

Table 1.3.2
Minimum detection limits in μg/g units

Sample	Li (478)	Be (3562)	B (2125)	F (197)	Na (440)	Al (1014)	Si (1779)
Macusanite volcanic glass	20	-	160	25	75	210	375
Volcanic glass (Tokaj Mts.)	15	-	-	30	110	375	590
Pyrex	-	-	140	-	100	235	490
Fe-tourmaline	-	-	150	-	110	325	430
Petalite	40	-	-	-	-	350	525
Hambergyte	-	420	145	-	-	-	-
Beryl	20	380	-	-	80	240	400

Although the MDLs may strongly depend on the beam energy, measuring time, collected charge, beam spot size, beam current density and sample composition, they can be compared with the values determined by others in different experimental conditions [Tro99, Rio95, Tou93, Cou91]. It can be concluded that the detection limits of the Clover-Ge-BGO system for Li, B and Na are much lower than the values achieved by other setups (e.g., reach the level of a particle detection system in case of Li), while for Be, F, Al and Si the MDLs are similar to each other.

The detection limits for C and O in iron matrix were also determined at 90 and 70 μg/g respectively, using deuteron bombarding particles (incident energy of 1.8 MeV, beam spot size of 100 μm^2, beam current of 1 nA and collected charge of 3 μC), which is discussed in subchapter 1.3.2 in details.

By using common HPGe detectors, the achievable minimum detection limits for C and O are high as compared with the values of charged particle detection, therefore the ion-ion technique is usually preferred for the determination of these elements. However, the values attained by the Clover-Ge-BGO spectrometer show that its MDLs are close to that of the particle detection (10 μg/g each [Tou91, Rya93]) and reasonably good in geological and archeological applications.

1.3.2 APPLICATION OF DEUTERON BEAMS IN ELEMENTAL ANALYSIS

Introduction

In recent years, there has been a growing interest of such ion beam analyses in which charged particle induced reactions leading to the emission of gamma-rays are applied. This is partly due to the use of heavy ion reactions via gamma-ray detection [Sep98] and partly to the appearance of large gamma-ray detectors [Pie96] and detector systems of high efficiency [Ele99] in ion beam applications. The nondestructivity of the methods and the easy use of external beams, when gamma-ray detection is desired, are also important advantages.

Systematic studies of p, α, ^{7}Li, ^{12}C, ^{14}N and ^{16}O induced gamma-ray emission have been performed in several works (see ref. [Sep98, Sav99, Kis85] and references therein), while the systematic investigation of deuteron induced gamma-ray emission (DIGE, or d-PIGE) is concerned by only a former publication [Kis94].

Deuteron induced gamma-ray yields are needed not only for analytical purposes, but also for the effective design and operation of low background experiments in many other fields where energetic deuteron beams are used.

The aim of this work was to continue the analysis of the experimental work done at the AGLAE facility of the Louvre Museum. It was intended to complete the results (published in ref. [Kis94]) with the presentation of typical gamma-ray spectra for the analyzed elements and to construct tables summarizing the most suitable gamma-ray lines for elemental analysis of a given element. The thick-target yields for the most characteristic gamma-rays of elements with Z=3-20 (except Be, Ne, P and Ar) in the deuteron energy range of 0.7-3.4 MeV are also completed with additional yield curves. The thick target yield investigations are contributed to differential cross-section measurements on carbon target material (which was not discussed from the point of view of elemental analysis earlier) in order to gain a better insight to the analytical applicability of DIGE method for concentration determination of carbon. Several

interdisciplinary studies were performed by the deuteron beam of the 5 MV Van de Graaff accelerator of ATOMKI, the experience of which permits to point out some features of the method which make DIGE complementary to other accelerator-based analytical methods.

Experimental and data analysis

Although the measurements were performed earlier by the deuteron beam of the 6 SDH-2 2 MV Pelletron accelerator of AGLAE, some basic experimental conditions are recalled here for the completeness. Typical ion currents were in the range of 0.5-10 nA with average measuring times of about 300 s. The collected charge measured by a calibrated current integrator varied between 0.02 and 20 μC depending on the sample and on the deuteron energy. A precision of about 5 % in the determination of the ion dose could be achieved with this set-up. Instead of elemental targets, compound samples were used in many cases as stable specimens.

For the detection of gamma-rays an Intertechnique N-type HPGe detector (58 mm diameter, 160 cm^3 volume) has been applied at an angle of 135^o with respect to the incident beam direction with a distance of 10 cm between the front face of the crystal and the samples. The high efficiency of the detection system made it possible to use low ion doses, thus avoiding radiation damage of the samples. For further details of the experiment, see ref. [Kis94].

The 8k-channel gamma-ray spectra were sent to a SUN workstation and originally analyzed off-line using the program package FLORENCE available at AGLAE laboratory. The more detailed investigation of the results [Ele97] revealed that this package can not correctly handle neither the peaks not totally resolved nor single peaks showing Doppler broadening. Therefore, a reanalyzes of the experimental data was made with the use of the program package FORGAMMA [Szé85] capable of analyzing complex unresolved gamma-ray peaks and also line shapes with Doppler broadening.

For the conversion of yields taken on compound samples to those of the respective elements, the approximation method of Kenny et al. [Ken80] was followed.

The thin target measurements and interdisciplinary studies were carried out at the nuclear microprobe facility of ATOMKI installed at the 5 MV Van de Graaff accelerator. The cross section experiments on the reaction $^{12}C(d,p\gamma)^{13}C$ were done first by using a self-supporting carbon foil as a target material. The thickness of the foil was determined by Rutherford Backscattering Spectrometry (RBS) using the formula $t = \frac{N}{n \cdot N_{Av} \cdot \Omega \cdot \sigma}$ where t is the thickness, N is the number of scattered particles, n is the number of bombarding ions hitting the target, N_{Av} is the Avogadro's number, Ω is the detector solid angle and σ is the Rutherford cross-section at the given bombarding energy and angle of detection. The measurements were repeated ten times at different spots on the foil with proton beam energy of 2 MeV and collected charge of 0.5 μC. The solid angle of the detector was 30 msr, while the angle between the direction of the beam and that of the detection was 120°. The average value of thickness was determined at 21.4±0.6 μg/cm^2.

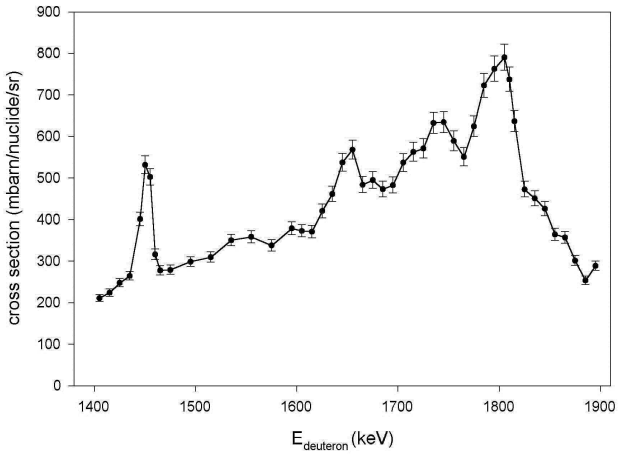

Figure 1.3.6 Excitation curve of the reaction $^{12}C(d,p\gamma)^{13}C$

The measurements of the excitation curve (Figure 1.3.6) was started at deuteron beam energy of 1.9 MeV and continued downwards with energy steps of 10 keV except when the resonance at 1.45 MeV was reached. At this point, the energy step was reduced to 2 keV. The gamma-rays were detected by the Clover-Ge-BGO detector system placed at 55° with respect to the beam direction using detector–target distance of 25 cm. The calculation of the cross-section was based on the relation $\sigma = \frac{N \cdot m}{n \cdot \varepsilon_p \cdot \omega \cdot N_{Av} \cdot t}$ where σ is the differential cross-section, N is the counts in 3089 keV peak originating from the transition between the first excited state and the ground state of ^{13}C produced in the reaction $^{12}C(d,p\gamma)^{13}C$, m is the mass number of the bombarded nucleus, n is the number of deuterons hitting the target, $(\varepsilon_p\omega)$ is the absolute total photopeak efficiency of the spectrometer at 3089 keV with a detector-target distance of 25 cm, N_{Av} is the Avogadro's number and t is the thickness of the foil. The collected charge on the target was 3 μC, while the beam spot size, scanned area and beam current were 100 μm^2, 1 mm^2 and 1 nA respectively.

The number of incident deuterons was measured by the beam chopper. In order to avoid the radiation which would come from the different target chamber material, a Faraday-cup-like box wrapped with tantalum inside was placed behind the target to catch the deuterons passing the foil. It turned out that no disturbing or competing reactions occurred. After every five steps, a test measurement was done irradiating the cup directly without the carbon foil to monitor the contribution of the carbon buildup in the box to the 3089 keV peak. This contribution was measured at 5 % of the total counts and did not change significantly during the measurements. The neutron background deriving from (d,n) reactions was also measured at the object slit of the microprobe where the highest dose was expected.

In the ion beam analysis, the accuracy and minimum detection limits of the method were tested for two of the best detectable elements, namely, oxygen and carbon, measuring on magnetic spherules and some samples (H14 Hungarian

steel, Mylar, Kapton) used as standards with well-known carbon contents, in the same geometry as above. The deuteron beam energy was 1.8 MeV, while the other experimental conditions were the same as for excitation function measurements.

Results and discussion

In Figures 1.3.7-1.3.10 only some gamma-ray spectra corresponding to Li, C, N, O (bombarded by deuteron beam of 1.8 MeV) and yield curves of the strongest gamma-rays are plotted together. However, the graphs for the other elements can be found in [Ele00]. Tables listing the gamma-ray energies originating from the samples and the nuclear reaction from which the respective gamma-rays emerged are added to the figures. The energy values of peaks for which yield curves are shown and proposed to be selected for elemental analysis are typed in bold, thus contrasting with other peaks originating from the element in question. In the case of the gamma-ray spectrum obtained using a $LiSO_4$ sample, several other peaks are also marked (their energies are underlined). As for their origin, they emerge because the neutrons produced in (d,n) reactions generate (n,n'γ) reactions on nuclei of the Ge crystal and target chamber materials (Al, Fe, Cu). On the other hand, they may come from deuteron induced reactions on elements like C, O, and Si which contaminate mostly the samples but also some parts of the sample chamber or diaphragms of the beam transport line. As it is expected in common gamma-ray spectrometry, the annihilation peak at 511 keV and the escape peaks (marked by a link to the full energy peaks in the figures) of the high energy peaks also appear. These disturbing peaks are listed in Table 1.3.3. (But they are denoted only in the above spectrum to avoid complicate presentation). The peaks which originate from other sample constituents, when a compound was applied for the analysis, are not indicated in the spectra.

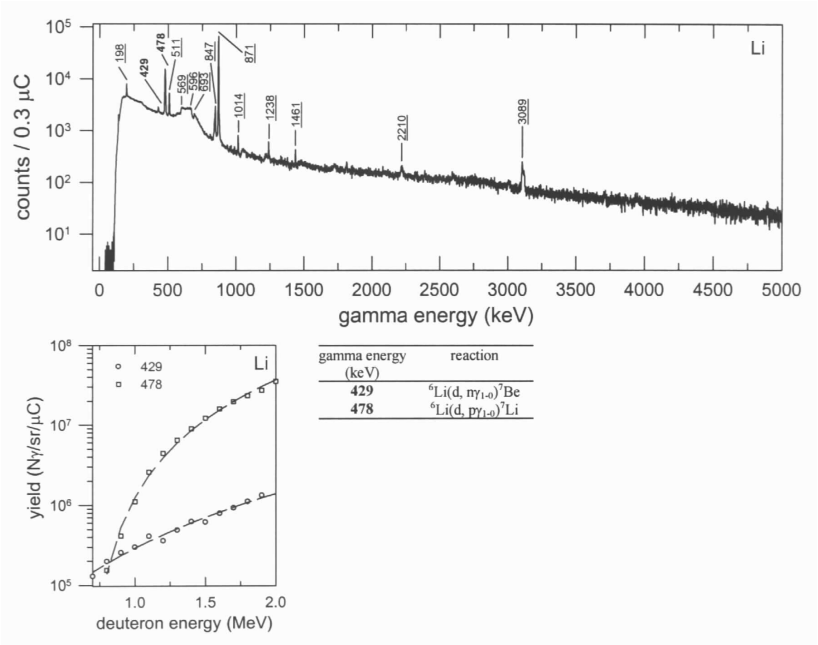

gamma energy (keV)	reaction
429	^{6}Li(d, n$\gamma_{(1-0)}$)^{7}Be
478	^{6}Li(d, p$\gamma_{(1-0)}$)^{7}Li

Figure 1.3.7 Spectrum, yield curves and tables with peaks for lithium. The spectrum was measured at E_d=1.8 MeV on $LiSO_4$

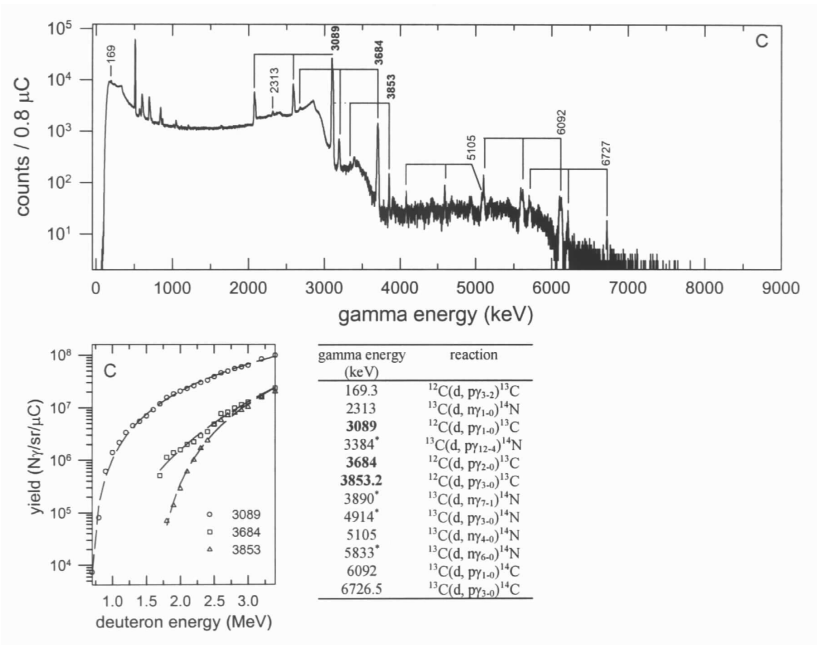

gamma energy (keV)	reaction
169.3	^{12}C(d, pγ_{3-2})^{13}C
2313	^{13}C(d, n$\gamma_{(1-0)}$)^{14}N
3089	^{12}C(d, p$\gamma_{(1-0)}$)^{13}C
3384*	^{13}C(d, p$\gamma_{(12-4)}$)^{14}N
3684	^{12}C(d, p$\gamma_{(2-0)}$)^{13}C
3853.2	^{12}C(d, p$\gamma_{(3-0)}$)^{13}C
3890*	^{13}C(d, n$\gamma_{(7-1)}$)^{14}N
4914*	^{13}C(d, p$\gamma_{(3-0)}$)^{14}N
5105	^{13}C(d, n$\gamma_{(4-0)}$)^{14}N
5833*	^{13}C(d, n$\gamma_{(6-0)}$)^{14}N
6092	^{13}C(d, p$\gamma_{(1-0)}$)^{14}C
6726.5	^{13}C(d, p$\gamma_{(3-0)}$)^{14}C

Figure 1.3.8 Spectrum, yield curves and tables with peaks for carbon. The spectrum was measured at E_d=1.8 MeV on pure C.

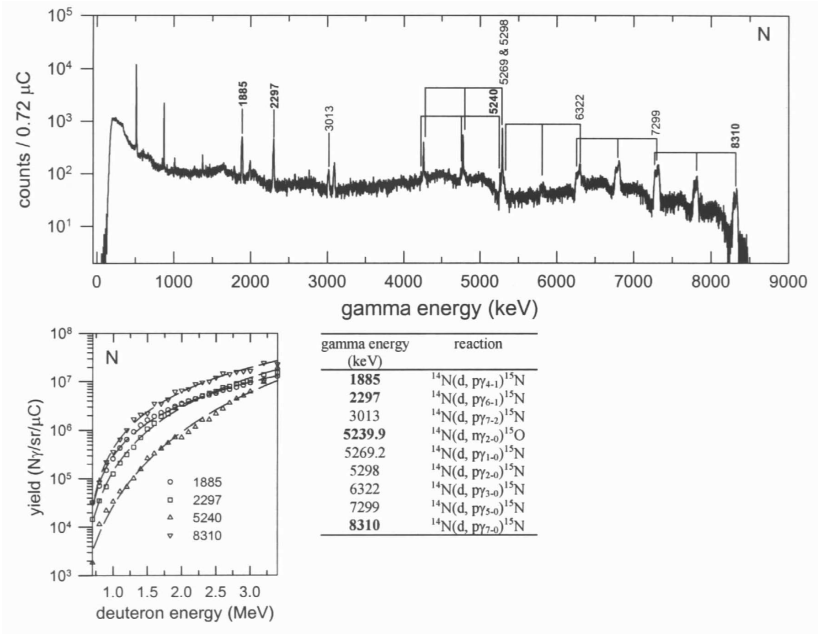

gamma energy (keV)	reaction
1885	$^{14}N(d, p\gamma_{4-1})^{15}N$
2297	$^{14}N(d, p\gamma_{6-1})^{15}N$
3013	$^{14}N(d, p\gamma_{7-2})^{15}N$
5239.9	$^{14}N(d, n\gamma_{2-0})^{15}O$
5269.2	$^{14}N(d, p\gamma_{1-0})^{15}N$
5298	$^{14}N(d, p\gamma_{2-0})^{15}N$
6322	$^{14}N(d, p\gamma_{3-0})^{15}N$
7299	$^{14}N(d, p\gamma_{5-0})^{15}N$
8310	$^{14}N(d, p\gamma_{7-0})^{15}N$

Figure 1.3.9 Spectrum, yield curves and tables with peaks for nitrogen. The spectrum was measured at E_d=1.8 MeV on TaN.

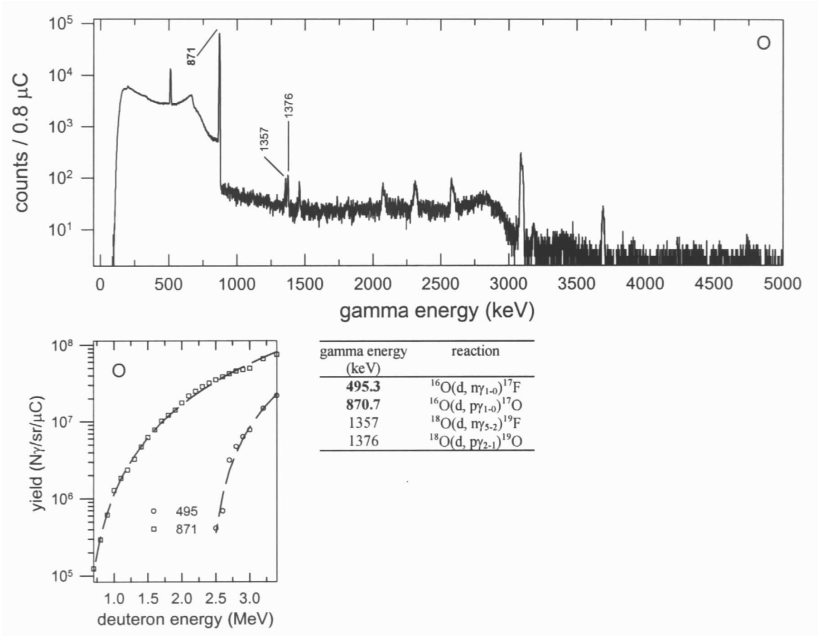

gamma energy (keV)	reaction
495.3	$^{16}O(d, n\gamma_{1-0})^{17}F$
870.7	$^{16}O(d, p\gamma_{1-0})^{17}O$
1357	$^{18}O(d, n\gamma_{5-2})^{19}F$
1376	$^{18}O(d, p\gamma_{2-1})^{19}O$

Figure 1.3.10 Spectrum, yield curves and tables with peaks for oxygen. The spectrum was measured at E_d=1.8 MeV on WO_3.

Table 1.3.3
Possible disturbing peaks appearing in a spectrum

E_γ [keV] [a]	Reaction
198	^{71m}Ge 22.7 γ + 175.2 γ
511	Annihilation
569	^{207}Pb(n, n'γ)
596	^{74}Ge(n, n'γ) ^{73}Ge(n, γ)
609	^{74}Ge(n, n'γ) ^{73}Ge(n, γ)
669	^{63}Cu(n, n'γ)
693	^{72}Ge(n, n'γ)
844	^{27}Al(n, n'γ)
847	^{56}Fe(n, n'γ)
871	^{16}O(d, pγ$_{1\text{-}0}$)^{17}O
1014	^{27}Al(n, n'γ)
1039	^{70}Ge(n, n'γ)
1238	^{56}Fe(n, n'γ)
1376	^{18}O(d, pγ$_{2\text{-}1}$)^{19}O
1461	Laboratory background
1779	^{28}Si(n, n'γ)
1811	^{56}Fe(n, n'γ)
1982	^{18}O(n, n'γ)
2210	^{27}Al(n, n'γ)
2313	^{13}C(d, nγ$_{1\text{-}0}$)^{14}C
3088	^{12}C(d, pγ$_{1\text{-}0}$)^{13}C
3684	^{12}C(d, pγ$_{2\text{-}0}$)^{13}C
3854	^{12}C(d, pγ$_{3\text{-}0}$)^{13}C

[a] Taken from references [Gih86, Ajz]

The measured absolute gamma-ray yields are listed in Table 1.3.4 for the most relevant peaks.

Table 1.3.4
Thick target absolute gamma-ray yields at deuteron energy of 1.8 MeV

	E_γ [keV] [a]	Yield [N_γ/sr/μC] (measured)	Yield [N_γ/sr/μC] (fitted)	Reaction
Li	429	1.10 (6) [b]	1.07 (6)	^{6}Li(d, nγ$_{1\text{-}0}$)^{7}Be
	478	2.31 (6)	2.45 (6)	^{6}Li(d, pγ$_{1\text{-}0}$)^{7}Li
B	953	1.09 (7)	1.03 (7)	^{11}B(d, pγ$_{1\text{-}0}$)^{12}B
	1674	1.36 (7)	1.28 (7)	^{11}B(d, pγ$_{2\text{-}0}$)^{12}B
C	3089	1.55 (7)	1.44 (7)	^{12}C(d, pγ$_{1\text{-}0}$)^{13}C
	3684	1.14 (6)	8.76 (5)	^{12}C(d, pγ$_{2\text{-}0}$)^{13}C
	3853.2 [d]	6.92 (4)	5.77 (4)	^{12}C(d, pγ$_{3\text{-}0}$)^{13}C

Table 1.3.4 (Continued)

	E_γ [keV] [a]	Yield [N_γ/sr/μC] (measured)	Yield [N_γ/sr/μC] (fitted)	Reaction
N	1885	2.56 (6)	2.44 (6)	$^{14}N(d, p\gamma_{4-1})^{15}N$
	2297	2.15 (6)	1.96 (6)	$^{14}N(d, p\gamma_{6-1})^{15}N$
	5239.9	5.46 (5)	5.53 (5)	$^{14}N(d, n\gamma_{1-0})^{15}O$
	8310	4.30 (6)	4.38 (6)	$^{14}N(d, p\gamma_{7-0})^{15}N$
O	495.3	-	-	$^{16}O(d, n\gamma_{1-0})^{17}F$
	870.7	1.22 (7)	1.18 (7)	$^{16}O(d, p\gamma_{1-0})^{17}O$
F	656	2.02 (6)	1.66 (6)	$^{19}F(d, p\gamma_{1-0})^{20}F$
	822.7	2.30 (5)	2.24 (5)	$^{19}F(d, p\gamma_{2-0})^{20}F$
	870.7	1.16 (6)	1.09 (6)	$^{19}F(d, \alpha\gamma_{1-0})^{17}O$
	983.5	3.57 (5)	3.31 (5)	$^{19}F(d, p\gamma_{3-0})^{20}F$
	1057	2.29 (6)	1.84 (6)	$^{19}F(d, p\gamma_{4-0})^{20}F$
	1309.2	4.25 (5)	3.40 (5)	$^{19}F(d, p\gamma_{5-0})^{20}F$
Na	350.7	6.61 (5)	6.08 (5)	$^{23}Na(d, \alpha\gamma_{1-0})^{21}Ne$
	472.2	4.68 (6)	3.84 (6)	$^{23}Na(d, p\gamma_{1-0})^{24}Na$
	1368.6	2.39 (6)	2.06 (6)	$^{23}Na(d, n\gamma_{1-0})^{24}Mg$
Mg	389.7	3.98 (5)	3.18 (5)	$^{24}Mg(d, p\gamma_{2-1})^{25}Mg$
	451.5	8.53 (5)	7.37 (5)	$^{24}Mg(d, n\gamma_{1-0})^{25}Al$
	585.0	1.66 (6)	1.44 (6)	$^{24}Mg(d, p\gamma_{1-0})^{25}Mg$
	974.7	4.61 (5)	3.86 (5)	$^{24}Mg(d, p\gamma_{2-0})^{25}Mg$
	1809	2.09 (5)	2.16 (5)	$^{25}Mg(d, p\gamma_{1-0})^{26}Mg$
Al	585.0	1.22 (5)	1.27 (5)	$^{27}Al(d, \alpha\gamma_{2-1})^{25}Mg$
	974.7 [c]	1.96 (5)	1.81 (5)	$^{27}Al(d, \alpha\gamma_{2-0})^{25}Mg$
	983 [c]			$^{27}Al(d, p\gamma_{2-1})^{28}Al$
	1014	9.94 (4)	8.46 (4)	$^{27}Al(d, p\gamma_{3-0})^{28}Al$
	2272	8.27 (4)	8.02 (4)	$^{27}Al(d, p\gamma_{9-0})^{28}Al$
	2839	1.09 (5)	1.17 (5)	$^{27}Al(d, p\gamma_{7-0})^{28}Al$
Si	755	5.76 (4)	4.73 (4)	$^{28}Si(d, p\gamma_{2-1})^{29}Si$
	1273	4.96 (5)	4.10 (5)	$^{28}Si(d, p\gamma_{1-0})^{29}Si$
	1384	1.07 (5)	1.07 (5)	$^{28}Si(d, n\gamma_{1-0})^{29}P$
	2028	2.26 (5)	2.11 (5)	$^{28}Si(d, p\gamma_{2-0})^{29}Si$
	2426	1.25 (5)	1.17 (5)	$^{28}Si(d, p\gamma_{3-0})^{29}Si$
	4934	6.42 (5)	5.90 (5)	$^{28}Si(d, p\gamma_{10-0})^{29}Si$
S	841.0	2.18 (5)	2.32 (5)	$^{32}S(d, p\gamma_{1-0})^{33}S$
Cl	671.4	2.11 (4)	2.25 (4)	$^{37}Cl(d, p\gamma_{1-0})^{38}Cl$
	788.4	5.66 (4)	5.16 (4)	$^{35}Cl(d, p\gamma_{1-0})^{36}Cl$
	1164.9	7.13 (4)	6.67 (4)	$^{35}Cl(d, p\gamma_{2-0})^{36}Cl$
	1951.1 [c]	1.45 (5)	1.30 (5)	$^{35}Cl(d, p\gamma_{4-0})^{36}Cl$
	1959.1 [c]			$^{35}Cl(d, p\gamma_{5-0})^{36}Cl$
	1970 [c]			$^{35}Cl(d, n\gamma_{1-0})^{36}Ar$
	2167	7.79 (4)	6.48 (4)	$^{37}Cl(d, n\gamma_{1-0})^{38}Ar$
K	770	4.29 (4)	4.34 (4)	$^{39}K(d, p\gamma_{2-1})^{40}K$
	2070 [c]	9.21 (3)	9.23 (3)	$^{39}K(d, p\gamma_{7-0})^{40}K$
	2074 [c]			$^{39}K(d, p\gamma_{8-1})^{40}K$
	3737	2.29 (4)	2.21 (4)	$^{39}K(d, n\gamma_{2-0})^{40}Ca$

Table 1.3.4 (Continued)

	E_γ [keV] [a]	Yield [N_γ/sr/μC] (measured)	Yield [N_γ/sr/μC] (fitted)	Reaction
Ca	1943	-	-	^{40}Ca(d, p$\gamma_{1\text{-}0}$)^{41}Ca
	2009.7	-	-	^{40}Ca(d, p$\gamma_{2\text{-}0}$)^{41}Ca

[a] Taken from references [Gih86, Ajz]
[b] (n) means x10^n
[c] Sum of gamma-ray yields are presented
[d] gamma-rays showing no Doppler broadening are indicated by their more precise energy. The lifetime of the respective excited state is $\tau \geq 1$ ps.

The bombarding energy of 1.8 MeV is chosen because it lies just below the neutron threshold (1.828 MeV) of the reaction ^{16}O(d,n)^{17}F. This resulted in the best peak to background ratio for samples containing oxygen. The precision of yields ranges from 15 to 25 %. It depends on the uncertainties in the determination of the net area of peaks, Kenny's matrix correction, detector efficiency, beam current and solid angle. Comparing the values with the ones in reference [Kis94], it can be concluded that in the majority of gamma-ray yields, the agreement is good. In most cases, the discrepancy is less than 15 %. However, for some values, larger differences can be observed due to the different background subtraction procedure and peak area calculation applied. The Table 1 in reference [Kis94] is completed and revised here with absolute yields of several other gamma-rays.

It was found that the measured yields could be fitted by a rather simple three-parameter function:

$$Y=Y_0 \cdot (E_d - E_{d0})^a$$

where Y is the absolute gamma-ray yield, E_d is the deuteron energy; Y_0, E_{d0} and a are the fitting parameters. These parameters and the fitting coefficient (R^2) for each element are listed in Table 1.3.5.

Table 1.3.5
Fitting parameters of the yield curves for the different gamma-ray peaks.
The equation used for fitting: $Y=Y_0 \cdot (E_d - E_{d0})^a$.

	E_γ [keV]	a	E_{d0}	Y_0	R^2
Li	429	2.9269	-0.4214	103232	0.9815
	478	2.4622	0.6608	17772644	0.9961
B	953	2.6153	0.4196	4453621	0.9963
	1674	2.5114	0.8506	14575754	0.9984
C	3089	2.1292	0.6689	11098039	0.9952
	3684	4.5781	0.2961	135347	0.9846
	3853.2	2.9054	1.5695	4104699	0.9907
N	1885	2.024	0.5647	1590121	0.9968
	2297	2.7811	0.4861	916118	0.9965
	5239.9	4.1438	0.2496	89940	0.9882
	8310	2.1905	0.5771	2820529	0.9959
O	495.3	2.0355	2.3656	21572890	0.9712
	870.7	2.3939	0.5142	6479876	0.9982
F	656	3.2476	0.4891	687615	0.9960
	822.7	3.0599	0.5552	114480	0.9929
	870.7	2.4548	0.5244	597070	0.9975
	983.5	2.7429	0.5876	195246	0.9957
	1057	2.6406	0.5618	1048293	0.9954
	1309.2	3.0362	0.4876	149100	0.9929
Na	350.7	3.1522	0.7166	472295	0.9979
	472.2	3.5221	0.5229	1622319	0.9961
	1368.6	4.0400	0.4141	551926	0.9962
Mg	389.7	3.4161	0.5952	168119	0.9914
	451.5	2.8606	0.7156	584246	0.9966
	585.0	3.0019	0.7175	1133471	0.9975
	974.7	3.0157	0.7054	293889	0.9967
	1809	2.5240	0.9176	296915	0.9931
Al	585.0	3.2138	0.8809	166725	0.9993
	974.7 983	3.5612	0.7738	165174	0.9978
	1014	3.2330	0.8524	100627	0.9971
	2272	3.4330	0.9264	125920	0.9969
	2839	4.0878	0.6051	56550	0.9961
Si	755	4.0876	0.6836	30144	0.9896
	1273	3.8388	0.7341	320773	0.9958
	1384	3.8851	0.8008	107290	0.9913
	2028	4.0038	0.7550	176509	0.9969
	2426	4.2567	0.6836	73313	0.9947
	4934	3.3891	0.7399	484414	0.9976
S	841.0	3.3142	1.0427	582204	0.9973

Table 1.3.5 (Continued)

	E_γ [keV]	a	E_{d0}	Y_0	R^2
Cl	671.4	22.3578	-4.8065	$1.044 \cdot 10^{-14}$	0.9901
	788.4	24.0028	-5.1816	$2.851 \cdot 10^{-16}$	0.9856
	1164.9	20.5251	-4.3094	$4.913 \cdot 10^{-12}$	0.9891
	1951.1				
	1959.1	8.8210	-0.3564	148	0.9829
	1970				
	2167	34.005	-8.9647	$5.231 \cdot 10^{-13}$	0.9869
K	770	4.7266	0.8648	59572	0.9989
	2070	2.8152	1.4428	167479	0.9892
	2074				
	3737	3.9341	1.1728	138203	0.9881
Ca	1943	6.9642	0.1577	1512	0.9873
	2009.7	1.9515	2.1699	1032335	0.9813

The R^2 coefficients show that rather good fits could be achieved. In order to illustrate this fact in another way, the calculated values at E_d=1.8 MeV from these fitted curves are also presented in Table 1.3.4. The differences between the *measured* and *calculated* yield values are generally less than 15 % which does not exceed the precision of the gamma-ray yields. The use of the above equation gives a useful tool in elemental analysis for concentration calculations. It should be noted, however, that in this way, it is assumed that the cross sections of the reactions vary smoothly with the deuteron energy, no compound reaction contribution to the direct reaction yield is taken into account. This is allowable because in most of the (d,p) and (d,n) reactions, the direct reaction mechanism is dominant. This type of reactions does not show sharp, well-separated resonances except few cases like oxygen at around 960 keV energy. (See, e.g., the pioneering work of Amsel and Samuel [Ams67] and also some later studies [Vic94, Gih86] in the reaction $^{16}O(d,p_1)^{17}O$ and $^{16}O(d,p\gamma_{1\text{-}0})^{17}O$ respectively). For thick samples, the contribution of the above mentioned resonance to the average gamma-ray yield is negligible, as it was shown by my calculations. On the other hand, it was mentioned earlier that the average stopping power method is the most accurate one in concentration evaluations.

Focusing on the individual spectra, the following statements can be given for carbon, nitrogen and oxygen (for the other elements a detailed discussion can be found in [Ele00]):

Several peaks originating from *carbon* via $^{12}C(d,p\gamma)$ reaction can be detected but only the peak of 3089 keV (the γ1-0 transition) has yield high enough for analytical purposes in the whole deuteron bombarding energy range. The yields of the 3684 and 3853 keV gamma-ray lines (from γ2-0, γ3-0 transitions, respectively) start playing more and more important role at deuteron energies above 1.8 MeV. The use of high energy gamma-rays requires the application of large volume detectors because the photopeak detection efficiency decreases with increasing gamma-ray energy. The (d,nγ) reaction channel is open for both ^{12}C and ^{13}C isotopes, but their gamma-ray yields are rather weak.

The spectrum collected using *nitrogen* target (TaN sample) is rich in peaks due to the numerous gamma-ray transitions in the residual ^{14}N nucleus, moreover, it is complicated by the strong escape peaks of the high energy gamma-rays. The peak at 8310 keV can be used for analytical purposes, however the net area of the 7301 keV peak contains the counts from the double escape peak of 8310 keV, therefore it was excluded from yield calculations. In reference [Kis94] the 5240, 5269 and 5298 keV peaks were not separated, and their yields were calculated together. Now only the yield for the 5240 keV peak is presented because at 5300 keV the double escape peak of 6322 keV appears, adding counts to the yields of the 5269, 5298 keV peaks.

The 871 keV *oxygen* (WO_3 sample) peak is very strong, however, if the unknown target contains high amount of fluorine, small correction should be applied in order to calculate the correct oxygen concentration, as a contribution to the yield may arise also from the reaction $^{19}F(d,\alpha\gamma_{1\text{-}0})^{17}O$. In this case, the 495 keV peak can also be employed for the identification of oxygen at higher deuteron energies.

The excitation function of the reaction $^{12}C(d,p\gamma)^{13}C$ was measured in the deuteron energy interval of 1.4-1.9 MeV and at 55° with respect to the beam

direction (Figure 1.3.6), since this experimental condition is often used and can be suggested for analytical purposes. The shape of the curve generally reflects that of the curve in [Try73] published for p_1 proton group deduced from the lineshape of the 3089 keV gamma-ray peak. In conclusion, it can be advised that for thick targets, 1.8 MeV deuteron energy should be used because in this way the complex resonance around 1.8 MeV can be integrated resulting higher gamma-ray dose with acceptable neutron hazard (10-100 μSv/h at the object slit and 1-3 μSv/h at the sample chamber). On the other hand, for thin targets, the highest yield can be achieved at 1.792 MeV, therefore this should be the recommended energy. The resonance at 1.4495 MeV ($\Gamma_{c.m.} \approx 7$ keV) [Ajz] can be easily used for carbon depth profiling if a thin (10-150 nm) surface layer is to be analyzed on a thick substrate (1 keV energy step means approximately 4 nm).

By measuring the geological and standard samples, the accuracy and the MDLs for the carbon and oxygen determination was tested. It was pointed out that the concentration values can be calculated with an uncertainty of 10 %, while the MDLs in iron matrix are 90 and 70 μg/g for C and O respectively.

2. APPLICATIONS IN THE FIELD OF ARCHEOLOGY AND GEOLOGY

This chapter includes my interdisciplinary research in archeology and geology which were carried out in cooperation with the Hungarian National Museum, Budapest, the Department of Classical Philology and the Department of Mineralogy and Geology of the University of Debrecen.

Subchapter 2.1 is devoted to some challenging archeological problems including analysis of Roman gems and their imitations, studies on prehistoric stone tool materials such as obsidian and radiolarite and investigation of one of the earliest artificial materials, pottery.

Subchapter 2.2 deals with the subject of geology, namely, the analysis of obsidians from the point of view of geological processes and examinations on magnetic spherules and their role in the answering of geological questions.

2.1 ARCHEOLOGY

2.1.1 ANALYSIS OF ROMAN GEMS AND THEIR IMITATIONS

Introduction

The claim to antique or looking like antique pieces of arts appeared in the era of the Renaissance, and this claim also reached Hungary [Mik94]. The manufacturing of imitations and business with them turned into a veritable branch of industry from the 17th century on.

One of the most popular group of antiques was engraved gems (Figure 2.1.1) which were used both for seal and jewel in the Antiquity. The exacting replicas and imitations meant, and means nowadays a serious pitfall for both collectors and specialists. For example, the most famous masters, as L. Natter and A. Pichler, signed their works, with Greek letters, but the other artists also wrote antique names on their products, which gave rise to the appearance of originality. Therefore, it has been getting more and more difficult to distinguish imitations and replicas from originals.

Figure 2.1.1 One of the studied engraved gems

Our aim was to analyze some imitations and to compare them with each other and original Roman samples, thus establishing to what extent they differ and how they can be separated from each other on the basis of their elemental compositions.

Description of the studied gems

In Table 2.1.1 some properties of the studied samples are summarized. Six imitations were analyzed and two specimens, an original Roman gem and a Roman glass, were chosen as reference materials. The selection from the extremely rich gem production of the 18th century occurred on the basis of the material and theme depicted on the ring stones. The selected specimens have the properties that the antique and antiquated representations appear on delusive faithful imitations of stone types preferred in the Antiquity.

Table 2.1.1
Features of the studied samples

Sample number	Origin	Engraving	Characteristics	Material
1	Wedgwood product, copy	Alexander the Great	black mat surfaces	clay with additives
2	Wedgwood product, copy	Cleopatra's suicide	black mat surfaces	clay with additives
3	18th copy Felix's work	Mercurius	polished to bright, air bubbles in glass matrix	glass-paste (supposed)
4	nicolo gem, copy	Mars and Minerva	plain polished surfaces	onyx
5	nicolo gem, copy	Amor riding a lion	plain polished surfaces	onyx
6	nicolo gem, copy	Sacrificing Amor	plain polished surfaces, air bubbles in glass matrix	glass-paste (supposed)
7	original roman gem	Bonus Eventus		
8	original roman glass			glass

Two nice pieces of the Modern Age collection of the Hungarian National Museum can be mentioned to illustrate the appearance and quality of the so-called black basalt. They were produced in the Wedgwood factory [Jän79], North-England in the 18th century. The base material of these objects was a mixture (essentially clay with various additives) worked out experimentally

during the production of ceramics. This mixture was pressed into steel form and backed to very hard.

The Hellenistic medal representation served as a model for a gem on which the portrait of Alexander the Great (sample 1) can be seen with ram horns. On an other gem, Cleopatra's suicide (sample 2) is shown in the modern age wording of the well-known story of Antique era.

From the Roman collection of the Hungarian National Museum, a black colored gem, which gives the impression of onyx (a type of quartz), was selected for the analysis (sample 3). Mercurius appears on it in three-quarters view. This is an excellent product of the classicism from the Augustus era made by Felix who worked at via Sacra. Its edge and back are mat. Fine granularity can be observed on the mat surface. Holding to light, it looks translucent. Its material seems to be glass-paste which was polished to bright. Air bubbles can also be recognized when using proper magnification.

One of the typical type of onyx, in which a thin light blue layer extends over a thick dark (black-blue-brown shaded) layer, is named nicolo after the Italian name of the mineral. The characteristic features of these stones are the following: both of their sides are plain, rims are oblique, edges are vertical, surfaces are polished. Their popularity is indicated by the fact that they were mass-produced from glass-paste later.

Three nicolo gems were investigated. In one of these gems, portraits of two persons in helmet can be seen (sample 4). It can not be decided whether the representation of Mars and Minerva, which can be mostly expected, or of two heroes or just two warriors is shown.

The other piece is a copy of a famous antique cameo (sample 5). Its dimension is just half of the original, Amor riding a lion are slimmer, the form of the lute is simpler.

The third nicolo gem is not a real copy, but an imitated composition: in front of an altar, Amor half knelt down sacrifices (sample 6). Little air bubbles appear at large optical magnification, which makes it possible that the gem was

made by glass-paste molding. The different material of the latter piece can be explored when light is transmitted through it. It does not let any light through, while the other nicolo gems are translucent.

Experimental

The analysis were carried out by PIXE and PIGE techniques in order to determine the major, minor and trace constituents.

For the PIXE measurements, a 2 MeV proton beam of 0.5 nA was supplied by the 5 MV Van de Graaff accelerator of ATOMKI. The experimental arrangement of the standard ATOMKI internal macrobeam PIXE facility is described in details elsewhere [Bor85]. A pair of characteristic X-ray spectra was taken on each sample with and without a 35 μm thick aluminum foil placed between the target and the X-ray detector to determine the concentrations of elements heavier and lighter than Fe respectively. The X-ray detector was a Canberra Si(Li) with an active area of 12.5 mm^2 and 155 eV resolution at 5.989 keV. The total charge collected in taking a spectrum amounted to 300 nC. The spectrum analysis, identification of the elements and assignment of concentration values were carried out with the program package PIXYKLM [Sza93].

In the PIGE measurements, the samples were irradiated by 3.8 MeV proton beam of 2-10 nA. The angle between the proton beam and the sample was 45°. 5 μC of charge was collected on each sample. A 100 cm^3 Harshaw Ge(Li) gamma-ray detector with a resolution of 2.4 keV at E_γ=1.33 MeV was mounted at 90° with respect to the beam direction at a distance of 19 cm from the target.

In order to investigate the reliability of the concentration values, more than one spectrum were taken on the samples. It turned out that the precision of the set-up is about 5-10 %.

Results and discussion

By means of the detection of the arising gamma- and X-rays, the concentrations of the following elements were determined: B, Na, Mg, Al, Si (with PIGE) and Al, Si, P, S, Cl, K, Ca, Ti, Cr, Mn, Fe, Co, Ni, Cu, Zn, Pb (with PIXE).

On the basis of these concentration values, a classification among the samples was performed. In Figure 2.1.2 the concentration ratios of Na/Si and Al/Si are shown from PIGE measurements, while in Figure 2.1.3 a similarity dendogram using PIXE data is displayed. The dendogram was produced through cluster analysis using STATISTICA program package [Sta]. Both figures, i.e., the results of the two different techniques of elemental analysis, clearly show the separation of samples 4, 5, 7 into the same group (Group I.). It can be concluded that the same type of mineral was used to make the imitations for the samples 4 and 5 as for the authentic Roman gem (sample 7).

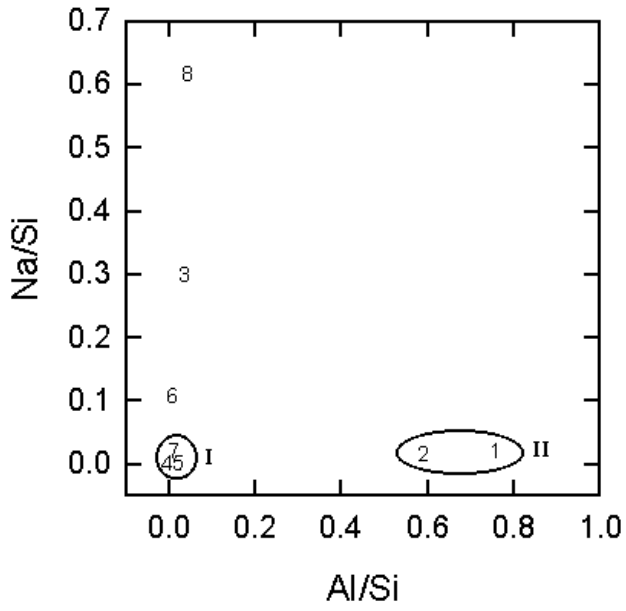

Figure 2.1.2 Na/Si vs. Al/Si elemental ratios of the samples from PIGE measurements

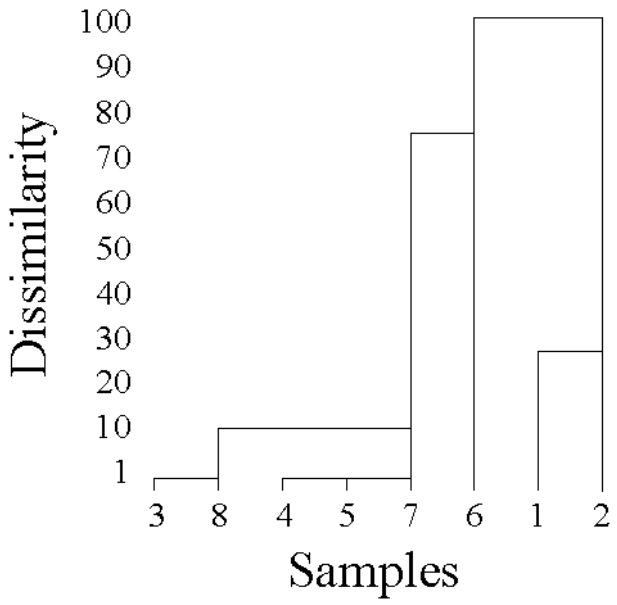

Figure 2.1.3 Dissimilarity dendogram of the samples using PIXE data

The members of the next group (samples 1 and 2) represent the 19th century complex composition of Wedgwood products (Group II.). On the basis of both PIXE and PIGE analysis, it can be stated that the elemental composition of these gems differs remarkably from the onyx mineral and the glass pastes. The remaining samples (3, 6 and 8) have the highest Na content. On the basis of the composition of the original Roman glass (sample 8), one can suppose that both of the samples 3 and 6 are made from sodium glass. Nevertheless, Figure 2.1.3 shows that sample 6 is quite different from samples 3 and 8. The similarity of samples 3 and 8 confirm the initial assumption, i.e., the base material of gem Mercurius (sample 3) is made of glass-paste. Our analysis shows that the nicolo "Sacrificing Amor" (sample 6) is made of glassy material, but its boron content indicates that it is different from the Roman glass, therefore its glass-paste can not be of Roman origin.

2.1.2 INVESTIGATION OF RADIOLARITE STONE TOOLS

Introduction

Radiolarites (Figure 2.1.4) belong to the group of sedimentary siliceous rocks. As the name indicates, it is formed of *Radiolaria* (Figure 2.1.5), i.e., the skeletal elements of siliceous unicellular beings. Apart from siliceous sponges and diatoms, *Radiolaria* is the most important biogene source for the formation of sedimentary siliceous rocks. They are present in the seas and oceans since at least the Paleozoic period.

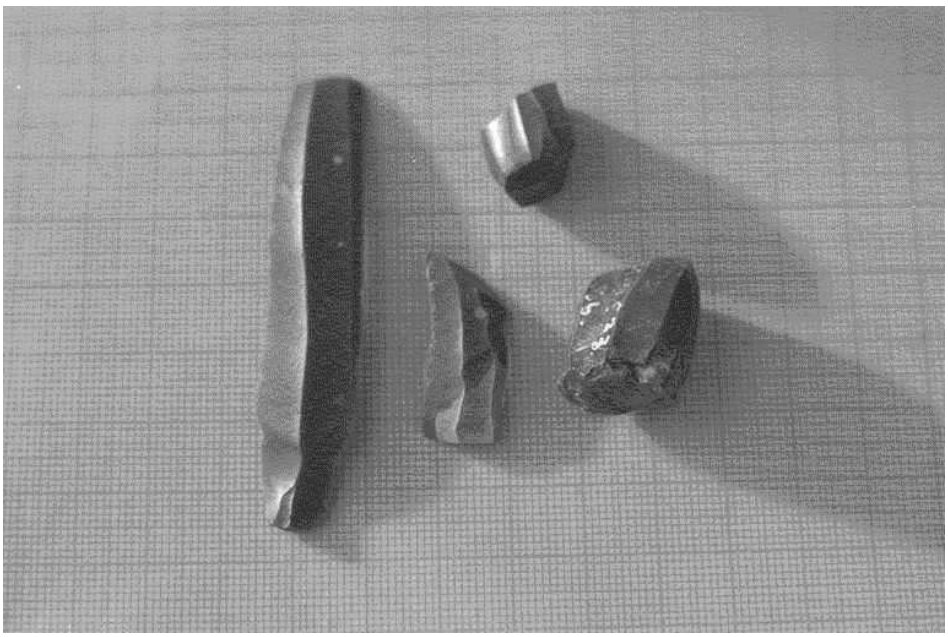

Figure 2.1.4 Radiolarite stone tools

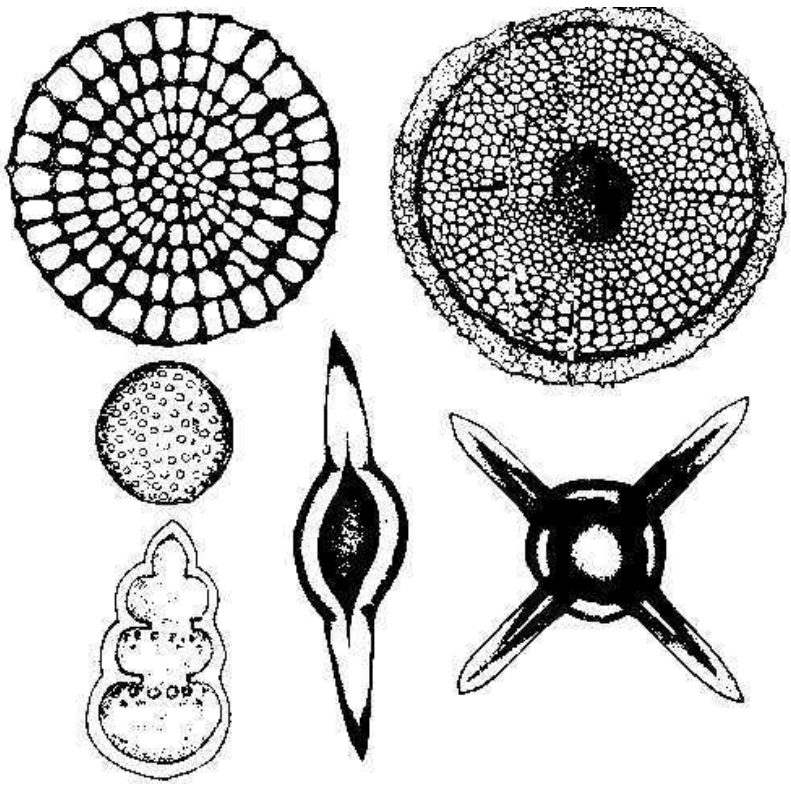

Figure 2.1.5 *Radiolaria* with various structures (their size in nature varies between 10 and 100 μms)

Being small in size (10-100 μm), Radiolaria accumulates in radiolarian silt very slowly, by a rate of some cm per million years. The mass occurrence of *Radiolaria* and formation of radiolarite in Hungary took place mainly in the Mesozoic period when the world ocean (Tethys) was of equatorial position. Radiolarite was formed in a long, west-eastern arch along the Alp-Carpathian system, across the Balkans till the Himalayas.

Radiolarites, as it has been demonstrated by recent petroarcheological and archeological research, have special importance for prehistory [Bir91, Gro97]. In large parts of Central and Southern Europe, mainly to the south of the Cretaceous and Tertiary flint zones, the basic supply of siliceous rocks for chipped stone artifacts, "silex" in general, was radiolarite. Recognition of radiolarite among archeological lithic raw materials is also fairly

recent. At the same time, separating the material coming from different radiolarite sources is far not easy. There are several color variants, but the macroscopical type groups distinguished mainly on the basis of color do not necessarily agree with actual sources.

The consequent elemental analysis of radiolarites in large numbers was not carried out before. Therefore, this IBA study can be regarded as a pioneering work which provide primary knowledge on the distribution of concentration values measured for samples with different geographical locations.

Our main question, when starting the analyses, was the following. To what extent are we able to characterize the radiolarite source areas by ion beam methods ? In order to answer this, we should

- separate radiolarite from other raw materials frequently used (e.g., obsidian, limnic quartzite, hydroquartzite) in the Carpathian Basin
- discriminate the individual source areas from each other
- find out whether existing macroscopical grouping based on physical qualities, mainly color, has anything to do with differences in chemical composition
- check some "macroscopically grouped" pieces against their potential sources.

Description of the analyzed samples

Experiences on source-collected material and macroscopical characterization of archeological lithic material allowed the grouping presented in Table 2.1.2.

Table 2.1.2
Radiolarite types in Hungarian (archeological and geological) lithic material separated macroscopically

Nr [a]	Type name	Geological age [b]
4	Carpathian radiolarite - "blue silex"	J3
5	Carpathian radiolarite, marble dark red	J3
6	Carpathian radiolarite, dark brownish-red	J3
7	Carpathian radiolarite, gray	J3
8	Carpathian radiolarite, other	J3

Table 2.1.2 (Continued)

Nr [a]	Type name	Geological age [b]
9	Transdanubian radiolarite - Szentgál radiolarite, vivid red	J2
10	Transdanubian radiolarite - Úrkút-Eplény radiolarite, mustard yellow	J2
11	Transdanubian radiolarite - Hárskút radiolarite, orange shaded brown	J2
12	Transdanubian radiolarite - Tata type radiolarite, liver-colored	J2
13	Transdanubian radiolarite, reddish brown	J2
14	Transdanubian radiolarite - Sümeg radiolarite, bluish gray	C1
15	Transdanubian radiolarite, other	J2
16	Mecsek radiolarite, dark red	J3
17	Mecsek radiolarite, gray	J3-C1
18	Mecsek radiolarite, other	J3
19	Transdanubian radiolarite - Gerecse region	J2-J3
20	Bükk radiolarite	J1-2
21	unspecified radiolarite	

[a] Numbers are given according to macroscopical type groups of Hungarian chipped stone lithic raw materials [Bir98]
[b] The abbreviations refers to the different periods in the Mesozoic era, i. e., J=Jurassic, C=Cretaceous

It should be noted that this table was made focusing on Hungarian archeological material. Therefore, Hungarian radiolarite sources and types are well represented, while some important radiolarite sources, which were not unambiguously identified in Hungarian lithic material yet, are just "lumped together" under "unspecified radiolarite". This collective term means radiolarites coming from Transylvania, especially the Maros valley, radiolarite from the Southern Carpathians or the Vienna Basin. The Lithotheca collection of the Hungarian National Museum has some examples from these source regions, but the petroarcheological cognizance of these regions is not adequate yet.

Samples were selected for the purpose of analysis both from geological and archeological sites. Geological ones were chosen from the Lithotheca collection from localities representing most of the known radiolarite source regions of the Carpathian Basin. The specimens are listed and described in Table 2.1.3. Some pieces were previously analyzed by G. Newton, Manchester

with neutron activation analysis (NAA)[3]. The results were published in the first volume of the Lithotheca catalogue [Bir91a]. The samples for which we have control data by NAA are marked by asterisks in table 2.1.3.

Table 2.1.3
Description of the samples

Sample number	Source region/ hypothetical source region and geological age	Site or source	Character of the sample	Macroscopical type group and description [a]
*1	Bakony J2	Városlőd-Savóvölgy	geological	10 dark mustard yellow
2	Bakony J2	Városlőd-Savóvölgy	geological	10 dark mustard yellow
3	Bakony J2	Városlőd-Savóvölgy	geological	11 brown
4	Bakony J2	Városlőd-Savóvölgy	geological	10 orange shade mustard yellow
5	Bakony J2	Városlőd-Savóvölgy	geological	9 red
*6	Bakony J2	Városlőd-Savóvölgy	geological	15 orange-reddish brown
7	Bakony J2	Szentgál-Tűzköveshegy	geological	15 skin-colored porcelanite
8	Bakony J2	Szentgál-Tűzköveshegy	geological	9 red
9	Bakony J2	Hárskút-Édesvízmajor	geological	9 red
10	Bakony J2	Hárskút-Édesvízmajor	geological	9 red fragment from varicolored piece
11	Bakony J2	Bakonycsernye-Tűzkövesárok	geological	13 reddish brown
12	Bakony J2	Bakonycsernye-Tűzkövesárok	geological	9 red
13	Bakony J1	Lókút-Hosszú árok	geological	9 red
14	Bakony K1	Sümeg-Mogyorósdomb	geological	14 bluish gray radiolarian chert
15	Bakony K1	Sümeg-Mogyorósdomb	geological	14 bluish gray radiolarian chert

[3] Only Fe is the common element which was determined by NAA and IBA, therefore a detailed comparison of the results can not be given.

Table 2.1.3 (Continued)

Sample number	Source region/ hypothetical source region and geological age	Site or source	Character of the sample	Macroscopical type group and description [a]
16	Gerecse J2-3	Agostyán-Lőtér	geological	19 reddish gray
17	Gerecse J2-3	Lábatlan-Tölgyhát	geological	19 liver-colored
18	Gerecse J2-3	Lábatlan-Tölgyhát	geological	19 liver-colored
19	Gerecse J2-3	Lábatlan-Vöröskőbánya	geological	19 reddish brown
20	Gerecse J2-3	Lábatlan-Pisznice tető	geological	19 liver-colored
21	Gerecse J2-3	Lábatlan-Pisznice tető	geological	19 bluish gray
22	Gerecse J2	Tata-Kálváriadomb	geological	19 liver-colored
23	Mecsek J3	Kisújbánya-Kistuft	geological	16 dark (brownish) red
24	Mecsek J3-K1	Kisújbánya-Márévári völgyfő	geological	17 silky gray
25	Mecsek J3	Hosszúhetény-Csengő hegy	geological	17 silky gray
26	Mecsek J3	Hosszúhetény-Csengő hegy	geological	16 dark (brownish) red
27	Carpathian J3	Trencinska Bohuslavice	geological	6 dark red
28	Carpathian J3	Trencinska Bohuslavice	geological	4 bluish gray
29	Carpathian J3	Trencinska Bohuslavice	geological	5 greenish gray
30	Bakony J2	Zengővárkony	archeological	9 Red
31	Mecsek J3	Zengővárkony	archeological	17 silky gray
32	Mecsek J3	Zengővárkony	archeological	16 dark (brownish) red
33	Mecsek J3	Zengővárkony	archeological	17 silky gray
34	Mecsek J3	Zengővárkony	archeological	17 silky gray with cream-rosy shade
35	Austria	Vienna-Mauern	geological	dark mauve red
36	Austria	Vienna-Mauern	geological	bluish gray
37	Bakony J2	Szentgál-Tűzköveshegy	geological	15 skin-colored porcelanite

Table 2.1.3 (Continued)

Sample number	Source region/ hypothetical source region and geological age	Site or source	Character of the sample	Macroscopical type group and description [a]
38	Bakony J2	Szentgál-Tűzköveshegy	geological	9 red
39	Bakony J2	Szentgál-Tűzköveshegy	geological	9 red
40	Bakony J2	Szentgál-Tűzköveshegy	geological	13 reddish brown
41	Carpathian J3	Arka	archeological	6 dark (brownish) red
42	Carpathian J3	Arka	archeological	6 dark red
43	Carpathian J3	Bodrogkeresztúr	archeological	4 bluish gray
44	Carpathian J3	Bodrogkeresztúr	archeological	8 dark red part of a bluish gray piece with dark red rim
45	Carpathian J3	Bodrogkeresztúr	archeological	6 dark red
46	Stone marrow	Bodrogkeresztúr	archeological	- hydroquartzite with kaoline
47	Limnic quartzite	Bodrogkeresztúr	archeological	- bluish white, slightly translucent
48	Bakony J2	Csabdi	archeological	10 dark mustard yellow with white porcelanite
49	Bakony J2	Csabdi	archeological	10 dark mustard yellow with white cortex
50	Bakony J2	Csabdi	archeological	9 red
51	Bakony J2	Szentgál-Teleki dűlő	archeological	9 red
52	Bakony J2	Szentgál-Teleki dűlő	archeological	9 red
53	Bakony J2	Szentgál-Teleki dűlő	archeological	9 red with porcelanite
54	Greece	Koziakas, Thessaly	geological	- dark red
55	Greece	Koziakas, Thessaly	geological	- dark red

[a] Numbers refer to the grouping in Table 2.1.2

The geological and archeological sites, from which the samples originate, are well-known raw material sources and important archeological sites for lithic archeology. They are not described here, however information on them can be found in the literature [Lec95, Wei99, Rut70, Bár79, Ard78, Vér65, Dob00, Dom60, Bác89, Ant90, Bir98, Ant82, Bir91].

Experimental

The samples were cleaned only with pure alcohol (because they were flat and plain enough for the analysis) and irradiated by proton beam supplied by the 5 MV Van de Graaff accelerator of ATOMKI. The experiments were carried out at the nuclear microprobe unit because this allowed a precise current measurement and easy sample manipulation in case of some specimens having small dimensions (about 1 mm^2). On the other hand, the homogeneity had to be checked, since the determination of the bulk composition was required. It turned out that the radiolarite samples were quite homogeneous (the concentration values derived from measurements taken on different spots of the samples varied only within the range of their statistical errors), but strong inhomogeneities were found in porcelanite samples (e.g., sample 38) considering their major and minor components. However, the trace elements - used for provenancing later - were uniformly distributed.

For PIGE analysis, the proton energy, collected charge, beam current, beam spot size and scanned area were 3.5 MeV, 10 μC, 5 nA, 10 μm x 10 μm and 50 μm x 50 μm respectively. The beam energy of 3.5 MeV was chosen because the gamma-ray yields from light elements are high enough at this energy to allow a fast determination of the elemental concentrations, and what is more important, it is above the quite strong resonance (at 3.1 MeV) of the reaction $^{28}Si(p, p'\gamma)^{28}Si$ [Gea74], thus making the detection of gamma-photons from silicon easier. The other beam parameters were adjusted so that the current density did not exceed 25 $pA/\mu m^2$ because a higher current density could alter the original composition of the samples [Tou93].

The gamma-rays were detected by the CLOVER-Ge-BGO detector system. The spectra were evaluated by the computer code Physics Analysis Workstation (PAW, from CERN, Geneva).

The PIXE study was done in two steps. Although the characteristic X-rays were detected by using a common Si(Li) detector in both cases, only the Hostaphan filter of 24 μm was first applied before the entrance window of the detector, while in the second run, the aluminum filter of 98.8 μm was also mounted. The proton energy, collected charge, beam current, beam spot size and scanned area were 2 MeV, 0.04 μC (5 μC with aluminum filter), 0.03 nA (2 nA with aluminum filter), 10 μm x 10 μm and 50 μm x 50 μm respectively. The concentration of elements in the region of $14<Z<24$ was determined in the first run, while the other constituents were measured in the second step up to zirconium.

Results and discussion

Concentration values of 24 elements were determined by ion beam methods, namely, F, Li, Al, Na, Si, P, S, Cl, K, Ca, Ti, V, Cr, Mn, Fe, Co, Ni, Cu, Zn, As, Rb, Sr, Y, Zr.

The samples, which are not radiolarites, could be separated on the basis of their potassium, rubidium and iron contents. The "stone marrow" sample contained extremely high amount of potassium and rubidium, while the limnic quartzite had low concentration in potassium and iron comparing with the average values in radiolarites.

Utilizing the geological samples, natural clusters can be formed such as Bakony, Mecsek, Gerecse, Carpathian, Greek and Vienna groups.

It was found that only few elements, namely, Ni, Cu, Zn characterize the provenance, since either the mean values for the other elements are not different from each other or the standard deviations are quite high to make any distinctions. On the basis of the concentration data of the indicator elements mentioned above, a cluster analysis was carried out using STATISTICA software

(developed by Microsoft) [Sta]. It seemed that three or four rational and interpretable clusters can be given. Therefore, the so called k-means clustering was employed in the analysis. The purpose of this type of clusterization is to classify objects into a pre-specified number of clusters. The algorithm moves objects into different clusters with the goal of minimizing the within-cluster variability, while maximizing the between-cluster variability.

The samples attached to each other into the different clusters can be seen in Table 2.1.4. The archeological specimens are in italics. The first cluster contains samples from the Vienna-basin and the Transdanubian object from Tata (type number 12). In the second and fourth clusters, mainly Carpathian and Transdanubian (from Gerecse region, type number 19) samples and the pieces from Greece can be found. Some Transdanubian specimen from the Bakony region (type numbers 9, 10, 11, 12, 13, 14, 15) and few archeological pieces are added to these groups. The third cluster is the group of the Transdanubian samples from Bakony region. Several archeological specimens with various provenances are linked to this cluster.

Table 2.1.4
Clusters with samples linked to each other

Cluster			
1	2	3	4
22, 35, 36	17, 18, 55	1, 2, 3, 4, 5, 6, 7, 8, 9, 10, 11, 12, 13, 14, 15, 23, 24, 25, 26, 28, *30*, *32*, *33*, *34*, 37, 39, 40, *41*, *43*, *44*, *45*, *49*, *50*, *51*, *52*, *53*	16, 19, 20, 21, 27, 29, *31*, 38, *42*, *48*, 54

In Table 2.1.5 the mean values and the standard deviations of the clusters are shown for the different elements, i.e., for the variables in the three-dimensional space. For the measurement of the distances, the Euclidean distance was employed. In order to illustrate the distances between clusters, the three-dimensional space is projected to a plane (Figure 2.1.6) where the two variables are Cu and Zn.

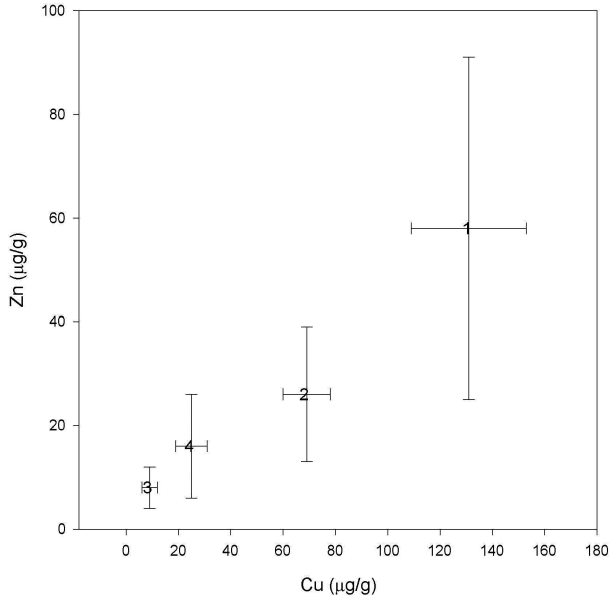

Figure 2.1.6 The localization of the clusters in the Cu-Zn plane

Table 2.1.5
Descriptive statistics for the clusters

	Mean value (standard deviation)			
	Cluster 1	Cluster 2	Cluster 3	Cluster 4
Ni	125 ± 54	26 ± 35	6 ± 1	10 ± 9
Cu	131 ± 22	69 ± 9	9 ± 3	25 ± 6
Zn	58 ± 33	26 ± 13	8 ± 4	16 ± 10

The concentration data were also investigated from the point of view whether there are correlations between them and the color of the samples, however no relations could be found.

2.1.3 STUDY ON ARCHEOLOGICAL OBSIDIANS

Introduction

Obsidian (Figure 2.1.7) is a glassy material which emerge during the rapid chilling of lava of high silicon content. It was widely used for tool-making by prehistoric men, especially during Neolithic times because it was easy to form different objects such as blades, arrowheads, scrapers and knives from the volcanic glass. Chemical and physical properties of this natural glass, as obtained from different volcanic sectors, are peculiar of the specific occurrence and allow their discrimination. Obsidian is also an ideal material for provenance studies and a unique material which can be used for reconstructing ancient exchange networks and cultural relations between different populations in the prehistoric epoch.

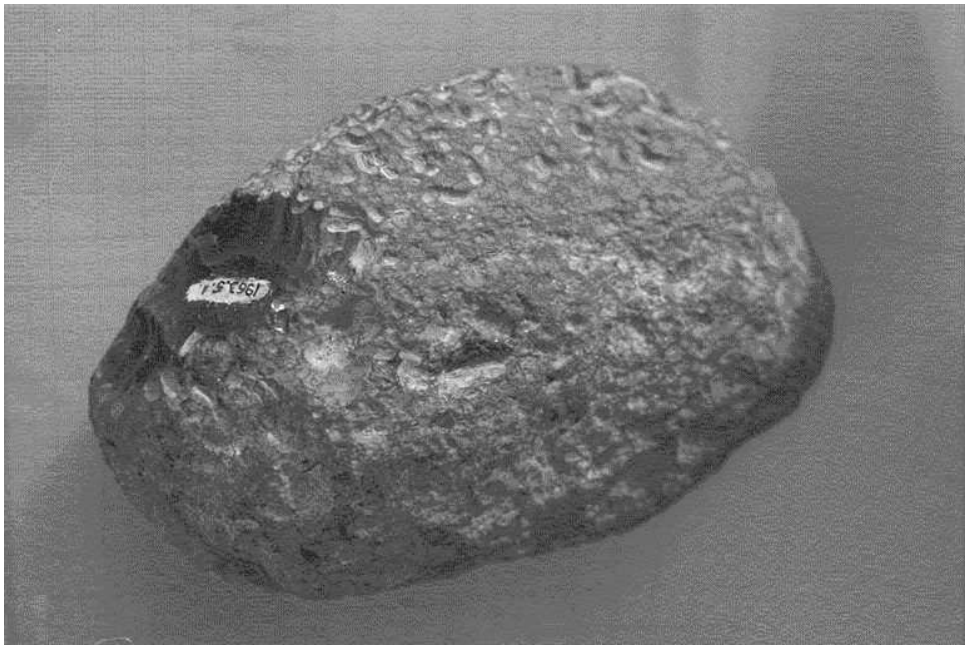

Figure 2.1.7 Natural obsidian lump

In addition to the Mediterranean (Greece, Turkey, Italy) and Caucasus (Armenia), obsidian turns up in large numbers in Europe only in the

Carpathian Basin, or more precisely in the region of the Tokaj-Presov Mts. which belongs to Slovakia and Hungary today. From time to time, this rare and valuable volcanic glass could be the reason for sudden migration or slow infiltration of people and also for powerful conflicts. On the other hand, wide-ranging connections and trade routes were formed with many distant archaeological sites in Europe.

The obsidian samples were widely investigated by different chemical and physical methods earlier (summarized in [Tho95]). IBA techniques are also included (e.g., [Bir78, Bel99]) because they are non-destructive, which is essential for archeological specimens, and do not require any sample preparation. The obsidians from the Tokaj Mts. were analyzed by Biró et al. with the use of an electron microprobe and found two main groups of Slovakian and Hungarian objects, while the Hungarian sources were separated into two subclusters [Bir91]. However, ion beam analysis of Hungarian obsidians were not carried out in large numbers before.

In this study, the proposed object was to chemically characterize Carpathian obsidians with all the possible localities by PIXE and PIGE methods, thus fingerprinting the geological sources, to find new subgroups if there is any and to build a compositional database for them in ATOMKI. It was also aimed to classify several archaeological samples found at an important Paleolithic settlement, Bodrogkeresztúr-Henye and to reveal distant linkage to this site or to confirm the assumption that these materials are local or mesolocal.

Description of the investigated obsidians and Bodrogkeresztúr-Henye site

Table 2.1.6 contains the analyzed obsidians which cover all the Carpathian sources explored earlier (Mád, Tolcsva-Erdőbénye, Viničky) [Bir91, Tho95]. Many other geological samples with different localities were studied in order to compare them with the Carpathian ones.

Table 2.1.6 Sample number and locations

Number	Location
1	Tolcsva, Tokaj Mts., Hungary
2	Erdőbénye, Tokaj Mts., Hungary
3	Sima, Tokaj Mts., Hungary
4	Jerevan, Armenia
5	Teotihuacan, Mexico
6	Hrafutinnusker, Iceland
7	Erdőbénye, Tokaj Mts., Hungary
8	Tolcsva, Tokaj Mts. Hungary
9	Tolcsva, Tokaj Mts., Hungary
10	Mád, Tokaj Mts., Hungary
11	Viničky, Slovakia
12	Kömürcü Köyü, Turkey
13	Jerevan, Armenia
14	Karacaören, Turkey
15	Lipari Island, Italy
16	Tolcsva, Tokaj Mts., Hungary
17	Tolcsva, Tokaj Mts., Hungary
18	Tolcsva slope, Tokaj Mts., Hungary
19	Tolcsva slope, Tokaj Mts., Hungary
20	Tokaj-Lebuj (perlite), Tokaj Mts., Hungary
21	Erdőbénye, under Mondoha, Tokaj Mts., Hungary
22	1 km west from Erdőbénye, Tokaj Mts., Hungary
23	Erdőbénye, Mondoha slope, Tokaj Mts., Hungary
24	Erdőbénye, Tokaj Mts., Hungary
25	Mád, Kakas hill, vineyard I., Tokaj Mts., Hungary
26	Mád, Kakas hill, vineyard I., Tokaj Mts., Hungary
27	Mád, near the winehouse, Tokaj Mts., Hungary
28	Mád, at the winehouse, Tokaj Mts., Hungary
29	Vinicky, Tokaj Mts., Slovakia
30	Vinicky, Tokaj Mts., Slovakia
31	Melos-Demenegaki, Greece
32	Melos-Demenegaki, Greece
33	Melos, Greece
34	Melos-Adamas, Greece
35	Melos, Greece
36	Antiparos
37	Antiparos
38	Yali Island, Greece
39	Yali Island, Greece
40	Yali Island, Greece
41	*Bodrogkeresztúr-Henye, Hungary*
42	*Bodrogkeresztúr-Henye, Hungary*
43	*Bodrogkeresztúr-Henye, Hungary*
44	*Bodrogkeresztúr-Henye, Hungary*

The archeological samples in italics are from Bodrogkeresztúr-Henye hill which is one of the classical sites of the Hungarian Upper Paleolithic. It belongs to the so-called Gravettian complex and dated to 28000 B.P. [Dob00]. The most important raw materials at this site are local (South-Tokaj) limnic quartzite, local and Slovakian obsidian, a special local raw material „stone marrow", a hydroquartzite related to kaolinite occurring also locally. Apart from this, a large number of regional „imported" raw materials including radiolarite was reported from this site [Dob00]. However, even supposing gravel pebble resources for radiolarite, this site lies much far from possible outcrops.

Experimental

The samples were cleaned with pure alcohol and bombarded by proton beam at the nuclear microprobe facility. This technique was used because it was well-known that obsidian may contain minerals at micrometer scale, therefore these inhomogeneities should have been explored and excluded from the bulk measurements[4]. The experimental conditions were similar to that of radiolarite study, hence only the data on beam parameters are listed here.

For PIGE analysis, the proton energy, the collected charge, beam current, beam spot size and scanned area were 3.5 MeV, 3 μC, 1 nA, 10 μm x 10 μm and 1000 μm x 1000 μm respectively.

The PIXE study was carried out in two runs as in case of radiolarites (with and without the aluminum filter in front of the Be-windowed detector). The proton energy, collected charge, beam current, beam spot size and scanned area were 2 MeV, 0.04 μC (1 μC with aluminum filter), 0.03 nA (1 nA with aluminum filter), 10 μm x 10 μm and 1000 μm x 1000 μm respectively.

The ion beam measurements were completed by LA-ICP-MS analysis in Orléans [Gra99]. This device is capable of determining concentrations of almost all the stable elements of the periodic table at μg/g level. However, it probes the

[4] However, they can give additional geochemical information on the lava flows, as it is presented in subchapter 2.2.1.

bulk of the samples, and furthermore, standards should be used during the evaluation of the spectra.

Results and discussion

By means of PIGE and PIXE techniques, 20 elements were detected. Among these elements, Na, Al, Si, K, Ca and Fe as major constituents, while Li, F, P, Cl, Ti, Mn Cu, Zn, Rb, Sr, Y Zr, Nb, Ba as minor or trace ones were determined.

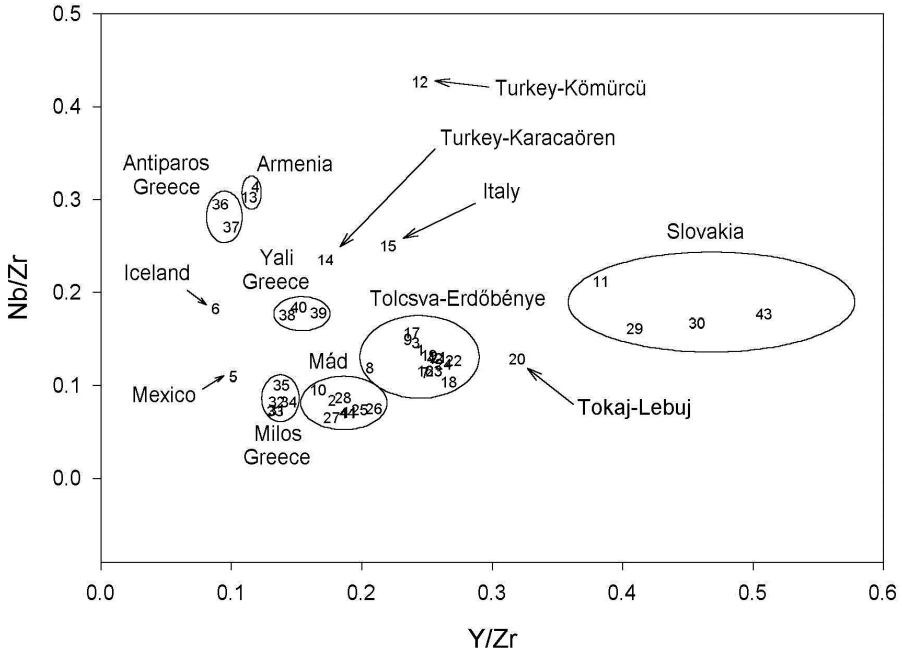

Figure 2.1.8 Classification of the studied obsidian samples on the basis of Y/Zr and Nb/Zr elemental ratios

In Figure 2.1.8 the position of the samples is displayed in a two-dimensional plot of Y/Zr vs. Nb/Zr. These elements remain stable during the production and evolution of obsidian, therefore they adequately characterize the lava flows, in this way the geographical sources. As a result, it is clear that ion beam techniques could sharply separate the different source areas and confirmed

the fact found earlier by electron microprobe measurements that only the following geological sources existed in the Carpathian basin: Mád, Tolcsva-Erdőbénye, and Viničky. A proper and wide database was created in ATOMKI, thus allowing the classification of any Carpathian archeological obsidian with an unknown provenance in the future.

Two of the samples collected at the site Bodrogkeresztúr-Henye fall into the group of Mád, and the clusters Tolcsva-Erdőbénye and Viničky also contain each. It means that it can be stated that these materials are local/mesolocal and do not show any evidence for linkage to other sites. In other words, the archeological assumption is still correct, i.e., the people at this site exploited the sources of the area and did not use obsidian and radiolarite material or tools of distant provenances.

2.1.4 ANALYSIS OF PREHISTORIC POTTERY

Introduction

Pottery, one of the earliest artificial materials, raises a number of questions in archeology. It is generally known that typological sequences based on pottery form and style constituted the relative chronological scheme of the periods prior to the appearance of writing and general use of metals. Even in periods dated by written evidence, pottery serves as an important marker for culture and date. However, much less can be found about the raw material of pottery finds and their possible indication for provenance, technology and dating.

Pottery consists of raw and additive materials, clay and/or loam and temper, formed wet into shape, fired at variable temperatures and used for storage and domestic purposes. The appearance of fired clay dates back well into the Paleolithic period, but its regular applications as vessels is one of the hallmarks of the first productive economies, i.e., the Neolithic period. It could be assumed that the materials of all the prehistoric potteries were basically local and originated from clay localities on the site; pottery temper - various additives to enhance physical qualities like $CaCO_3$, Fe_2O_3, SiO_2, scale, biotite, different feldspars, especially prevent shrinkage and cracking during firing of the pottery - most probably was constituted mainly of materials also available locally. Knowing the „picky" choice of prehistoric people in selecting their lithic raw material stock, this is not necessarily true [Bir98a]. Even assuming a basically local origin for most contents of pottery, we can expect much variety in technology and finish. Furthermore, as a rule, it is known that prehistoric pottery could travel long distances as container of other goods or on its own merit for artistic beauty already in the Neolithic period [Kal77].

The chemical characterization of prehistoric pottery is a rapidly developing field of archaeological research [Man88, Kil88, Sán98, Shr99 , Ont00]. Due to the complexity of the problem, the archeometrical study of prehistoric pottery started much later than other, more „simple" materials like glasses or metals. It is not

quite clear what is mirrored: place of origin or production technology or workshop. The chemistry and mineral composition of the pottery vessels are the resultant of all these factors which are very difficult to separate [Sil00]. It is not by chance that fingerprinting pottery had been effective first in the case of vessels with very strict technological processing technique, i.e., terra sigillata [Bal88]. Recent investigations on prehistoric pottery in Hungary concentrated mainly on temper mineralogy of Bronze Age/Early Iron Age pottery from the Western parts of Transdanubia [Ghe99].

In this study, material from one excavation site representing several chronological periods was selected. The aim was to see whether there are differences in choice of raw material, production technology within the shards from different periods and how much the differences can be explained, if there are any. For this purpose, the nuclear microprobe technique was applied with the small beam size, which beside the bulk composition and mineral inclusions, allow to observe other temper materials (like seashell pieces).

Description of the site and the samples

The archaeological site chosen as the object of analysis is the northernmost settlement for one of the earliest Neolithic populations in the Carpathian Basin, the so-called Starčevo culture. The site Vörs is located in the south of lake Balaton, in the middle of the Kis-Balaton marshes. Probably, it used to be a protruding long peninsula in the Prehistoric period when the water level of lake Balaton was much higher than today. The environs of Vörs is extremely rich in archaeological remains: almost all archaeological periods are represented, which is partly due to the favorable natural endowments of the region, but also to intensive archaeological work conducted here over several decades. The site Máriaasszonysziget itself contains the archaeological heritage of several cultures, both in prehistory and historical periods.

On the earlier excavation by Cs. Aradi, rich Neolithic material turned up [Kal98]. Later on, this material was recognized as the most northerly exposed

site of the Starčevo culture, thus having special historical significance for the Neolithization of the Central Danube [Kal98]. Due to the importance of the material, new excavations were started in order to gather as much scientific evidence as possible from this important site. The top soil was removed, and closed units from the prehistoric periods were opened by selective methods. This material has large information value, as it came from a controlled and dated context. The pottery fragments selected for analyses cover all prehistoric periods found during the recent excavation season, with an emphasis on early Neolithic pottery. In Table 2.1.7 the properties of the samples are listed. The firing atmosphere was concluded from the color of the specimens [Man88]. It can be seen that some developments were achieved in the control of firing temperature, since mainly the technique of oxygen reduction was observed from the Early Copper Age.

Table 2.1.7
Properties of the samples

Number	Unit	Culture	Age	Atmosphere
1	52 (western part)	Starčevo	Early Neolithic	Oxidizing
2	50	Starčevo	Early Neolithic	Mixed
3	54 (southern part)	Starčevo	Early Neolithic	Oxidizing
4	52 (grave soil)	Starčevo	Early Neolithic	Mixed
5	43	Lengyel	Early Copper Age	Reducing
6	53 (eastern part)	Kostolac	Late Copper Age	Reducing
7	48	Kisapostag	Early Bronze Age	Mixed
8	46	Kisapostag	Early Bronze Age	Reducing

Experimental

Three parts of the samples (original inner, outer surfaces and cut cross sections) were probed by the proton beam after cleaning them with pure alcohol in order to check the reliability of concentration values.

PIXE method described in subchapter 1.2 was employed to obtain information on the fragments. Approximately 10 mm^2 of each part of the samples were mapped by the proton beam in five steps using 2.5 mm^2 scan sizes to achieve an average and characteristic distribution of the inclusions. Spectra were taken first on the bulk and then on the inclusions using smaller scan sizes

corresponding to the specific situation. The scan areas used initially (2.5 mm x 1 mm) allowed to observe even 30-40 μm size objects, thus the typical enrichments with the smallest size of about 100 μm were easily explored. For the bulk measurements, the proton energy, collected charge, beam current and beam spot size were 2 MeV, 0.1 μC (2 μC with aluminum filter), 0.1 nA (0.5 nA with aluminum filter), 3 μm x 3 μm respectively. When measuring on the inclusions, the beam parameters were adjusted regarding to the composition of the sample.

Results and discussion

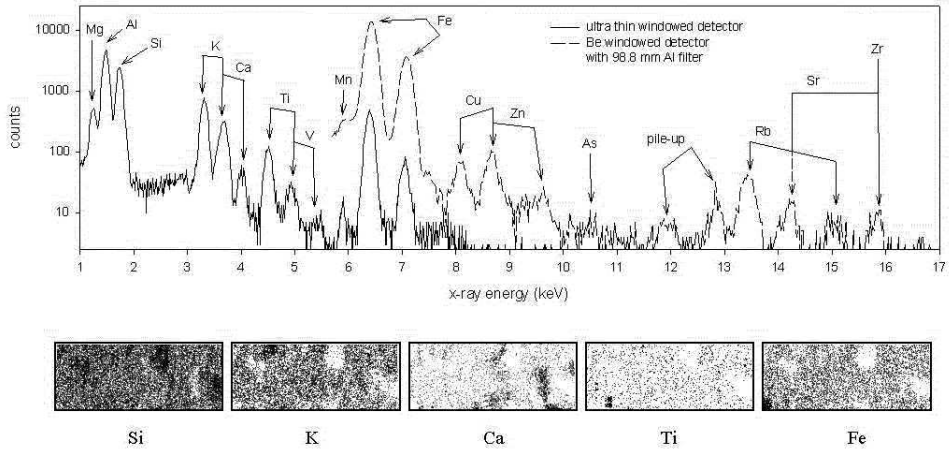

Figure 2.1.9 Typical spectrum taken on the bulk of a pottery sample and some elemental maps (produced by the low energy Si(Li) detector) indicating the characterizing enrichment places in the bulk material (scan size: 2.5 mm x 1 mm)

In Figure 2.1.9 typical spectra taken on the bulk of a pottery and some elemental maps indicating the characteristic enrichments can be seen. The major elements detected were Mg, Al, Si, K, Ca and Fe, while Ti, V, Mn, Cu, Zn, As, Rb, Sr and Zr appeared in the spectra as minor or trace constituents. Unfortunately no correlation was found between the distribution and/or size and/or number of enriched places and the age of the samples. Although, in addition to the abundant parts presented in Figure 2.1.9, Cu-rich places (originated from chalcopyrite) were found in all of the samples except the ones from the Early Neolithic. This may be an indication that from the Early Copper

Age, beside the common tempers, some other minerals were also used for producing potteries.

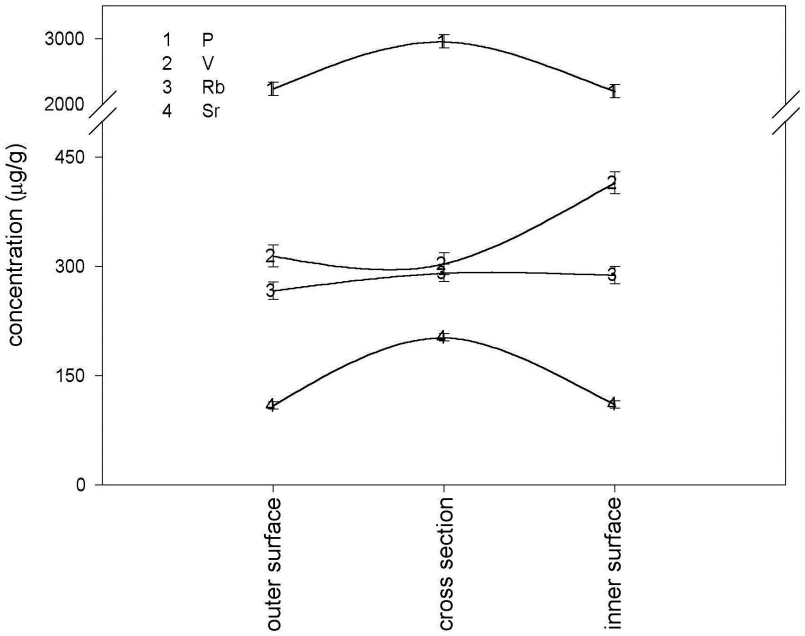

Figure 2.1.10 Variation of the concentration of some interesting elements from the outer to the inner surface of samples

The composition of the samples and the relation of the elemental concentrations to each other can vary during the firing, usage and because of the interaction between the material of the potteries and the soil in which they are buried. These factors are mixed, and their effects can not be unambiguously separated. This is illustrated in Figure 2.1.10 by the variations of the bulk concentration values of some elements used later for provenancing from the outer to the inner surfaces through the cross sections of the samples. Although only few elements are presented in this graph, the others also show this feature. (The largest concentration differences between the surfaces and the cross sections can be observed for P in samples #7 and #8. This reflects that they were used not only for storage, but for cooking [Sán98]). Because of this and the fact found and

mentioned earlier, namely, there is no unambiguous relation between the composition of mineral inclusions and age of the samples, the cross section of the specimens, which are almost not influenced by the above effects, was brought into focus. On the basis of this analysis, it was shown that using the concentration values of P, V, Rb and Sr (the selection of them is somehow accidental and the result of attempts according to the precedent in reference [Man88]), a classification can be given among the samples to a certain extent. The distribution of the pottery pieces in the 3-dimensional space chosen is plotted in Figure 2.1.11. As it is clearly seen, two distinct groups can be formed. The first one includes samples from the Starčevo and Kostolac cultures, while into the second cluster, the specimens from the Kisapostag and Lengyel cultures are fallen, which reflects the raw material differences rather than the production technique of the specimens. In this way, the initial assumption, i. e., the raw material of the potteries would be local, was disproved, which raises the possibility of trade with other populations or other clay source nearby.

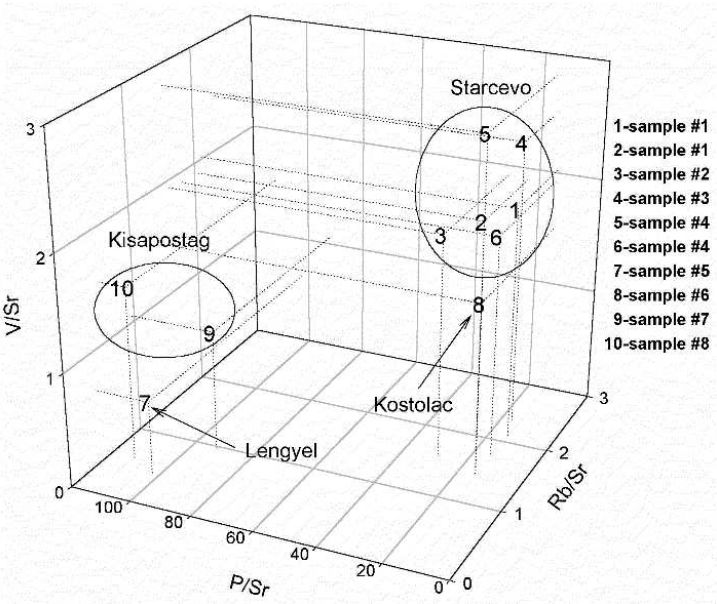

Figure 2.1.11 Distribution of the samples in a 3-dimensional space using P/Sr, V/Sr, Rb/Sr concentration ratios

2.2 GEOLOGY

2.2.1 STUDY ON PHENOCRYSTS IN OBSIDIAN GLASSES

Introduction

The study presented in subchapter 2.1.3 focused on the chemical composition of obsidians from different geographical localities. The samples were collected in order to investigate the glassy material from archeometrical and geochemical point of view. However, some of the specimens contained several phenocrysts[5] of relatively large size (10-500 μm). Silica-rich volcanic glasses, obsidians have a very low (sometime practically zero) content of phenocrysts. Therefore, the mineralogical identification of the characteristic phenocrysts when they are present and the knowledge of their minor and trace element contents can help to distinct among ancient obsidian sources. Moreover, phenocrysts may provide petrologic information as well.

This subchapter deals with the analysis of silicate, sulfide and sulfate minerals found in the obsidian samples from Tertiary or Quaternary volcanic area of Armenia, Greece, Hungary and Slovakia.

Description of the studied volcanic glasses

The localities, geological settings and age of the samples are listed in Table 2.2.1.

[5] Phenocyst is a microcrystal in the host glass. If it is incorporated from the surrounding rocks by the lava, it is called a xenocryst.

Table 2.2.1
The locality, geological setting and age of the analyzed obsidian samples

Sample number	Locality	Geological setting	Geological age
1	Aragats Mts., Armenia	subduction related volcanic arc	Pliocene-Quaternary
2	Giali, Greece	volcanic arc	Miocene-Quaternary
3	Melos, Greece	volcanic arc	Miocene-Quaternary
4	Erdõbénye, Tokaj Mts., Hungary	volcanic arc	Miocene
5	Sima, Tokaj Mts., Hungary	volcanic arc	Miocene
6	Viničky , Tokaj Mts., Slovakia	volcanic arc	Miocene

According to the so-called total alkali-silica (TAS) diagram [Mai89] each sample can be petrographically regarded as rhyolites (Figure 2.2.1). However, silicic obsidians can be classified chemically corresponding to their CaO, Al_2O_3 and Na_2O+K_2O contents [Mac92]. According to this ternary diagram, the samples show subalkaline peraluminous character (Figure 2.2.2).

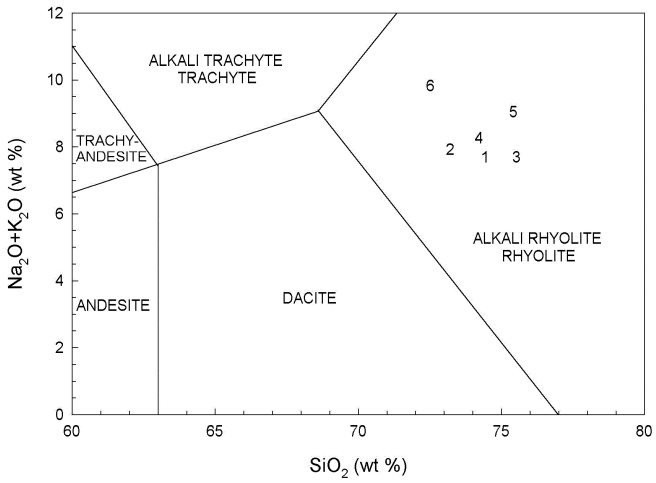

Figure 2.2.1 Localization of the studied obsidian samples in the total alcali-silica diagram

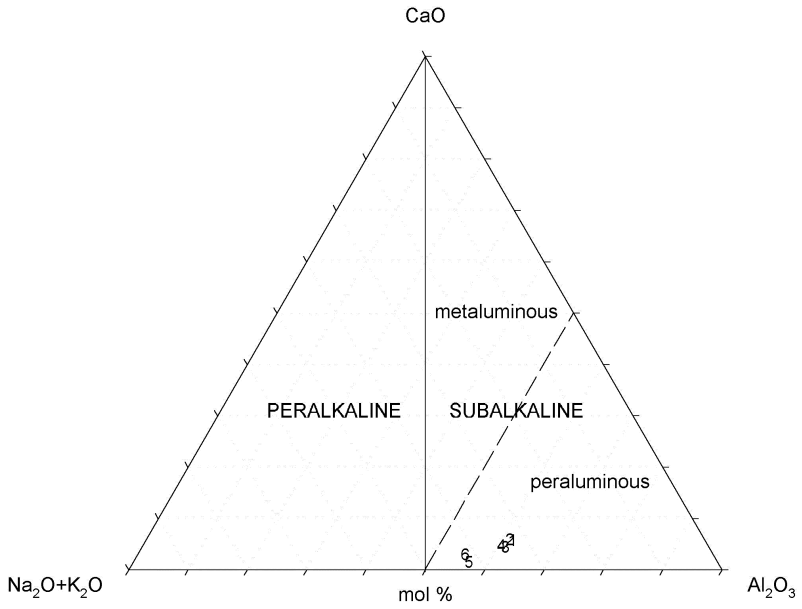

Figure 2.2.2 Localization of the studied obsidian samples in the CaO-Al_2O_3-(Na_2O+K_2O) diagram

Experimental

Thin sections of 40-50 μm were produced first and the minerals were identified by using a NIKON Microphot SA polarizing microscope.

Although the routine analysis of mineral phases is usually carried out by the electron microprobe technique, in this work the nuclear microprobe facility was used because additional information can be achieved with the detection of minor and trace elements (e.g., Y, Ag, Hf), which can be easily performed by this device. On the other hand, the latter instrument allowed to measure those trace elements in the host glass which are major or minor constituents of the minerals, thus giving the possibility of direct comparison of them.

The experimental conditions were the same as in subchapter 2.1.4, therefore they are not entirely recalled here. The proton beam of 2 MeV has an average projected range of about 50 μm in silicate materials which corresponds

to the size of the grains. The size of 2 x 2 μm^2 and intensity of 50 pA of the beam provided a non-destructive analysis. The integrated charge on the samples varied in a wider range (200-400 nC) according to the specific mineral studied. The scan size of the beam was also adjusted according to the size of the mineral assemblage in question. After the production of elemental maps, interesting and differing parts of the assemblages were selected and measured in order to identify the individual mineral phases. When small minerals (<40 μm) were investigated, interferences with the host material could be observed, therefore these spectra were not interpreted.

Results and discussion

The minerals measured in the obsidian glasses were zyrcon (6 pieces), pyroxene (4 pieces), amphibole (2 pieces), biotite (7 pieces), plagioclase feldspar (3 pieces), quartz (4 pieces), anhydrite (1 pieces), pyrite (2 pieces), chalcopyrite (2 pieces), pyrrhotite (1 pieces) with the occurrences of elements Na, Mg, Al, Si, P, S, Cl, K, Ca, Ti, V, Cr, Mn, Fe, Co, Ni, Cu, Zn, Rb, Sr, Y, Zr, Ag, Hf. In the following paragraphs, their description and related geological discussion is detailed.

Silicate minerals

a) Zircons

Zircon ($ZrSiO_4$) is a common accessory mineral in acidic volcanic rocks. It always contains some Hf, and continuous solid solution extends to hafnon ($HfSiO_4$).

Two crystals in obsidian from Sima (Hungary) and four crystals in obsidian from Viničky (Slovakia) were analyzed. The Hf/Zr atomic ratios of the measured zircon crystals were definitely lower for obsidian of Sima (0.009 and 0.010) than that of Viničky (0.012, 0.0.14, 0.015 and 0.018). The calculated wt% of Hf in zircons is 0.83 and 0.91 for Sima, and ranges from 1.10 to 1.68 for Viničky. These values are lower than the mean of 1.71 calculated by

Ahrens and Erlank, however they belong to the ranges of high frequency in the distribution diagram compiled by these authors [Car74]. The Hf/Zr atomic ratios of the host glasses are higher than those of the zircon crystals (0.033 for Sima and 0.027 for Viničky). It is worth mentioning that the differences between the Hf/Zr ratios of the zircon crystals and that of the host glass is much higher for Sima than for Viničky, which reflects the differences of the bulk contents of these sources mentioned in subchapter 2.1.3.

The yttrium content of the analyzed zircon crystals is also remarkable. The Y/Zr atomic ratios are 0.008 and 0.010 for Sima and range from 0.004 to 0.013 for Viničky . It seems that there is no definite correlation between Y/Zr and Hf/Zr ratios.

b) Pyroxenes

Pyroxenes are relatively rare, but not uncommon mineral constituents in acid volcanic rocks. They have a general formula $X_2Si_2O_6$ in which X is usually Mg, Fe, Ca rarely Mn, Li, Ti, Al or Na.

Pyroxene crystals were found in three samples coming from three different localities. According to the $CaSiO_3$-$MgSiO_3$-$FeSiO_3$ contents (Table 2.2.2), pyroxenes of obsidians from Melos (Greece) are augite, and those from Giali (Greece) are diopside-hedenbergite, while the pyroxene crystal found in obsidian from Sima (Hungary) is ferrosilite [Mor88]. Position of Ca-rich pyroxene from Melos and that of Ca-poor pyroxene from Sima more or less corresponds to the crystallization trend of Ca-rich and Ca-poor pyroxenes suggested by Carmichael [Car60], however the crystal from Giali lies far away from the trends.

Table 2.2.2
Estimated composition of the pyroxene crystals (at%) and the $\frac{(Fe+Mn)x\,100}{Fe+Mn+Mg}$ ratios for these crystals and their residual glasses

	$CaSiO_3$	$MgSiO_3$	$FeSiO_3$	$\frac{(Fe+Mn)x\,100}{Fe+Mn+Mg}$
Mp [a]	40.2	48.7	11.1	19.8
Mr	-	-	-	72.4
Gp1	47.0	25.0	28.0	37.5
Gp2	46.6	27.0	26.4	37.0
Gr	-	-	-	82.4
Sp	3.5	24.6	71.9	74.5
Sr	-	-	-	93.5

[a] Mp = pyroxene from obsidian Melos (Greece); Mr = residual glass-Melos;
Gp1, Gp2 = pyroxenes from obsidian Giali (Greece); Gr = residual glass-Giali;
Sp = pyroxene from obsidian Sima (Hungary); Sr = residual glass-Sima

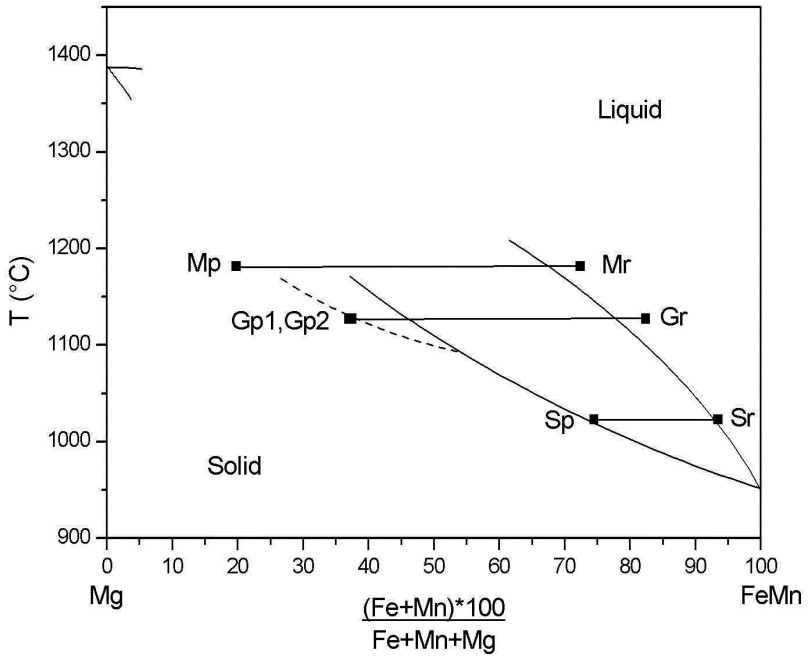

Figure 2.2.3 Possible relationship between pyroxenes and their residual glasses with respect to their relative iron enrichment

Pyroxene phenocrysts may be in equilibrium with residual glass, or they may be xenocrysts which have been incorporated in the glass. Figure 2.2.3 shows a possible relationship between pyroxenes and their residual glasses, in which

hypothetical solidus and liquidus curves were constructed by Carmichael on the basis of analytical data on Ca-rich pyroxenes and their residual glasses from some British and Icelandic Tertiary pitchstone [Bow13]. The pyroxene–glass pairs Mp–Mr and Gp1/Gp2–Gr lie off the hypothetical curves, therefore these pyroxene crystals could be regarded as xenocrysts. However, Carmichael suggests that a "rather odd-shaped bulge" of the solidus curve can also be assumed [Bow13]; in that case Mp-Mr and Gp1/Gp2–Gr pairs are not anomalous.

c) Amphiboles

Chemical composition of minerals of the amphibole group can be expressed with the formula $X_{0-3}Y_{5-7}Si_8O_{22}(OH)_2$ in which *X* can be Ca, Na, K, and *Y* can be Mg, Fe, Mn, Al, Ti. Silicon and (OH) can be partially replaced by Al and O or F respectively. Amphibole is common mineral constituent in igneous rocks, however it is relatively rare in obsidians.

Two amphibole (hornblende) crystals were found in the obsidian sample from Melos (Greece). It is quite difficult to give an exact composition because of the complicated structure of amphiboles and limits of the micro-PIXE method (OH^- content cannot be measured). According to the analyses, the most probable composition of these hornblende crystals is $NaCa_2Mg_{2-3}Fe_{1-2}Al_{0-1}[Si_{6-7}Al_{1-2}O_{22}(OH)_2]$.

d) Biotites

Biotite is the most common mafic mineral constituent in acid volcanic rocks. Its chemical composition can be expressed by the formula $K(Mg,Fe)_3[AlSi_3O_{10}(OH)_2]$.

Numerous biotite crystals were found in the studied samples, however most of them were small in size (<20 μm) and opacitized. Some unweathered biotite crystals in samples from Erdőbénye (Hungary) and Viničky (Slovakia) were analyzed.

Mg/Fe ratio of biotite crystals from Erdőbénye and Viničky ranged from 0.9 to 1.9 and from 0.6 to 0.9 respectively. Rubidium could be detected in each crystal (in the range of 0.1 at%), and the Rb/K ratio proved to be quite similar for the two localities (0.003 for Viničky and 0.002-0.004 for Erdőbénye). Rb_2O contents of the studied biotite crystals are also similar and show low variety: they ranges from 0.10 to 0.16 and from 0.11 to 0.12 for Erdőbénye and Viničky respectively.

e) Plagioclase feldspars

Plagioclase feldspars are formed by a continuous series of pure albite (Ab) ($NaAlSi_3O_8$) and anorthite (An) ($CaAl_2Si_2O_8$). Sodium-rich plagioclase is a common felsic mineral in acid igneous rocks. Accordingly, several plagioclase feldspar crystals of oligoclase composition ($Ab_{70\text{-}90}An_{10\text{-}30}$) were detected in obsidians from various localities. In some cases, however, calcium-rich plagioclases were also identified (Table 2.2.3). According to the micro-PIXE measurements, two plagioclase crystals in obsidian from Viničky (Slovakia) have bytownite ($Ab_{20}An_{80}$) and labradorite ($Ab_{45}An_{55}$) compositions, while one crystal in obsidian sample from Melos (Greece) showed bytownite-labradorite composition ($Ab_{30}An_{70}$).

Table 2.2.3
The albite-anorthite ratios for the Ca-rich plagioclase crystals and their residual glasses (wt%).

	albite	anorthite
Mf [a]	30	70
Mr	80 [b]	20 [b]
Vf1	20	80
Vf2	45	55
Vr	86 [b]	14 [b]

[a] Mf = feldspar from obsidian Melos (Greece); Mr = residual glass-Melos;
Vf1, Vf2 = feldspars from obsidian Viničky (Slovakia); Vr = residual glass-Viničky;
Sf = feldspar from obsidian Sima (Hungary); Sr = residual glass-Sima
[b] calculated from the normative Ab and An contents

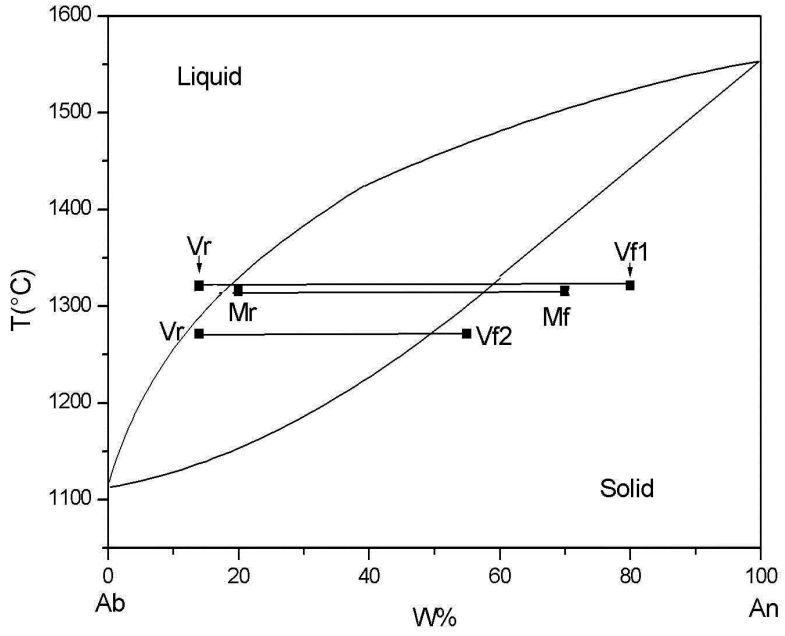

Figure 2.2.4 Possible relationship between Ca-rich plagioclases and their residual glasses. The system albite–anorthite at 1 bar pressure was made after Bowen [Bow13] and revised by Kushiro [Kus73]

Following Carmichael's train of thoughts related to pyroxenes found in acid glasses, possible relationship between Ca-rich feldspars and their residual glasses can be outlined. Figure 2.2.4 shows Ab/An ratios for the feldspar-residual glass pairs in the binary system Ab-An. The ratios for the residual glasses based on normative Ab and An values calculated from their major elemental compositions. As it can be seen, feldspar members of the pairs (particularly points Mf, Vf1) lie far from the solidus curve, indicating that they are not in equilibrium with their residual glasses. This pattern suggests that Mf, Vf1 are probably, and Vf2 possibly xenocrysts incorporated by the acid melts.

f) Quartz

Quartz is essential mineral constituent in acid igneous rocks, however, quite rare in obsidians. Obsidian from Giali (Greece) contains several angular

quartz crystals the size of which is some hundred μm. Some of these crystals are scattered in the glass, but others, sometime together with large sodic plagioclase, are embedded in rounded opaque material. These rounded objects can be regarded as inclusions, while the individual quartz crystals are xenocrysts. Probably, these quartz crystals were incorporated by the obsidian magma just before or during the volcanic activity because they do not show resorption embayments.

Non-silicate minerals

Two samples contained very interesting non-silicate mineral assemblages. One *anhydrite* ($CaSO_4$) crystal was found in obsidian from the Aragats Mountain (Armenia). The anhydrite crystal contains scattered fine grains of *chalcopyrite* ($CuFeS_2$) and is surrounded by secondary copper mineral (Figure 2.2.5). The latter mineral could not be identified unambiguously, nevertheless its emerging Ag content (0.06 at%) confirm that it differs from the inner chalcopyrite. Although anhydrite is primarily sedimentary mineral, it can be also formed by hydrothermal activity or volcanic exhalation. Appearance of copper ore minerals in and around the crystal suggests hydrothermal origin.

A rounded opaque grain was found in an obsidian from Viničky (Slovakia) which proved to be a mineral assemblage of *pyrrhotite* (FeS), *pyrite* (FeS_2) and subordinately *chalcopyrite* (Figure 2.2.6). The Fe/S ratio of 8/9 of the pyrrhotite was deduced from the measurements which showed chalcopyrite-pyrrhotite composition because it could not be originated by using the spectrum taken on the pyrrhotite-pyrite assemblage, since the pyrrhotite/pyrite ratio is ambiguous. The presence of pyrite and the low (0.1 at%) Ni content suggest a hydrothermal origin for this ore mineral assemblage. Pyrrhotite has not been observed in obsidians from Viničky so far [Ďud].

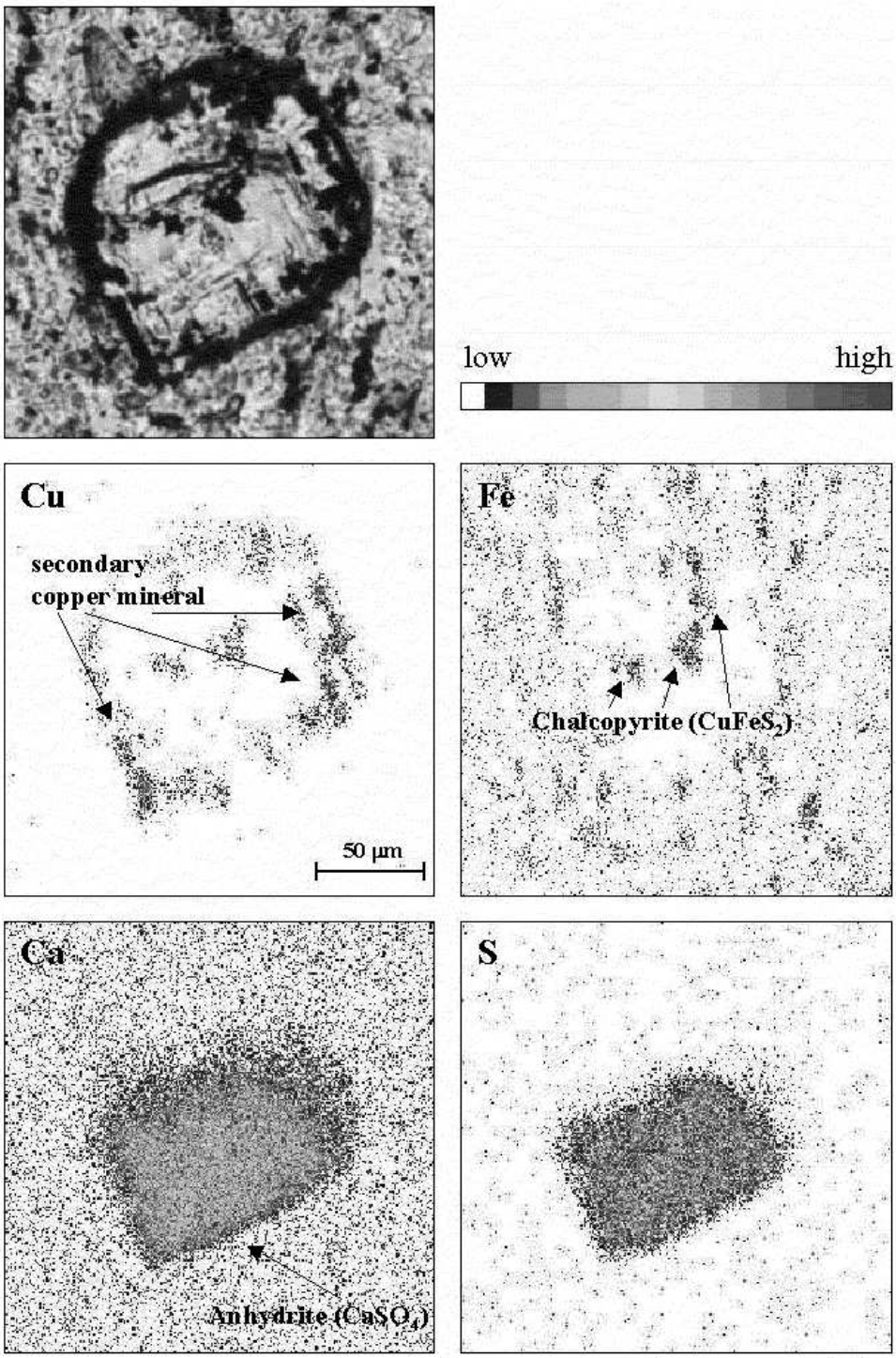

Figure 2.2.5 The photograph and some characteristic PIXE elemental maps of the anhydrite and associated crystals

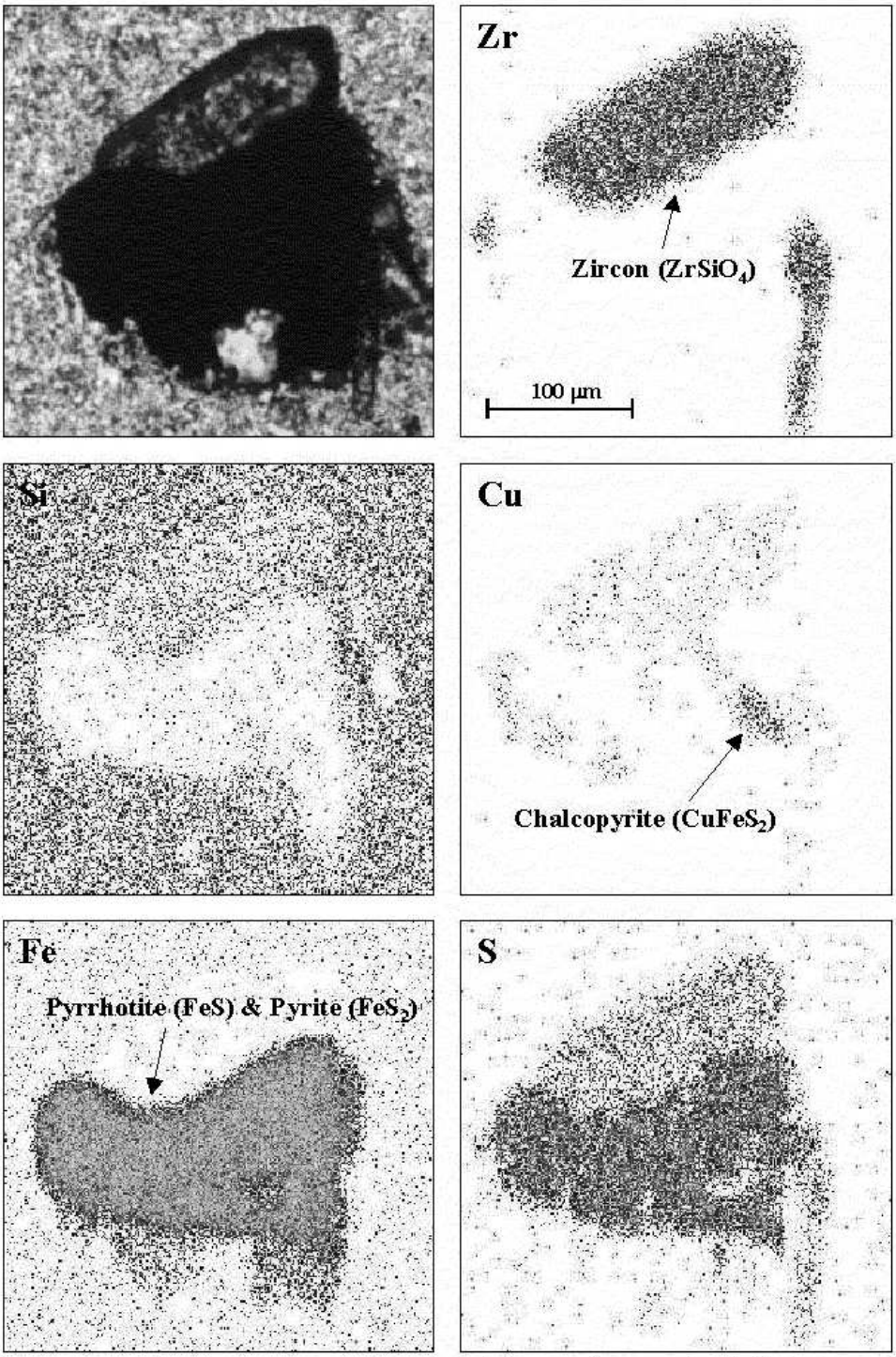

Figure 2.2.6 The photograph and some characteristic PIXE elemental maps of the mineral assemblage of zircon, pyrrhotite, pyrite and chalcopyrite

Finally, it must be noted that obsidian glasses from the above mentioned localities do not show trace of hydrothermal alteration. Therefore it is also possible that these hydrothermal minerals were incorporated before the solidification. The clarification of this question requires further studies.

2.2.2 INVESTIGATION OF MAGNETIC SPHERULES

Introduction

For the first time, Nordenskjold (1874) and later Murray (1876) reported on "magnetic spherules" the origin of which was interpreted as "cosmic" [Nor74, Mur76]. The systematic exploration and investigation of these objects started by the oceanographic expeditions Albatros, Galathea and Challenger [Pet50, Bru55].

In the past hundred years, magnetic spherules were found in various geological environments, namely, in the Antarctic and Greenland ice and glacial sediments [Koe89, Zbi94], in deep-sea floor cores [Kur94, Yad96], in meteorite fall areas [Nin54, Shy93], in Paleozoic-Mesozoic [Mio93, Det98], Mesozoic-Cenozoic [Loz81, Cza83] and Quaternary [Bi93, Mar67, Bor95] sediments, in volcanic [Fil81, Rob96] and granitoid-metamorphic [Jer78, Jak89] rocks. Magnetic spherules collected in recent sediments and oceanic floor around the industrial centers may also be the products of air pollution (perhaps over 99 %) [Puf80].

The origin of the magnetic spherules has not been entirely determined, although it has been restricted to extraterrestrial (cosmic dust or meteoritic impact), igneous (volcanic or metamorphic) and industrial processes. Examples for each genetic type of magnetic spherules above from Holocene fluvial deposits of the Carpathian Basin can be found in [Raj96a, Szö95]:

(1) impactites (extraterrestrial)
    (a) magnetite spherules formed by the melting of meteoritic matter or from condensed metal vapor,
    (b) metallic-silicate (and glassy) spherules formed by the mixing of the terrestrial matter by shock metamorphism,
(2) globules of the volcanogene hydrothermal effect (igneous),
(3) iron-welding produced spheres (industrial).

The aim of this study is to contribute to the identification of the magnetic spherules found in the Carpathian Basin and to prove the hypothesis that the investigated objects are the products of a meteoritic impact.

Description of spherules

The studied objects were collected from borehole cores in the Üveghuta area (Mórágy Granite Complex), SW-Hungary [Kók97]. Moissanite, shock metamorphic quartz, large number of magnetic spherules, metallic-silicate spherules, magnetite platelets and ejected slag fragments have been identified in the detritus red clay overlaying the surface of the above mentioned Lower Carboniferous Mórágy Complex [Bal83]. This paragenesis supposing a meteoritic impact event may not be identified either in the underlying granite or the overlying Quaternary loess and fossil soil. Only the magnetic spherules of the paragenesis is investigated here. The spherules indicated as Uh-s, Uh-i and Uh-ps (corresponding to the surface, inner part and polished section of the spherules respectively) in Table 2.2.4 are characterized by uniform morphologic and structural features as well as very high iron content. The texture of the samples has been studied by a scanning electron microprobe (SEM) using an AMRAY 1830I equipment. In Figures 2.2.7 and 2.2.8 peculiarities of a meteoritic impact can be observed: cup-like shape of a spherule, a broken spherule and special texture in its outer crust.

Table 2.2.4
The properties of the compared magnetic spherules

Symbol	Geological setting	Locality	Size (μm)	Investigated area
Uh-s	Pleistocene detritus, overlaying bed of Paleozoic Mórágy Granite	Borehole Üveghuta-5, depth: 54.6-54.8 m, SW-Hungary	100-200	surface
Uh-i	Pleistocene detritus, overlaying bed of Paleozoic Mórágy Granite	Borehole Üveghuta-5, depth: 54.6-54.8 m, SW-Hungary	100-200	inner part
Uh-ps	Pleistocene detritus, overlaying bed of Paleozoic Mórágy Granite	Borehole Üveghuta-5, depth: 54.6-54.8 m, SW-Hungary	100-200	inner part

Table 2.2.4 (Continued)

Symbol	Geological setting	Locality	Size (μm)	Investigated area
R-1	Recent river bed	Körös River, SE-Hungary	200-600	surface
R-2	Holocene sand of alluvial flat	Danube River, NW-Hungary	100-400	surface
Hn	Mesozoic Gemeric Granite	Hnilec, Slovakia	90-120	surface
Bükk	Paleozoic-Mesozoic bedded limestone	Gerennavár, Bükk Mts., NE-Hungary	3-20	surface
Jap	Paleozoic-Mesozoic bedded chert	SW-Japan	5-20	surface
DS	Recent deep-sea sediment	Hawaiian Islands	70-230	inner part

Literature for the different samples: R-2 [Raj96a]; Hn [Jak89]; Bükk [Det98]; Jap [Mio93]; DS [Yad96]

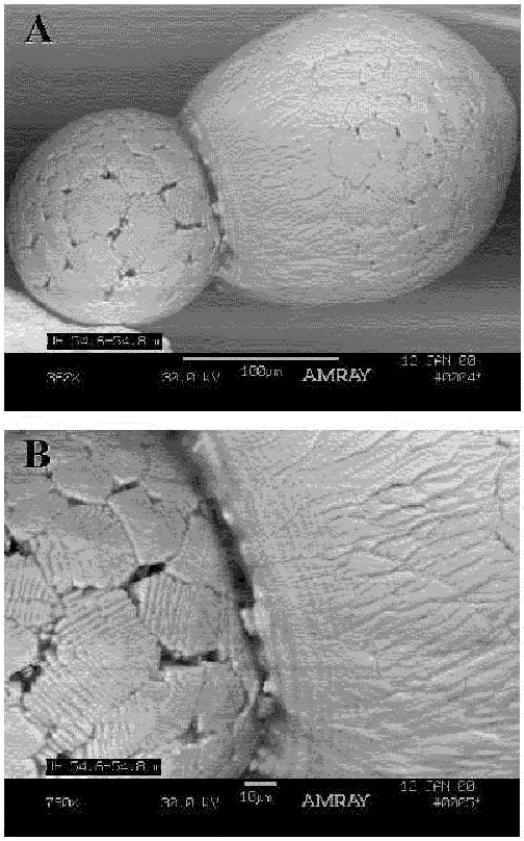

Figure 2.2.7 (A) SEM patterns for the magnetic spherules in borehole Üveghuta-5 showing ball-like and cup-like forms with typical cooling structures, (B) Microtexture of the polygonally and ”astrakhan-coated” surface indicative of meteoritic impact

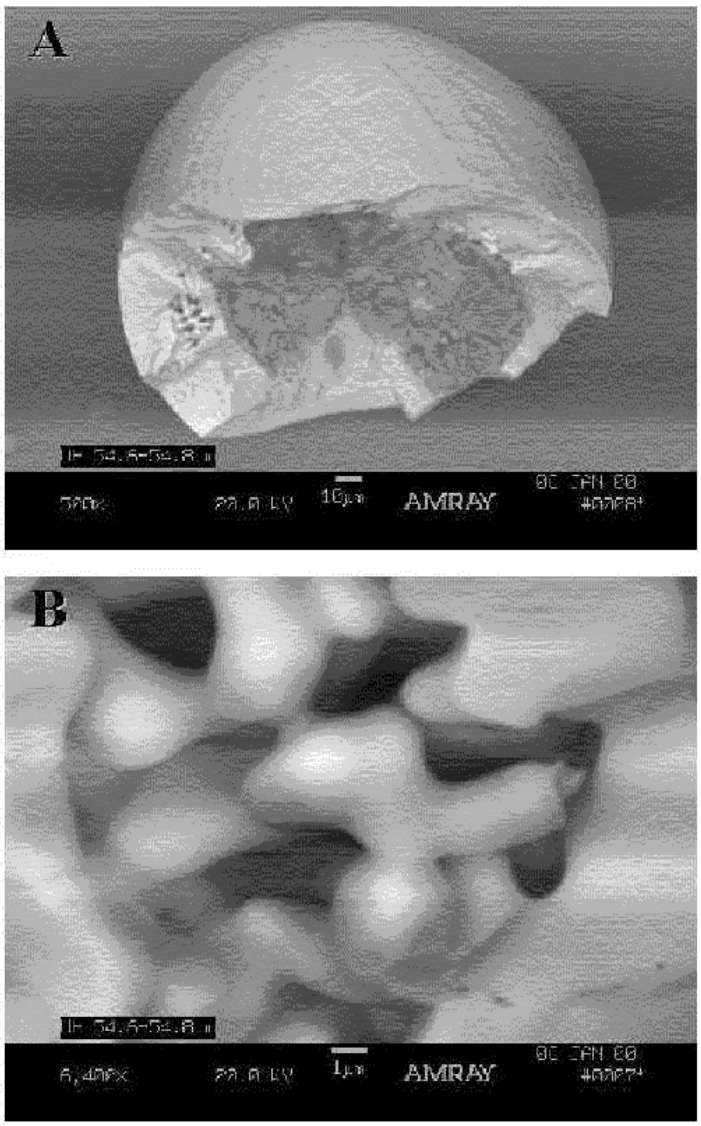

Figure 2.2.8 (A) SEM pattern for a cracked up magnetic spherule with streaked smooth surface in borehole Üveghuta-5, (B) Microtexture of the fluidal, dendroidal hollow inside indicative of rapid cooling from liquid state

For comparison, the data on the following groups of spherules are taken from the literature (summarized in Table 2.2.4):

(1) magnetic spherules showing similar morphological-structural and compositional features to the above ones, which were collected from alluvial Hungarian river beds (R-1 and R-2); according to earlier

studies [Raj96a], these spherules were regarded as objects coming from an impact event,

(2) magnetic spherules described by Detre et al. (Bükk) [Det98]; regarding the size, structure, composition and genesis of these spherules, this group differ from that of the spherules mentioned above; the authors state that these objects, which were collected from a formation of Permian-Triassic boundary, are cosmic/interstellar spherules as "messengers of a nearby supernova explosion",

(3) objects found in Japan (Jap) [Mio93] which correspond to the above (2) type spherules,

(4) magnetic spherules (Hn) [Jak89] identified in the Mesozoic Gemeric Granite Complex [Kov66],

(5) objects with cosmic origin from recent deep sea sediments (DS).

Additionally, I refer to data on spherules with different Fe-phases (magnetite, hematite, pure Fe) [Isa00] in order to compare them with the Üveghuta objects. Polished sections of magnetic spherules from the carbon-bearing Barringer crater, Arizona [Sut85, Sho87] were also analyzed collating them to the Üveghuta spherules regarding their carbon contents.

Experimental

Several (19 sample) spherules showing the special texture mentioned earlier and presented in Figures 2.2.7 and 2.2.8 were selected for elemental analysis. The specimens were analyzed in original (Uh-s), broken (Uh-i) and polished section (Uh-ps) forms because it was found that magnetic spherules may have a silicate-metallic rim around the metallic core. (As an example Fe and Al maps taken by micro-PIXE method on spherules from the Barringer crater (Arizona, USA) can be seen in Figure 2.2.9.)

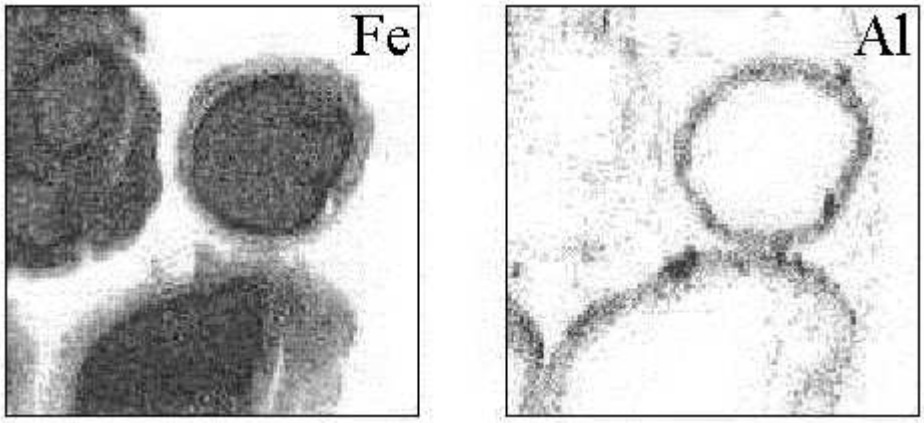

Figure 2.2.9 Fe and Al maps taken by micro-PIXE method on polished thin sections of Arizona spherules (scan size: 1000 μm x 1000 μm, white color: low counts, blue: high counts)

The elements above Na were detected by micro-PIXE technique using 2 MeV proton beam focused to 2 μm x 2μm size with a beam current of 50 pA. The integrated charge deposited on the samples was typically 150-200 nC. The beam was scanned over the sample up to a maximum area of 1000 μm x 1000 μm. It is known that due to the spherical shape of the spherules, the calculation of the concentration values without the application of geometrical corrections may cause high systematic errors. However, as it was discussed in a previous work [Uzo98], this can be avoided by measuring on the center of the samples where the surface can be approximated with a plane.

The C and O contents of the spherules were determined by DIGE method bombarding the samples by 1.8 MeV deuterons and using the Clover-Ge-BGO detector system placed at 55° with respect to the beam direction. The collected charge on the target was 3μC, while the beam spot size, scanned area and beam current were 100 μm^2, 1 mm^2 and 1 nA respectively. The concentration values were deduced by means of some samples (H14 Hungarian steel, Mylar, Kapton) used as standards with well-known carbon and oxygen contents.

Results and discussion

From the evaluation of the measured PIXE spectra, the major constituent of the spherules was iron. As minor elements, Al, Si, P (few wt%), S, K, Ca, Ti, V, Cr, Mn and Ni were detected. The DIGE analysis revealed that the samples have relatively high carbon contents and contain significant amount of oxygen (20-40 wt%) as well. The collected charges were adjusted so that the determination of trace elemental concentrations was not possible because the minor metallic elements were enough to achieve our aims.

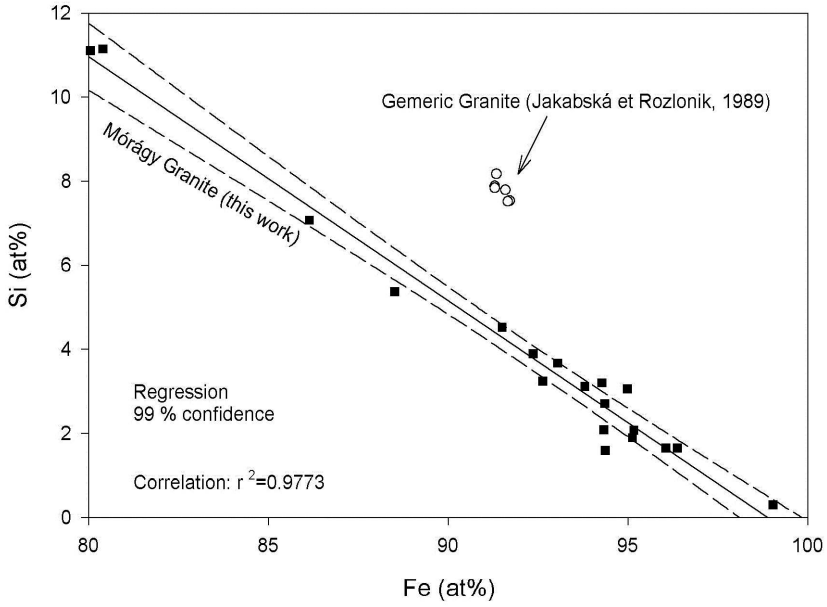

Figure 2.2.10 Bivariate plot of Fe and Si of the magnetic spherules (■ Mórágy Granite, ○ Gemeric Granite)

The studied spherules from the weathered surface of the Mórágy Granite Complex are probably ferrosilicium material similar to the spherules in the samples from the Gemeric Granite Complex [Jak89], however the Fe/Si ratio shows a negative correlation scattered in a wider range (Figure 2.2.10). Ferrosilicium with formula Fe_2Si contains 79.91 % Fe and 20.09 % Si [Jak89].

The data show that our spherules contain 95-99 %[6] Fe for the inner part and 80-97 % Fe for the surface. This composition indicates a rapid cooling (e.g., in water) of a melt at a temperature of >1200 ^{o}C [Jak89] and suggests an impact event.

Identification and distinction of terrestrial (volcanic, antropogene) and extraterrestrial spherules can be made by using some elemental ratios (Ti/Fe, Cr/Fe, Mn/Fe, Co/Fe, Ni/Fe) [Yad96, Mio93].

By averaging the elemental concentrations of the samples in the different groups and comparing our results with data from the literature (Table 2.2.5), correlations of some elemental ratios have been made (Figure 2.2.11).

Table 2.2.5
Average ratios with standard deviations of some metallic elements for the different groups of samples (n. d = not determined, values are multiplied by 1000)

Sample	Number of samples	Ti/Fe av. (st. d.)	Cr/Fe av. (st. d.)	Mn/Fe av. (st. d.)	Ni/Fe av. (st. d.)
Uh-s	16	0.55 (0.66)	1.17 (0.68)	6.56 (0.51)	n. d.
Uh-i	3	n. d.	0.95 (0.86)	2.92 (0.95)	2.01 (0.60)
R-1	5	1.63 (0.20)	0.70 (0.56)	12.3 (0.58)	0.85 (0.35)
R-2	4	1.73 (0.08)	1.05 (0.58)	10.76 (0.46)	0.93 (0.29)
Hn [a]	6	n. d.	2.46 (0.73)	4.61 (0.89)	n. d.
Bükk	3	0.62 (0.69)	1.68 (0.66)	3.53 (0.62)	21.5 (0.92)
Jap [b]	5	1.63 (0.46)	2.24 (0.62)	5.56 (0.59)	16.9 (0.10)
DS [c]	4	n. d.	0.51 (0.29)	n. d.	35.5 (0.16)

[a] data taken from reference [Jak89]
[b] data taken from reference [Mio93]
[c] data taken from reference [Yad96]

[6] The oxygen content of the spherules was not determined by micro-PIXE, therefore the composition without this element was rounded up to 100 %.

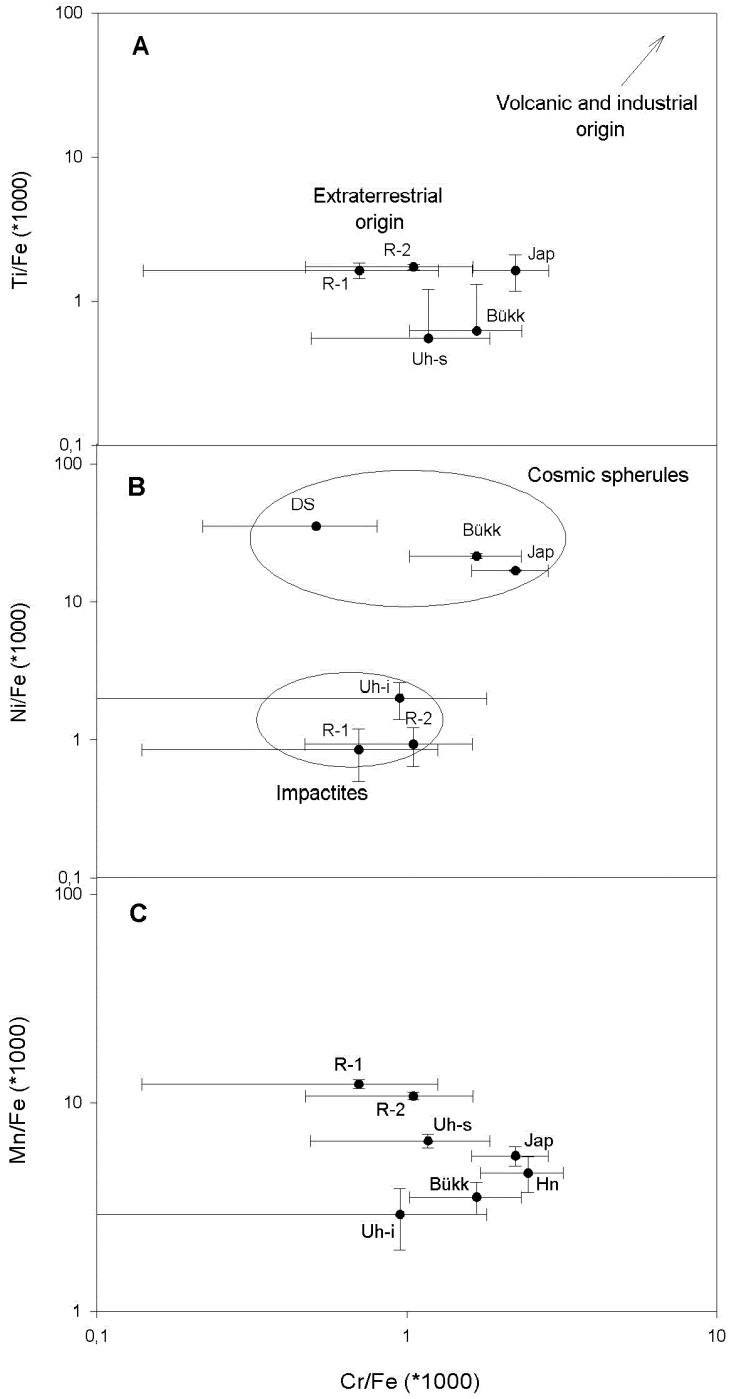

Figure 2.2.11 Averages of (Mn/Fe), (Ni/Fe), (Ti/Fe) vs. (Cr/Fe) for different groups of magnetic spherules (for legend see Table 2.2.4)

On the basis of these diagrams, the following conclusions can be drawn.

- In general, Ti content of volcanogene and industrial magnetic spherules is higher than that of the extraterrestrial ones [Mio93, Puf80]. According to the Ti/Fe vs. Cr/Fe diagram (Figure 2.2.11/A), all of the studied samples are of extraterrestrial origin.
- It is widely accepted that Ni content of magnetic spherules indicates extraterrestrial origin, although opposite views are also known [Puf80, Gor67]. The so-called fission crust, which can be found on the surface of micrometeorites and impactite spherules, does not commonly contain Ni. This fact is also confirmed by the analytical data of the samples from Üveghuta area (Uh-s, Uh-i). On the basis of the Ni/Fe vs. Cr/Fe diagram (Figure 2.2.11/B), the impactite and cosmic[7] spherules can be definitely separated from each other.
- Position of the samples in the Mn/Fe vs. Cr/Fe diagram (Figure 2.2.11/C) suggests that in the case of impactite magnetic spherules, it is crucial which part of the samples were analyzed. Outer surfaces of the samples from Üveghuta area (Uh-s) are characterized by definitely higher Mn content than their inner parts (Uh-i). Using this diagram, the two genetic groups can be separated from each other by the analysis of the outer crust. Position of magnetic spherules of Gemeric Granite Complex (Hn) in the Mn/Fe vs. Cr/Fe diagram is similar to that of the samples from the Bükk Mountain (Hungary) and Japan. At the same time, however, it is questionable that the origin of the (Hn) spherules are cosmic, since Ni has not been detected in them. Probably, only the surfaces of the spherules were analyzed, and composition of their inner part can be

[7] Cosmic spherules are often called micrometeorites

considerably different, as it is shown by the samples from the Üveghuta area.

In Figures 2.2.12 and 2.2.13 Fe, Al, C and O (from DIGE measurements) maps are presented for Arizona and Üveghuta samples, while Table 2.2.6 includes the average concentration values for different sampling points.

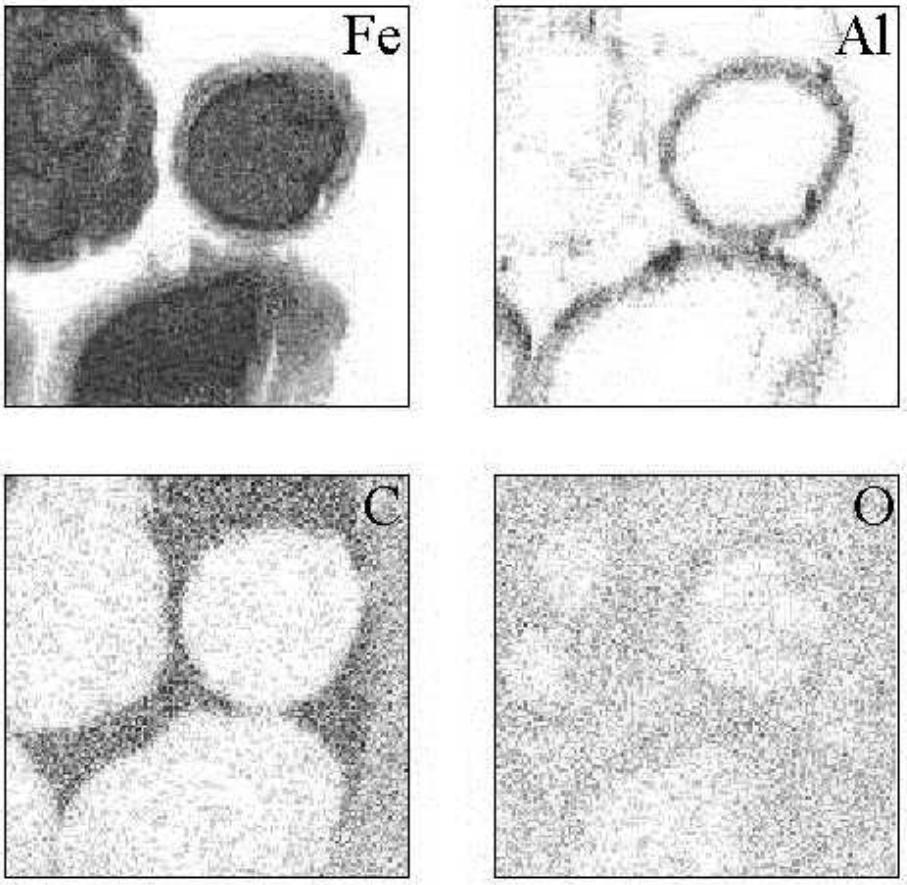

Figure 2.2.12 Fe, Al, C and O (from DIGE measurements) maps taken on Arizona metallic spherules (scan size: 1000 x 1000 μm^2)

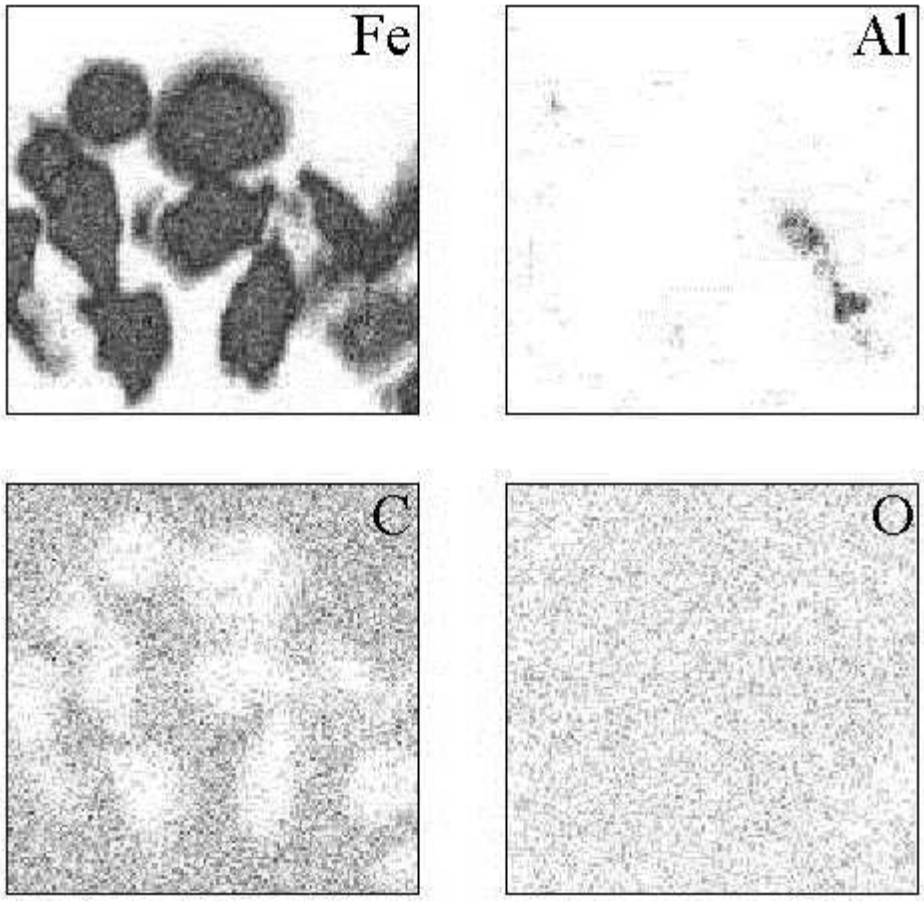

Figure 2.2.13 Fe, Al (from PIXE measurements), C and O maps taken on Üveghuta metallic spherules and platelets (scan size: 1000 x 1000 μm^2)

Table 2.2.6
Average carbon and oxygen contents of the spherules and the meteorite fragment at different sampling points

Sampling point	C (μg/g)	O (μg/g)
Arizona inner core (9 points)	1700±140	875±70
Arizona outer rim (8 points)	12600±1900	398000±60000
Üveghuta inner core (10 points)	3540±210	310000±52000

It is clearly seen that the Arizona objects have fine-grained siliceous impactite coating around their metallic cores, which fact is well-known [Mea65], however the Üveghuta samples do not clearly show this feature. The correlation between the Fe and O contents of the samples (Figure 2.2.14) is also plotted in order to

determine the Fe-phases of spherules comparing them with earlier identified magnetite, hematite and pure Fe spherules [Isa00]. On the basis of this graph, two of the Üveghuta spherules can be classified as magnetites, five of them can be regarded as hematites, while the rest two samples are more oxidized. The Fe-Ni-metal, kamacite cores of the Arizona specimens have oxygen contents only at trace element level, while the outer rims contain significant amount of oxygen (30-60 wt%). This oxygen (and Fe) enrichment of impactite coating suggests the possibility that mineral phase could be goethite or maghenite [Mea65].

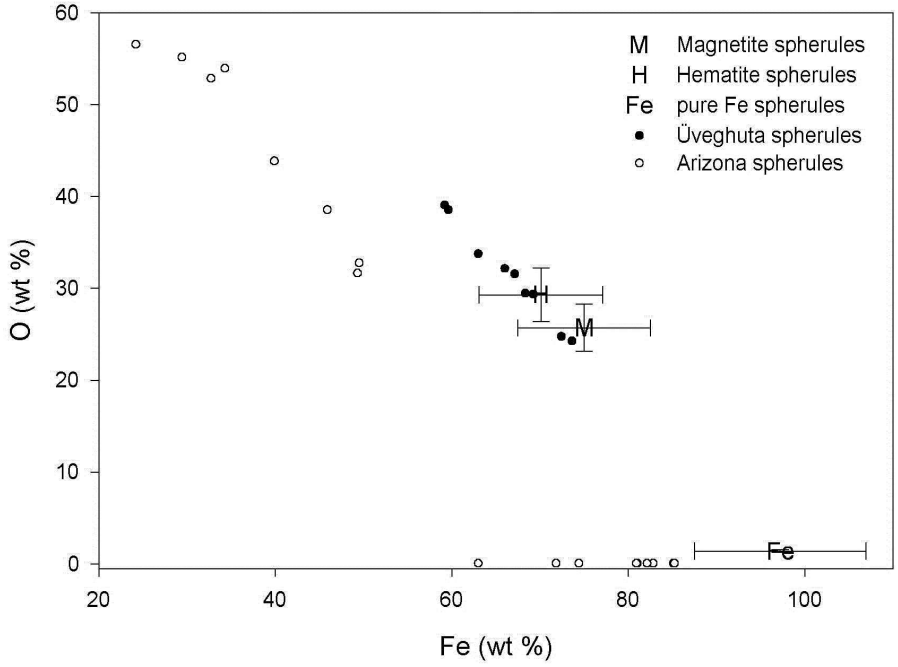

Figure 2.2.14 Correlation between Fe and O content of the metallic spherules (the data on magnetite, hematite and pure Fe spherules are taken from [Isa00])

Carbon content of rim and plain specimens of the Canyon Diablo meteorite was systematically measured earlier [Moo67]. However, other impact objects (spherules, blebs, slag) have not been studied in this respect. The carbon content of the Arizona objects may be connected to various accessory

phases such as graphite, diamond, lonsdaleite [Fro67], carbide [Axo77], cohenite [Hun94] and moissanite [Sco71, Yud70], however this study can not answer this question. It was proven only that the carbon contents of the spherule outer coating are much higher than that of the inner core, and the meteorite fragment has the highest concentrations. It is worth mentioning that the carbon content of the Üveghuta iron-oxide spherules is quite similar to that of the Fe-Ni rich core of the metallic spherules from the Barringer Crater, Arizona. These connections are discussed as it follows:

- Data support the argument [Kar96, Miu95] that the impact shock heating and decarbonation of the target rocks caused partial oxidation and chemical fractionation of meteorite projectile of the Barringer Crater, Arizona.
- It is an important result that the presence of carbon is also characteristic for the Üveghuta spherules representing a higher oxidized iron-oxide type. This fact prompts further studies on samples from other boreholes (e.g., [Isa00, Mar97]) to trace possible carbon-bearing phases. These results, however, are not sufficient to decide whether the carbon content of the Üveghuta spherules indicates the presence of ‘carbon-bearing’ or a ‘carbon-free’ impact crater, i.e., the carbon may come from the target rock or from the projectile.

SUMMARY

In this work interdisciplinary studies on geology, archeology and physics based on ion beam techniques were shown. The thesis was started with a short introduction to the concepts and principles of the applied methods and instruments, which was continued by the description of methodological developments. Then several applications of ion beam techniques in the field of geology and archeology were detailed.

The relevant results I achieved during this interdisciplinary scientific research at the nuclear microprobe facility of ATOMKI can be summarized in the following items.

1. It is the first time that a Clover-Ge-BGO detector system was successfully applied in ion beam analysis at the nuclear microprobe facility. The problem, how to produce elemental maps, was solved by using analogous summation, while good energy resolution spectra could also be created. The total photopeak efficiency of this type of detector systems was measured for the first time because it was crucial in cross section calculations, and the achieved minimum detection limits in PIGE measurements for most of the detectable elements reached the best values found in recent papers, sometimes they are better than the published ones. Utilizing the excellent characteristics of the set-up, the detection of lithium (an interesting tracer element) in obsidian glasses by PIGE method was made possible, and carbon concentration could be measured in spherule samples with minimum detection limit commensurable to that of charged particle detection.
2. By studying deuteron induced reactions on different light elements, typical gamma-ray spectra were presented and tables summarizing the most suitable gamma-ray lines for elemental analysis of a given element were constructed.

The thick-target yields for the most characteristic gamma-rays of elements with Z=3-20 (except Be, Ne, P and Ar) in the deuteron energy range of 0.7-3.4 MeV were also completed with additional yield curves. It was found that the measured yields could be generally fitted by a rather simple three-parameter function:

$$Y=Y_0\cdot(E_d-E_{d0})^a$$

where Y is the absolute gamma-ray yield, E_d is the deuteron energy; Y_0, E_{d0} and a are the fitting parameters. The thick target yield investigations were contributed to differential cross-section measurements on carbon target material and discussed from the point of view of elemental analysis. In conclusion, it can be advised that for thick targets 1.8 MeV deuteron energy should be used. On the other hand, for thin targets, the highest yield can be achieved at 1.792 MeV, therefore this should be the recommended energy. The resonance at 1.45 MeV ($\Gamma_{c.m.}\approx$7 keV) can be easily used for carbon depth profiling if a thin (10-150 nm) surface layer is to be analyzed on a thick substrate (1 keV energy step means approximately 4 nm). By measuring geological and standard samples, the accuracy and the MDLs for the carbon and oxygen determination was tested. It was pointed out that the concentration values can be calculated with an uncertainty of 10 %, while the MDLs are 90 and 70 μg/g for C and O respectively iron matrix.

3. It was shown that the combined application of PIXE and PIGE methods is capable of characterizing engraved gems and to provide useful information on the originality and production technique of the artifacts. The 18th century Wedgwood products could be easily separated from the other samples, while the composition of two of the nicolo imitations was found similar to that of the authentic Roman gem. It was also concluded that the remaining samples were made from sodium glass. Nevertheless, their glass-pastes are different from that of the original Roman glass.
4. For the first time, the systematic elemental analysis of radiolarites in large numbers was carried out by ion beam analysis. It can be regarded as a

pioneering work which provide primary knowledge on the distribution of concentration values measured in samples with different geographical locations. The samples which were not radiolarites could be distinguished by means of their potassium, rubidium and iron contents. It was pointed out that from the huge concentration data set, only some trace elements (Ni, Cu, Zn) seem to characterize the provenance of the samples. As a result of the cluster analysis, the samples from the Vienna-basin can be separated unambiguously into one cluster with a special type (namely Tata-type) of Transdanubian radiolarite. Specimens from the Bakony-region and the Mecsek radiolarites could be grouped together in another cluster. Gerecse-type Transdanubian, Carpathian radiolarites and the Greek samples fell into two clusters mixed. No correlation was found between the measured concentration data and the color of the samples as well as the type numbers of the pieces based on macroscopical grouping.

5. The obsidian analysis revealed the fact that PIXE and PIGE methods are capable to make distinctions among Carpathian sources. By measuring the composition of many samples with different localities (Mexico, Iceland, Turkey, Armenia, Italy, Greece, Slovakia and Hungary), a proper database was created in ATOMKI. In this way, the classification of obsidian samples with unknown provenance became possible. The investigation on the archeological site Bodrogkeresztúr-Henye showed that the archeological specimens are local and mesolocal. In other words, the people at this site exploited the sources of the area and did not use obsidian materials or tools of distant provenances.
6. As a result of prehistoric pottery investigation, it was proven that potteries may contain significant amount and various type of temper materials which, however, do not unambiguously characterize the ages. Nevertheless, it was pointed out that the specimens of Early Neolithic do not include Cu-rich places (originated from chalcopyrite), which is an indication of the behavior that in the Early Neolithic Age chalcopyrite was not used as temper material.

It was also shown that the firing process, usage and interaction of the soil with the material of the clays can alter the concentration of elements. To a certain extent, a classification could be performed among the samples where clusterization reflects the raw material differences rather than the production technique of the specimens. The initial assumption, i. e., the raw material of the potteries would be all local, cannot be maintained, which raises the possibility of trade with other populations or the use of different clay sources nearby.

7. On the basis of the study on phenocrysts observed in obsidian glasses, the following petrologic conclusions could be drawn:
   - Hf contents of zircon crystals in obsidian samples from two close localities of the Tokaj Mts. (Sima in Hungary and Viničky in Slovakia) show definite differences, which reflects the distinction between the bulk composition of their host glasses.
   - The Ca-poor orthopyroxene crystal in the sample from Sima (Hungary) is in equilibrium, while Ca-rich pyroxene crystals of obsidians from Melos and Giali (Greece) may be in equilibrium with the residual glass. Therefore, it is possible that these crystals can not be regarded as xenocrysts.
   - The Ca-rich plagioclase feldspars detected in samples from Viničky (Slovakia) and Melos (Greece), while quartz crystals in the specimen from Giali (Greece) have probably been incorporated in the glass.
   - Anhydrite-chalcopyrite and pyrrhotite-pyrite-chalcopyrite assemblages in obsidians from Aragats Mountain (Armenia) and Viničky (Slovakia) were formed by hydrothermal activity. However, it is questionable whether the solid obsidian rocks suffered the hydrothermal activity or these crystals were incorporated by the rhyolitic melts.
8. By measuring magnetic spherules from Mecsek Mts., it was pointed out that their materials are similar to ferrosilicium. On the basis of some elemental ratios and the classification of Fe-phases, it can be stated that the objects are

extraterrestrial and show the possibility of meteoritic origin. In this way, the initial assumption of the geologists was confirmed, i.e., the fingerprint of a possible meteoritic impact in the past could be revealed.

ÖSSZEFOGLALÁS (SUMMARY IN HUNGARIAN)

A doktori dolgozatban ionnyaláb analitikai módszerekkel, a geológia, a régészet és a fizika határterületén végzett kutatásokat ismertettem. A disszertációt a felhasznált eljárások és berendezések alapjainak és elveinek leírásával kezdtem, amit az általam végrehajtott metodikai fejlesztések bemutatása követett. Ezután geológiai és régészeti alkalmazásokat tárgyaltam.

Az ATOMKI pásztázó nukleáris mikroszondájának segítségével elért új tudományos eredményeimet a következő pontokban lehet összefoglalni:

1. Elsőként alkalmaztam az úgynevezett Clover-Ge-BGO detektorrendszert ionnyaláb analitikai célokra nukleáris mikroszondánál. Az elemtérképek készítését analóg összegzéssel oldottam meg. Először mértem meg ilyen típusú detektorrendszer teljes fotocsúcs hatásfokát. Az elért PIGE detektálási határok elérik a korábban publikált legjobbakat, néha azoknál jobbak is. A detektorrendszer alkalmazásával, PIGE módszerrel is lehetővé vált a lítium detektálása obszidián mintákban, a szén detektálási határát vas mátrixban pedig összemérhetővé sikerült tenni azzal, amit töltött részecske detektálással lehet elérni.
2. A különböző könnyű elemeken történő deuteronindukált reakciók vizsgálata során bemutattam a tipikus gamma-spektrumokat, az analitikai célokra leginkább felhasználható gamma-vonalakat pedig táblázatokban tettem közzé. A korábban megjelent vastag céltárgyakra vonatkozó hozamokat újabbakkal egészítettem ki. A hozamgörbéket pedig egy viszonylag egyszerű függvény segítségével tudtam megilleszteni:

$$Y=Y_0\cdot(E_d-E_{d0})^a$$

ahol Y az abszolút gamma-hozam, E_d a deuteron energia; Y_0, E_{d0} és a illesztési paraméterek. A vastag céltárgy hozamvizsgálatokat vékony szén

céltárgyon végzett gerjesztési függvény mérésekkel egészítettem ki. Ezen mérések alapján vastag céltárgyak széntartalmának meghatározására 1.8 MeV bombázóenergiát javasoltam, vékony céltárgyakra pedig 1,792 MeV-t. Az 1,45 MeV ($\Gamma_{c.m.}\approx 7$ keV) energiánál található rezonanciát szén mélységanalízis elvégzésére alkalmasnak találtam, amennyiben egy vékony (10-150 nm) felületi réteget kell vizsgálni vastag hordozón (1 keV energialépés 4 nm-t jelent). Geológiai és standard minták mérésével a módszer pontosságát és az elérhető detektálási határokat tanulmányoztam szénre és oxigénre. Kimutattam, hogy a koncentrációértékek 10 % pontossággal meghatározhatók, a detektálási határok pedig szénre és oxigénre rendre 90 és 70 μg/g.

3. Megmutattam, hogy a PIXE és PIGE módszerek együttes alkalmazásával kielégítően jellemezhető metszett gyűrűkövek összetétele és hasznos információt nyújtanak az eredetüket és elkészítési technikájukat illetően. A 18. századi Wedgwood termékeket egyszerűen el tudtam különíteni a többitől, két nicolo másolat összetételét pedig az eredeti római korú mintáéhoz hasonlónak találtam. Szintén kimutattam, hogy a többi gyűrűkő nátronüvegből készült, azonban alapanyaguk eltér az eredeti római korú üvegétől.
4. Elsőként mértem meg radiolaritok elemi összetételét ionnyaláb módszerek felhasználásával, amit úttörő munkának lehet tekinteni a területen, hisz először szolgáltatott információt a különböző lelőhellyel rendelkező minták elemi koncentrációinak eloszlása terén. A más anyagból készült kőeszközöket sikerült elválasztanom a radiolaritoktól a K, Rb és Fe tartalmuk alapján. Kimutattam, hogy a meghatározott elemek közül csak néhány nyomelem (Ni, Cu, Zn) alkalmas a lelőhely jellemzésére. Klaszteranalízis eredményeként a bécsi mintákat egyértelműen el tudtam választani a többitől a Tata-típusú dunántúli radioalarittal együtt. A bakonyi és mecseki mintákat egy csoportba soroltam. A Gerecse-típusú dunántúli, a kárpáti és a görög radiolaritok vegyesen kerültek két csoportba. Sem a minták színe, sem pedig

a makroszkópos azonosításból származó csoportjai nem mutattak összefüggést az elemi összetétellel.

5. Az obszidiánokon végzett vizsgálataim kimutatták, hogy a PIXE és PIGE módszerekkel különbséget lehet tenni a kárpáti források között. Változatos lelőhelyű (Mexikó, Izland, Törökország, Örményország, Olaszország, Görögország, Szlovákia és Magyarország) obszidiánok összetételének mérésével megfelelő adatbázist hoztam létre az ATOMKI-ban, amelynek segítségével lehetővé vált az ismeretlen forrással rendelkező minták besorolása. A Bodrogkeresztúr-Henye régészeti lelőhely kombinált kőeszköz vizsgálata során bebizonyítottam, hogy a régészeti minták lokálisak illetve mezolokálisak és nem utalnak távolabbi területekkel való kereskedelemre. Más szavakkal, megerősítettem azt a régészeti feltételezést, hogy az itt élő őskori emberek a környezetükben található forrásokat aknázták ki.
6. Őskori agyagedények vizsgálatának eredményeként számos soványító anyagot mutattam ki a mintákban, amelyek azonban nem jellemezték a korukat egyértelműen. Azonban a korai neolitikumi edényekben kalkopiritet nem találtam soványító anyagként, míg az összes többiben igen. Azt is sikerült kimutatni, hogy az égetési eljárás, a használat vagy a talajba kerülés után az azzal történő kölcsönhatás során az elemek koncentrációja megváltozik. Bizonyos mértékig tudtam osztályozni a mintákat, habár ez a csoportosítás az alapanyag különbségeket jellemzi, nem pedig az elkészítési technikát. Ezáltal az eredeti régészeti, hogy a lelőhelyen talált edények anyaga helybéli és azonos forrásból származik, megcáfolható, ami felveti a kereskedelmi kapcsolatok lehetőségét más csoportokkal, vagy egy másik nyersanyagforrás létét.
7. Az obszidián mintákban található mikrokristályok tanulmányozása során a következő ásványtani következtetéseket lehetett tenni:
    - A Tokaj-Eperjes hegység két forrásából (Sima és Szőllőske, Szlovákia) származó obszidiánban található cirkon kristályok Hf

tartalma eltér egymástól, ami visszatükrözi az üveg alapanyagaiknál talált különbséget.

- A simai mintában talált Ca-szegény ortopiroxén kristály biztosan, a meloszi és giali obszidiánokban lévők pedig valószínűleg egyensúlyban vannak az őket tartalmazó üveggel. Ezért ezeket a kristályokat nem tekinthetjük xenokristályoknak.
- A Szőllőskéről származó és a meloszi mintákban talált Ca-gazdag földpátok, míg a giali mintában lévő kvarc kristályok az üvegalapanyagból kristályosodtak ki.
- Az örmény és szlovákiai mintákban talált anhidrit-kalkopirit és pirhotin-pirit-kalkopirit ásványtársulások valószínűleg hidrotermális aktivitás során jöttek létre. Azonban nem dönthető el, hogy maguk a kristályok vagy az őket tartalmazó obszidián üvegek szenvedték-e el ezt a hatást.

8. A Mecsek hegységből származó mágneses szferulák mérésével kimutattam, hogy azok anyaga hasonlít a ferroszilíciuméhoz. Néhány elem koncentrációjának aránya és az Fe-fázisok azonosítása alapján kijelenthető volt, hogy a szferulák földönkívüliek és meteoritikus eredetre utalnak. Ezáltal megerősítettem az eredeti geológiai feltételezést, azaz egy - a régmúltban történt - lehetséges meteoritbecsapódásra utaló nyomokat fedeztem fel.

REFERENCES

[Ajz] F. Ajzenberg-Selove, Nucl. Phys. A460 (1986) 1, A475 (1987) 1, A490 (1988) 1, A506 (1990) 1, A523 (1991) 1.

[Ams67] G. Amsel, D. Samuel, Anal. Chem. 39 (1967) 1689.

[Ant82] J. Antoni, Our prehistoric ancestors in Csabdi, Régészeti kutatások a Dunántúlon. Exhibition Guide (1982) 1.

[Ant90] J. Antoni, PhD.Thesis (1990).

[Ard78] E. Ardaens, Thesis 3e qcle (1978).

[Axo77] H. J. Axon, W. R. D. Couper, J. Kinder, Nature 267 (1977) 414.

[Bác89] E. Bácskay, Communicationes Archaeologicae Hungaricae (1989) 5.

[Bal88] M. Balla, J. Bérczi, G. Keömley, Gy. Rosner, D. Gabler, ARH Archaeometrical Research in Hungary, Budapest National Centre of Museums (1988) 103.

[Bal83] K. Balogh, E. Árváné Sós, Gy. Buda, Anu. Inst. Geol. Geofiz. 61 (1983) 359.

[Bár79] K. J. Bárta, Slovenska Archaeologia 27 (1979) 5.

[Bar00] L. Bartha, I. Uzonyi, Nucl. Inst. Meth. B161-163 (2000) 339.

[Bel99] L. Bellot-Gurlet, T. Calligaro, O. Dorighel, J.-C. Dran, G. Poupeau, J. Salomon, Nucl. Instr. and Meth. B.150 (1999) 616.

[Bi93] D. Bi, R. D. Norton, K. Wang, Geochim. Cosmochim. Acta 57 (1993) 4129.

[Bir78] J. R. Bird, L. H. Russell, W. R. Ambrose, M. D. Scott, Analytical Chemistry, 50 (1978) 2082.

[Bir85] J. R. Bird, J. S. Williams (Eds.), “Ion Beams for Materials Analysis”, Academic Press, Australia, 1989.

[Bir91] K. T. Biró, J. Regenye, Acta Archaeologica Hungarica 43 (1991) 337.

[Bir91a] K. T. Biró, V. Dobosi, LITOTHECA - The Comparative Raw Material Collection of the Hungarian National Museum. Catalogue. (1991) 1-268.

[Bir98] K. T. Biró, Hung. Nat. Mus. (1998) 1.

[Bir98a] K. T. Biró, Journal of Anthropological Archaeology 17 (1998) 1.

[Bor85] I. Borbély-Kiss, E. Koltay, S. László, Gy. Szabó and L. Zolnay, Nucl. Inst. and Meth. B12 (1985) 496.

[Bor94] I. Borbély-Kiss, Zs. Fülöp, T. Gesztelyi, Á. Z. Kiss, E. Koltay, Gy. Szabó, Nucl. Inst. Meth. B85 (1994) 836.

[Bor95] I. Borbély-Kiss, I. Rajta, I. Beszeda, Gy. Szöőr, Proc. NIPR. Symp. Antarct. Meteorites, Japan (1995) 16.

[Bow13] N. L. Bowen, Amer. J. Sci. 4 (1913) 577.

[Bru55] A. E. Bruun, E. Langer, H. Pauli, Deep-sea Res. 2 (1955) 230.

[Car60] I. S. E. Carmichael, J. Petrology 1 (1960) 309.

[Car74] I. S. E. Carmichael, F. J. Turner, J. Verhoogen, Igneous petrology, McGraw-Hill, New York (1974) 739 pp.

[Che81] J. R. Chen, H. Kneis, B. Martin, R. Nobiling, D. Pelte, B. Povh, K. Traxel, Nucl. Inst. Meth. 181 (1981) 141.

[Cou91] P. Courel, P. Trocellier, M. Mosbah, N. Toulhoat, J. Gosset, P. Massiot, D. Piccot, Nucl. Inst. Meth. B54 (1991) 429.

[Cza83] I. Czajkowski, P. Engelert, A. Bosselini, J. G. Ogg, Meteoritics 18 (1983) 286.

[Dec78] G. Deconninck, “Introduction to Radioanalytical Physics”, Akadémiai Kiadó, Budapest, 1978.

[Det98] Cs. M. Detre, I. Tóth, A. Gucsik, A. Z. Kiss, I. Uzonyi, Sz. Bérczi, Proc. 29th Lunar and Planetary Sci. Conf., Houston, 1998.

[Dob00] V. Dobosi, Prehistória (in press)

[Dol98] G. Dollinger, C. M. Frey, A. Bergmaier, T. Faestermann, Nucl. Inst. Meth. B136/138 (1998) 603.

[Dom60] J. Dombay, Archaeologia Hungarica 37 (1960) 1.

[Duc99] G. Duchêne, F. A. Beck, P. J. Twin, G. de France, D. Curien, L. Han, C. W. Beausang, M. A. Bentley, P. J. Nolan, J. Simpson, Nucl. Inst. Meth. A432 (1999) 90.

[Ďud] Rudolf Ďuďa, Eastern Slovak Museum, Košice, private communication

[Ele97] Z. Elekes, The Journal of Undergraduate Research in Physics, 16 (1997) 7.

[Ele99] Z. Elekes, Á.Z. Kiss, Gy. Gyürky, E. Somorjai, I. Uzonyi, Nucl. Instr. Meth. B158 (1999) 209.

[Ele00] Z. Elekes, Á. Z. Kiss, I. Biron, T. Calligaro, J. Salomon, Nucl. Inst. Meth. B168 (2000) 305.

[Fil81] L. G. Filimonová, Dokl. Akad. Nauk. 262 (1981) 962.

[Fro67] C. Frondel, U. B. Marvin, Nature 214 (1967) 587.

[Gea74] N. L. Gearhart, H. J. Hausmann, J. F. Morgan, G. A. Norton, N. Tsoupas, Phys. Rev. C10 (1974) 1739.

[Ghe99] K. Gherdán, Gy. Szakmány, T. Weiszburg, G. Ilon, Berichte der Deutschen Mineralogischen Gesellschaft 1 (1999) 82.

[Gih86] D. Gihwala, M. Peisach, J. Radioanal. Chem. Letters 106 (1986) 9.

[Gor67] A. El Gorsey, H. Fechtic, Smithsonian Contr. Astrophys. 11 (1967) 391.

[Gra99] B. Gratuze, J. Arch. Sci. 26 (1999) 869.

[Gri94] G. W. Grime, M. Dawson, Nucl. Inst. Meth. B89 (1994) 223.

[Gro97] D. Gronenborn, Universitätsforschungen zur Prähistorischen Archäologie 37 (1997) 1.

[Hun94] Huntington (1894) in H. M. Nininger, Report of progress. Yr. Bk. Am. Phi. Soc. 1948 (1949) 582.

[Isa00] Y. W. Isachsen in C. M. Detre (Ed.), Terrestrial and Cosmic Spherules, Acad Press, Budapest (2000) 72.

[Ish87] K. Ishii, M. Valladon, J. L. Debrun, Nucl. Inst. Meth. 150 (1987) 213.

[Jak89] K. Jakabská, L. Rozložník, Geologicky Zborník – Geologica Carpathica 40 (1989) 305.

[Jän79] Fr. Jännicke, Grundriss der Keramik. II. Stuttgart (1879) 653 skk.; European Ceramic Art from the End of the Middle Ages to about 1815. 660 skk, s. v. Wedgwood, Josiah.

[Jer78] P. V. Jermolov, V. N. Koroljuk, Dokl. Akad. Nauk. 240 (1978) 155.

[Joh88] S. A. E. Johansson, J. L. Campbell, "PIXE: A Novel Technique for Elemental Analysis", John Wiley & sons Ltd., Great Britain, 1988.

[Kal77] N. Kalicz, J. Makkay, StudArch Studia Archaeologica 7 (1977) 1.

[Kal98] N. Kalicz, Zs. M. Virág, K. T. Biró, Documenta Praehistorica 25 (1998) 151.

[Kar96] J. S. Kargel, P. Coffin, M. Kraft, J. S. Lewis, C. Moore, D. Roddy, E. M. Shoemaker, J. H. Wittke, Lun. Plan. Sci. XXVII (1996) 645.

[Ken80] M. J. Kenny, J. R. Bird, E. Clayton, Nucl. Instr. Meth. 168 (1980) 115.

[Kil88] V. Kilikoglou, Y. Maniatis, P. Grimanis, Archaeometry 30 (1988) 37.

[Kis85] Á.Z. Kiss, E. Koltay, B. Nyakó, E. Somorjai, A. Anttila, J. Räisänen, J. Radioanal. Nucl. Chem. Articles 89 (1985) 123.

[Kis94] Á.Z. Kiss, I. Biron, T. Calligaro, J. Salomon, Nucl. Instr. Meth. B 85 (1994) 118.

[Koe89] C. Koeberl, E. H. Hagen, Geochim. Cosmochim. Acta 53 (1989) 937.

[Kók97] A. Kókai, Ann. Rep. of the Geol. Inst. of Hungary 1996/2 (1997) 59.

[Kov66] M. Kováčik, Slovak Geol. Mag. 3-4 (1966) 215.

[Kur94] G. Kurat, C. Koeberl, T. Presper, F. Brandstätter, M. Maurette, Geochim. Cosmochim. Acta 58 (1994) 3879.

[Kus73] I. Kushiro, Yb. Carnegie Instn. Wash. 72 (1973) 502.

[Lan00] W. A. Lanford, S. Bedell, S. Amadon, A. Haberl, W. Skala, B. Hjorvarsson, Nucl. Inst. Meth. B161/163 (2000) 202.

[Lec95] J. Lech (Ed.) Catalogue of flint mines, Archaeologia Polona 33 (1995) 1.

[Loz81] N. G. Lozoyay, Okeanologiya, Moskva, 21 (1981) 89.

[Mac92] R. Macdonald, R.L. Smith, J.E. Thomas, Chemistry of the subalkalic silicic obsidians, US Geol. Survey Professional Paper, 1523, Washington, 1992.

[Mai89] R.W. Le Maitre (ed), A Classification of Igneous Rocks and Glossary of Terms, Blackwell, Oxford, London, 1989.

[Man88] Y. Maniatis, V. Perdikatsis, K. Kotsakis, Archaeometry 30 (1988) 264.

[Mar97] F. Marini, J-G. Casier, J-M. Claude, J-M. Théry, Sphaerula 1 (1997) 4.

[Mar67] U. B. Marvin, N. T. Einaudi, Geochim. Cosmochim. Acta 31 (1967) 1871.

[Mea65] C. W. Mead, J. Litter, E. C. T. Chao, Am. Mineral. 50 (1965) 667.

[Mik94] Pannonia Regia. Művészet a Dunántúlon 1000-1541. Kunst und Architektur in Pannonien 1000-1541. Eds. Á. Mikó and I. Takács, Budapest (1994) 322.

[Mio93] S. Miono, Y. Nakayama, H. Shoji, H. Tsuji, A. Nakanishi, Nucl. Inst. Meth. B75 (1993) 435.

[Miu95] Y. Miura and M. Okamoto, Antarctic Meteorites, Tokyo 20 (1995) 169.

[Moo67] C. B. Moore, P.J. Birrell, C.F. Lewis, Geochim. Cosmochim. Acta 31 (1967) 1885.

[Mor88] N. Morimoto, J. Fabries, A. K. Ferguson, I. V. Ginzburg, M. Ross, F. A. Seifert, J. Zussman, K. Aoki, G. Gottardi, American Mineralogist 73 (1988) 1123.

[Mur76] J. Murray, Proc. Roy. Soc. 9 (1876) 258.

[Nin54] H. H. Nininger, Am. J. Sci. 252 (1954) 277.

[Nor74] A. E. Nordenskjold, Overs. Kgl. vet Akad. Fürh., Stockholm, (1874) 1.

[Ont00] M. Á. Ontalba Salamanca, J. L. Ruvacalba-Sil, L. Bucio, L. Manzanilla, J. Miranda, Nucl. Inst. Meth. B161-163 (2000) 762.

[Pet50] H. Pettersson, H. Rotschi, Nature 166 (1950) 308.

[Pie96] N. Piel, W.H. Schulte, M. Berheide, H.W. Becker, L. Borucki, C. Grama, M. Mehrhoff, C. Rolfs, Nucl. Instr. Meth. B118 (1996) 186.

[Puf80] J. H. Puffer, E. W. B. Russell, M. R. Rampino, J. Sedimentary Petrology 50 (1980) 247.

[Raj96] I. Rajta, I. Borbély-Kiss, Gy. Mórik, L. Bartha, E. Koltay, Á. Z. Kiss, Nucl. Inst. Meth. B109/110 (1996) 148.

[Raj96a] I. Rajta, I. Borbély-Kiss, Gy. Mórik, L. Bartha, E. Koltay, Á. Z. Kiss, Gy. Szöőr, Nucl. Inst. Meth. B118 (1996) 437.

[Rio95] S. Rio, N. Métrich, M. Mosbah, P. Massiot, Nucl. Inst. Meth. B100 (1995) 141.

[Rob96] E. Robin, N. H. M. Swinburne, L. Froget, R. Rocchia, J. Gayraud, Geochim. Cosmochim. Acta 60 (1996) 815.

[Rut70] E. Ruttkay, MAGW 100 (1970) 70.

[Rya93] C. G. Ryan, W. L. Griffin, Nucl. Inst. Meth. B77 (1993) 381.

[Sán98] A. Sánchez, M. L. Cañabate, R. Lizcano, Archaeometry 40 (1998) 341.

[Sav99] A. Savdou, X. Aslanoglou, T. Paradellis, M. Pilakouta, Nucl. Instr. Meth. Bl52 (1999) 12.

[Sco71] E. R. D. Scott, Nature 229 (1971) 61.

[Sep98] A. Seppälä, J. Räisänen, E. Rauhala, Z. Szőkefalvi-Nagy, Nucl. Instr. Meth. B143 (1998) 233.

[Sho87] E. M. Shoemaker, Geol. Soc. Am. Cent. Fileds Guide – Rocky Mountains Sect. (1987) 399.

[Shr99] C. Shriner, M. J. Dorais, Archaeometry 41 (1999) 25.

[Shy93] S. Shymanovich, T. Kolosova, A. Raukas, R. Tiirmaa, Proc. Estonian Acad. Sci. Geol. U2 (1993) 127.

[Sil00] B. Sillar, M. S. Tite, Archaeometry 42 (2000) 2.

[Sta] CSS: STATISTICA (1986-1991) User's Manual, StatSoft

[Sut85] S. R. Sutton, J. Geophys. Res. 90 (1985) 3690.

[Sza93] Gy. Szabó and I. Borbély-Kiss, Nucl. Inst. and Meth. B75 (1993) 123.

[Sza89] Gy. Szabó, L. Zolnai, Nucl. Inst. Meth. B36 (1989) 88.

[Szé85] G. Székely, Comp. Phys. Comm. 34 (1985) 423.

[Szö95] Gy. Szöőr, Gy. Gyuricza, I. Beszeda, P. Rózsa, Proc. Int. Meeting on Spherulites, KFKI Rep., Budapest (1995) 67.

[Tho95] O. Williams-Thorpe, Archaeometry 37, 2 (1995) 217.

[Tou91] N. Toulhoat, P. Trocellier, P. Massiot, J. Gosset, K. Trabelski, T. Rouaud, Nucl. Inst. Meth. B54 (1991) 312.

[Tou93] N. Toulhoat, P. Courel, P. Trocellier, J. Gosset, Nucl. Inst. Meth. B77 (1993) 436.

[Tro99] P. Trocellier, P. Berger, B. Berthier, E. Berthoumieux, J. P. Gallien, N. Metrich, C. Moreau, M. Mosbah, M. E. Varela, Nucl. Inst. Meth. B158 (1999) 221.

[Try73] S. Tryti, H. Holtebekk, J. Rekstad, Nucl. Phys. A201 (1973) 135.

[Uzo98] I. Uzonyi, Á. Z. Kiss, P. Solt, L. Dosztály, O. Kákay-Szabó, Cs. H. Detre, Nucl. Inst. Meth. B139 (1998) 192.

[Uzo01] I. Uzonyi, I. Rajta, L. Bartha, Á. Z. Kiss, A. Nagy, Nucl. Inst. Meth. B, in press

[Vér65] L. Vértes, Quartär 16 (1965) 79.

[Vic94] I. Vickridge, J. Tallon, M. Presland, Nucl. Instr. Meth. B85 (1994) 95.

[Wei99] G. Weisgerber (Ed.), 5000 Jahre Feuersteinbergbau, Bochum, Deutschen Bergbau-Museum (1999) 1.

[Yad96] T. Yada, T. Nakamura, M. Sekiya, N. Takaoka, Proc. NIPR. Symp. Antarct. Meteorites, Japan (1996) 218.

[Yud70] I. A. Yudin, Meteoritika 30 (1970) 93.

[Zbi94] M. Zbik, V. A. Gostin, Proc. NIPR. Symp. Antarct. Meteorites, Japan (1994) 169.

PUBLICATIONS RELATING THE PHD THESIS

1. I. Borbély-Kiss, T. Gesztelyi, Z. Elekes, I. Rajta, E. Koltay, Á. Z. Kiss, "Investigation of Classical Ring-Stones and their Imitations", Prc. 5th Int. Conf. on Nondestructive Testing (art '96), Sept. 24-26, 1996, Budapest, Hungary, pp. 131-142.
2. Z. Elekes, "Evaluation of Thick Target Yields of Deuteron Induced Gamma Ray Emission from Li, B, N, F, Na, Mg", The Journal of Undergraduate Research in Physics 16 (1997) 7.
3. Z. Elekes, Á. Z. Kiss, Gy. Gyürky, E. Somorjai, I. Uzonyi, "Application of a Clover-Ge-BGO System for PIGE Measurements at a Nuclear Microprobe", Nuclear Instruments and Methods B158 (1999) 209.
4. Z. Elekes, I. Uzonyi, B. Gratuze, P. Rózsa, Á. Z. Kiss, Gy. Szöőr, "Contribution of PIGE Technique to the Study of Obsidian Glasses", Nuclear Instruments and Methods B161-163 (2000) 839.
5. Z. Elekes, Á. Z. Kiss, I. Biron, T. Calligaro, J. Salomon, "Thick Target Gamma-Ray Yields for Light Elements Measured in the Deuteron Energy Interval of 0.7-3.4 MeV" Nuclear Instruments and Methods B168 (2000) 305.
6. Z. Elekes, K. T. Biró, I. Uzonyi, I. Rajta, Á. Z. Kiss, "Geochemical Analysis of Radiolarite Samples from the Carpathian Basin" Nuclear Instruments and Methods B170 (2000) 501.
7. P. Rózsa, Gy. Szöőr, B. Gratuze, Z. Elekes, I. Beszeda, J. Simulák, "Classification and Distinction of Obsidians by Various Analytical Techniques", Applied Mineralogy in Research, Economy, Technology, Ecology and Culture (Eds.: D. Rammlmair, J. Mederer, Th. Oberthür, R. B. Heimann, H. Pentinghaus), Rotterdam, A. A. Balkema (2000), ISBN 90 5809 163 5.

8. K. T. Biró, Z. Elekes, B. Gratuze, "Ion Beam Analyses of Artefacts from the Bodrogkersztúr-Henye Lithic Assemblage", Bodrogkeresztúr-Henye /NE-Hungary/ Upper Palaeolithic Site, Budapest, Printing House of the Hungarian National Museum (2000), ISBN: 963 9046 450
9. Gy. Szöőr, Z. Elekes, P. Rózsa, I. Uzonyi, J. Simulák, Á. Z. Kiss, "Magnetic Spherules: Cosmic Dust or Markers of a Meteoritic Impact ?", Nuclear Instruments and Methods B (in press)
10. Z. Elekes, K. T. Biró, I. Uzonyi, A. Simon, Á. Z. Kiss, "Analysis of Prehistoric Pottery Finds from the Balaton Region, Hungary", Nuclear Instruments and Methods B (in press)
11. Z. Elekes, Gy. Szöőr, Á. Z. Kiss, P. Rózsa, A. Simon, I. Uzonyi, J. Simulák, “Carbon and Oxygen Determination in Magnetic Spherules by Deuteron Induced Gamma-Ray Emission Method at a Nuclear Microprobe”, Nuclear Instruments and Methods B (submitted)
12. P. Rózsa, Z. Elekes, Gy. Szöőr, I. Uzonyi, J. Simulák, A. Simon, Á. Z. Kiss, "Study on Phenocrysts in Obsidian Glasses", Nuclear Instruments and Methods B (submitted)

OTHER PUBLICATIONS

1. J. Dombóvári, L. Papp, I. Uzonyi, I. Borbély-Kiss, Z. Elekes, Zs. Varga, J. Mátyus, Gy. Kakuk, "Study of Cross-Sectional and Longitudinal Distribution of Some Major and Minor Elements in the Hair Samples of Haemodialysed Patients with Micro-PIXE Method", Journal of Analytical Atomic Spectrometry 14 (1999) 553.
2. Á. Z. Kiss, A. Simon, D. L. Beke, G. A. Langer, L. Daróczi, Z. Elekes, F. Ditrói, S. Mészáros, "IAEA Co-ordinated Research Programme: Application of MeV Ion Beams for Development and Characterization of Semiconductor Materials (G4.02: Utilization of Particle Accelerators)", Progress Report. Project No.: HUN 10032/R1., Sept. 14, 1999
3. B. Gratuze, I. Uzonyi, Z. Elekes, Á. Z. Kiss, E. Mester, "A Study of Hungarian Medieval Glass Composition", EUR 19218 Ion Beam Study of Art and Archaeological Objects – A Contribution by members of the COST G1 Action (Eds.: G. Demortier, A. Adriaens), Luxembourg: Office for Official Publications of the European Communities (2000), ISBN 92-828-7652-7.
4. B. Gratuze, I. Uzonyi, Z. Elekes, Á. Z. Kiss, E. Mester, "A Study of Hungarian Medieval Glass Composition (preliminary results)", British Archaeological Reports [Archaeolingua Central European Series] (in press)